Gravity Wave Signals From Relativistic Calculations of Binary Neutron Star Coalescence

by

Joshua Aaron Faber

Submitted to the Department of Physics
in partial fulfillment of the requirements for the degree of

Doctor of Philosophy in Physics

at the

MASSACHUSETTS INSTITUTE OF TECHNOLOGY

September 2001

Author .....
Department of Physics
August 10, 2001

Certified by .....
Frederic A. Rasio
Assistant Professor of Physics
Thesis Supervisor

Accepted by .....
Thomas J. Greytak
Professor of Physics
Associate Department Head for Education

Gravity Wave Signals From Relativistic Calculations of Binary Neutron Star Coalescence

by

Joshua Aaron Faber

Submitted to the Department of Physics
on August 10, 2001, in partial fulfillment of the
requirements for the degree of
Doctor of Philosophy in Physics

Abstract

This thesis describes the design, testing, and implementation of a Lagrangian, post-Newtonian, smoothed particle hydrodynamics code used to study the gravitational wave signature produced by coalescing neutron star binary systems. Additionally, we have studied the properties of remnants which may be formed during the merger process. We have introduced a hybrid post-Newtonian formalism, which treats lowest order 1PN relativistic terms at a reduced strength, to make the problem numerically tractable, while treating the gravitational radiation reaction, which is the lowest order dissipative term in general relativity, at full strength. We compare the results of calculations with and without 1PN effects for initially synchronized binary systems, for neutron stars with polytropic equations of state, finding that relativistic corrections play an important role in the dynamical stability of such sytems and the resulting gravitational wave forms. Relativistic corrections also suppress mass shedding in these systems. Studies of initially irrotational binary systems demonstrated that our results are independent of the numerical resolution of the calculations. The power spectrum of the gravitational radiation produced during a merger is found to yield important information about the neutron star equation of state, the binary mass ratio, and other physical parameters of the system.

Thesis Supervisor: Frederic A. Rasio
Title: Assistant Professor of Physics

Acknowledgments

It all started when I was four, and *Cosmos* made its debut on PBS. Apparently, it would have taken a natural disaster to move me away from the TV, and none was provided, and thus I was started on the road to being an astrophysicist (which took me one more year to spell).

Along the way, many people have earned my thanks and gratitude, starting with my family, who provided not only encouragement but my first two telescopes as well. Sure, they often wondered if I would ever be able to find a job, but kept such thoughts to themselves during my impressionable years.

Alex Miller and Dmitry Kondrashov have persevered with me for all these years, an amazing feat given my tendency to ramble on endlessly and occasionally attempt to sing Irish folk songs (just because I know the words doesn't make me any closer to finding the proper key). To their respective moms, I give my thanks for feeding me, letting me stay over, and giving away free psychoanalysis.

There are those in my field who deserve mention, starting with Glenn Faust from my high school, who taught me that sadistic humor does indeed have a place in the scientific world, and it makes for much more interesting midterm exams. Eileen Handelman and David Sharpe at Simon's Rock taught me not just the basics, but also how much fun this could all actually be. Fred Walter and Scott Wolk at Stony Brook let me use a very big telescope, and even paid me for the privilege. Gerry Brown and Fred Rasio taught me that both napkins and supercomputers have the potential for scientific discovery. Finally, to Paul Sherman, Ed Keyes, Nick Morgan, Jamie Portsmouth, John Fregeau, Jeremy Schnittman, and all my other officemates, my sincere and heartfelt thanks for letting me play my music in the office, no matter how eclectic and downright aggravating it proved to be.

For Shevah Margolin, all I can say is that I have enjoyed this past year as much as any in my life, and the largest part of the credit belongs to her. Thank god for those people whose smiles can alleviate all stress, they are few and far between and should be treasured.

Lastly, I dedicate this thesis to Bob Steers. After years of having people accept what I said without argument, he pointed out that I had one too many zeroes in my formulas, and in doing so taught me that humility and humor must never be forgotten. Perhaps my finest moment was the end of a two hour intellectual argument about the definition of entropy, that not only proved us both right, but also taught me just how invaluable it is to appreciate the myriad perspectives that exist for any topic. I may not have thanked him then, but I do now.

Go Mets.

Contents

List of Figures

List of Tables

Chapter 1

Coalescing compact binaries

Coalescing compact binaries with neutron star (NS) or black hole (BH) components provide the most promising sources of gravitational waves for detection by the large laser interferometers currently under construction or in the testing phase, such as LIGO (Abramovici et al. 1992, 1996), VIRGO (Bradaschia et al. 1990; Caron et al. 1997), GEO (Hough 1992; Danzmann 1998; Freise et al. 2000), and TAMA (Kuroda et al. 1997; Tagoshi et al. 2001). In addition to providing an important new test of Einstein's general theory of relativity (GR), gravity waves may provide the strongest evidence to date for the existence of black holes (Lipunov, Postnov, & Prokhorov 1997b; Flanagan & Hughes 1998), and the detection of gravitational waves from coalescing binaries at cosmological distances could provide accurate independent measurements of the Hubble constant and the mean density of the Universe (Schutz 1986; Chernoff & Finn 1993; Marković 1993). As we will demonstrate in this thesis, the gravity wave signals from merging binaries containing NS will also contain important information about the equation of state (EOS) of nuclear matter at high densities.

1.1 Event rates

Expected rates of compact binary coalescence in the Universe, as well as expected event rates in laser interferometers, have now been calculated by many groups. Although there is some disparity among various published results, the estimated rates

are generally encouraging.

The galactic binary NS coalescence rate calculated from population synthesis studies varies widely depending on the assumptions made, resulting in uncertainties of several orders of magnitude (Kalogera 2000). The classic evolutionary scenario for merging binaries involves forming a common envelope around the binary system after the primary has undergone a supernova. As the resulting NS spirals in, the orbital energy is transferred to the secondary, ejecting the envelope and tightening the orbit. Eventually, the secondary also undergoes a supernova explosion, resulting in a close binary NS system (Bhattacharya & van den Heuvel 1991). Unfortunately for this scenario, the amount of mass accreted by the NS is likely to lead to its gravitational collapse and the formation of a black hole (Houck & Chevalier 1992; Chevalier 1993, 1996; Brown 1995; Bethe & Brown 1998). Alternately, in systems where the masses of the primary and secondary are close, both stars can evolve off the main sequence prior to the formation of a common envelope. In this scenario, the common envelope is ejected by the inspiral of two helium stars which both proceed to undergo supernovae, thus producing a close binary NS system (Brown 1995). Other models generally involve minor adjustments to these basic scenarios. Most studies place the total coalescence rate, $\mathcal{R}$, in the range $10^{-6} - 2 \times 10^{-5}\,\mathrm{yr}^{-1}$ for the Milky Way Galaxy (Lipunov, Postnov, & Prokhorov 1997a; Fryer, Burrows, & Benz 1998; Portegies Zwart & Yungelson 1998; Bethe & Brown 1998; Fryer, Woosley, & Hartmann 1999; Grishchuk et al. 2001). Among the greatest sources of uncertainty is the distribution of kick velocities imparted to NS during supernova events, since at present there is little theoretical agreement on which model reproduces the observed distribution of galactic pulsars. Most statistical analyses favor a bimodal velocity distribution, but the relative amplitudes of the two components are not well constrained, nor is the exact magnitude of the respective velocity maxima (Cordes & Chernoff 1998; Lai, Chernoff & Cordes 2001).

Alternatively, the galactic coalescence rate can be estimated by extrapolating from the observed galactic distribution of recycled pulsars in binary systems which should coalesce within a Hubble time. Using the parameters calculated from pulsars PSR

B1913+16 (Taylor & Weisberg 1989) and PSR B1534+12 (Wolczan 1991), the original estimate of the coalescence rate was found to be $\mathcal{R} \simeq 10^{-6}\,\mathrm{yr}^{-1}$ (Narayan, Piran, & Shemi 1991; Phinney 1991). Further revisions to the galactic pulsar population scale height, beaming fraction, and observable lifetime have generally raised this estimate to $\mathcal{R} \simeq 5 - 8.5 \times 10^{-6}\,\mathrm{yr}^{-1}$ (Curran & Lorimer 1995; van den Heuvel & Lorimer 1996; Stairs 1998), although significant uncertainties remain in the estimate of the pulsar beaming angle. Taking into account the difficulties in observing the faint end of the pulsar population, Kalogera et al. (2000) find that the galactic coalescence rate could be as high as $\mathcal{R} \simeq 5 \times 10^{-4}\,\mathrm{yr}^{-1}$. Beyond these difficulties, formation channels for relativistic binaries which do not produce a recycled pulsar can also increase the total coalescence rate without factoring into observed pulsar distributions, requiring significant but poorly understood corrections to the observed rates (Belczynski & Kalogera 2001).

Finn & Chernoff (1993) calculated that an advanced LIGO could observe as many as 20 NS merger events per year. This number corresponds to an assumed merger rate $\mathcal{R} \simeq 10^{-6}\,\mathrm{yr}^{-1}$, which is now thought to be a fairly conservative estimate. Should the coalescence rate prove to be higher, we expect that the rate of detection will rise proportionally up to a maximum of approximately 1000 per year for LIGO II (Kalogera et al. 2000).

The more optimistic estimates above are inconsistent with the upper limit of $\mathcal{R} < 10^{-5}\,\mathrm{yr}^{-1}$ placed on the coalescence rate based on the non-detection of young pulsars in relativistic binaries (Bailes 1996), since both observed relativistic binary pulsar systems contain a recycled pulsar. They are consistent, however, with the more recent upper limit of $\mathcal{R} < 10^{-4}\,\mathrm{yr}^{-1}$ derived by Arzoumanian et al. (1999) on the basis of very general statistical considerations about radio pulsars, including the decrease in search sensitivity arising from Doppler shifting of pulsar signals in tight binaries. This latter limit is consistent with one derived by Kalogera & Lorimer (2000), who studied constraints from supernova explosions in binaries and the relative formation rates of single versus binary pulsars.

1.2 The physics of gravity waves

Gravity waves are a purely relativistic effect, which can be derived from Einstein's field equations when treated in the linear regime. They represent oscillations in the metric of spacetime which satisfy a simple propagation equation when treated in the proper gauge, known as the transverse traceless gauge. The basic derivation of that equation, as well as the limits of its applicability, are discussed below.

To start, we define the linearized metric of spacetime $g_{\mu\nu}$ at every point as

$$g_{\mu\nu} = \eta_{\mu\nu} + h_{\mu\nu} \tag{1.1}$$

where $\eta_{\mu\nu}$ is the metric of flat space and $h_{\mu\nu}$ represents the small deviations from flatness in the metric, and satisfies the condition $|h_{\mu\nu}| \ll 1$. Following tradition, we will use Greek indices to indicate 4-dimensional quantities, and Latin indices to indicate spatial 3-dimensional quantities. Any repeated index is to be summed over. It is important to note that there is a great deal of coordinate freedom in general relativity. The condition $h_{\mu\nu} \neq 0$ can be produced even in flat spacetimes by means of coordinate transformations. Gravity waves, however, represent real deviations from flatness which can be measured in any coordinate system.

The usually adopted gauge to analyze gravitational radiation is the transverse traceless gauge, which can be thought of as the general relativistic analogue of the Coulomb gauge in electromagnetism (Misner, Thorne, & Wheeler 1973; Thorne 1987). It is defined by the conditions that

$$\partial_i h^{0i} = 0 \tag{1.2}$$

$$\partial_j \left(h^{ij} - \frac{1}{3}\delta^{ij} h^k_k \right) = 0. \tag{1.3}$$

In essence, these conditions state that the space-time terms in the metric are divergence free, as is the traceless space-space part of the metric tensor.

With these conditions in place, we redefine the individual metric components as

follows:

$$h_{00} \equiv -2\phi \tag{1.4}$$

$$h_{0i} \equiv w_i \tag{1.5}$$

$$h_{ij} \equiv -2\psi\delta_{ij} - 2s_{ij}, \tag{1.6}$$

with the condition that $s_i^i = 0$. The scalars ϕ and ψ correspond to the Newtonian gravitational potential and the relativistic potential associated with mass-energy density, respectively. The vector $\vec{w}$ is a gravitomagnetic potential, and is associated with precession effects in binary systems analogous to magnetic precession effects in electromagnetism. By our choice of the gauge, the gravitomagnetic potential is divergence-free. Lastly, the tensor s_{ij}, which is transverse by our choice of gauge and traceless by its definition, is the piece of the metric associated with gravitational radiation. With this choice of variables, the field equations reduce to (Bertschinger 2000)

$$\nabla^2\phi = 4\pi G T_{00} \tag{1.7}$$

$$\nabla^2 w_i = 16\pi G T_{0i,\perp} \tag{1.8}$$

$$(\delta_{ij}\nabla^2 - \partial_i\partial_j)(\phi - \psi) + 2\delta_{ij}\nabla\phi = 8\pi G T_{ij,\parallel} \tag{1.9}$$

$$(\nabla^2 - \partial_t^2)s_{ij} = -8\pi G T_{ij,T}, \tag{1.10}$$

where the subscripts $\perp$, $\parallel$, and T refer respectively to the divergence-free, curl-free, and transverse projections of vectors and tensors. It should be noted that the first three equations are static, whereas the last one represents a typical traveling wave solution in 4-dimensional space time. It is this last piece that we associate with gravitational radiation.

In the derivation above, we assumed that the metric was safely in the linear regime. In order to derive the wave field measured by a distant observer, we need one more assumption. The solution to Eq. 1.10 is a familiar integral involving a retarded

potential, given by

$$s_{ij}(r,t) = 2\int \frac{\mathcal{T}_{ij}(x, t-|r-x|)}{|r-x|}\, d^3x, \tag{1.11}$$

where the symbol $\mathcal{T}_{ij}$ and all others like it indicate the traceless part of a tensor. In the slow source approximation, where the velocity of material in the system is slow with respect to c, we find that: $\mathcal{T}_{ij,T}(x, t-|r-x|) \approx \mathcal{T}_{ij,T}(x, t-r)$. For a distant observer, Eq. 1.11 reduces to

$$s_{ij} = \frac{2}{r}\int T_{ij,T}(x, t-r)\, d^3x. \tag{1.12}$$

Relating this expression to the more familiar quadrupole source term is instructive, as it demonstrates why conservation of mass and momentum imply that there can be no monopole or dipole gravitational radiation. In relativity, these conservation principles follow from the zero divergence of the stress-energy tensor, i.e., $\partial_\mu T^{\mu\nu} = 0$. We find that

$$\begin{aligned}
\frac{d^2}{dt^2}\int T_{00}(x,t)x^i x^j d^3x &= \frac{d}{dt}\int \partial_t T^{00} x^i x^j d^3x & (1.13)\\
&= -\frac{d}{dt}\int (\partial_k T^{0k}) x^i x^j d^3x & (1.14)\\
&= \frac{d}{dt}\int (T^{0i}x^j + T^{0j}x^i) d^3x + \text{ surface term} & (1.15)\\
&= \int (\partial_t T^{0i}x^j + \partial_t T^{0j}x^i) d^3x & (1.16)\\
&= -2\int (\partial_k T^{kj}) x^k d^3x & (1.17)\\
&= 2\int T^{ij} d^3x + \text{ surface term,} & (1.18)
\end{aligned}$$

integrating by parts twice in the argument. The boundary terms go to zero if there is no momentum flux over the boundary of the calculation, which is automatically satisfied for a distant observer. We conclude that

$$s_{ij} = \frac{1}{r}\frac{d^2}{dt^2} Q_{ij}(t-r), \tag{1.19}$$

where we define the traceless quadrupole moment as

$$Q_{ij} \equiv \int T_{00}(x) x^i x^j d^3x, \tag{1.20}$$

and note that the quadrupole nature of gravitational radiation is inherently linked to local conservation of energy and momentum. Unlike the electromagnetic case, where there is often a non-trivial time-varying electric dipole moment, we can always define a reference frame in which the mass dipole moment of the system is zero. Additionally, whereas there is one linear polarization for electromagnetic radiation, there are two independent polarizations for gravity waves traveling in a specified direction, typically denoted h_+ and $h_\times$ for the linearly polarized case. For waves traveling in the z-direction, these polarizations are given by

$$h_+(t) = s_{xx} = -s_{yy} = \frac{1}{r}\left(\ddot{Q}_{xx} - \ddot{Q}_{yy}\right) e^{i(kx-\omega t)} \tag{1.21}$$

$$h_\times(t) = s_{xy} = s_{yx} = \frac{2}{r}\ddot{Q}_{xy} e^{i(kx-\omega t)}, \tag{1.22}$$

where the dispersion relation takes the same simple form as it does for electromagnetic waves.

The effect of gravity waves on particles is given by the equation of geodesic motion

$$\frac{dv^\alpha}{d\tau} = \Gamma^\alpha_{\beta\gamma} v^\beta v^\gamma \tag{1.23}$$

where the Christoffel symbols are given in the linear regime by

$$\Gamma^\alpha_{\beta\gamma} = \frac{1}{2}\eta^{\alpha\nu}\left(h_{\beta\nu,\gamma} + h_{\gamma\nu,\beta} - h_{\beta\gamma,\nu}\right). \tag{1.24}$$

For a stationary observer, we find that the acceleration of a particle experiencing the passage of a gravitational wave follows the scaling $\frac{dv}{dt} \propto \partial_t s_{ij}$, and thus the energy flux goes like $(\partial_t s_{ij})^2$. With the proper coefficients, we find that the energy and angular

momentum loss are given respectively by

$$\frac{c^5}{G}L_{GW} = \frac{1}{5}\left\langle Q_{ij}^{[3]}Q_{ij}^{[3]}\right\rangle \tag{1.25}$$

$$\frac{c^5}{G}\frac{dJ_{GW}}{dt} = \frac{2}{5}\epsilon_{ijk}\left\langle Q_{jl}^{[2]}Q_{lk}^{[3]}\right\rangle . \tag{1.26}$$

1.3 Binary inspiral

Even though there are no direct detections to date of gravity waves from astrophysical sources, the strongest test of general relativity relies critically upon their existence. The pulse history of binary pulsar system PSR 1913+16 (Taylor & Weisberg 1989) is well-resolved enough so that all binary parameters can be derived from observed precessions and gravitational time delays. In addition, the decay of the orbit due to energy radiated away in gravity waves meets the predictions of the theory exactly. We will derive the predicted inspiral of a binary system, noting it applies in the regime where the respective NS are at great enough separation that tidal effects play no appreciable role. We will work with circular orbits, since the binaries are expected to have been circularized by gravity wave emission by the time they become visible with laser interferometers.

For a binary system containing stars with individual masses M_1 and M_2, the total mass is given by $M \equiv M_1 + M_2$ and the reduced mass by

$$\mu \equiv \frac{M_1 M_2}{M}. \tag{1.27}$$

For the special case of a binary with equal-mass components we have $M = 2M_{NS}$ and $\mu = \frac{M_{NS}}{2}$. Assuming the stars to be spherical and irrotational, the total Newtonian energy of the system is given by

$$E(r) = \frac{1}{2}(M_1 v_1^2 + M_2 v_2^2) - \frac{GM_1M_2}{r} \tag{1.28}$$

$$= -\frac{1}{2}\frac{GM\mu}{r} \tag{1.29}$$

with an angular velocity given by

$$\omega = \sqrt{\frac{GM}{r^3}} \tag{1.30}$$

where r is the binary separation. The quadrupole moment of the system, when the binary axis makes an angle θ with the x-axis is given by

$$\begin{aligned} Q_{xx} &= \mu r^2(\cos^2\theta - \frac{1}{3}) = \frac{1}{2}\mu r^2 \cos 2\theta + \text{const.} && (1.31)\\ Q_{xy} &= \mu r^2 \cos\theta \sin\theta = \frac{1}{2}\mu r^2 \sin 2\theta && (1.32)\\ Q_{xx} &= \mu r^2(\sin^2\theta - \frac{1}{3}) = -\frac{1}{2}\mu r^2 \cos 2\theta + \text{const.} && (1.33) \end{aligned}$$

Additionally, $Q_{zz} = -\frac{1}{3}\mu r^2$, but the result is time-independent and does not concern us here. The energy radiated away in gravity waves follows as

$$\begin{aligned} \frac{dE_{GW}}{dt} &= \frac{G}{5c^5} Q_{ij}^{[3]} Q_{ij}^{[3]} && (1.34)\\ &= \frac{16 G \mu^2 r^4 \omega^6}{5c^5} \left(2\cos^2 2\theta + 2\sin^2 2\theta\right) && (1.35)\\ &= \frac{32 G^4 \mu^2 M^3}{5c^5 r^5}. && (1.36) \end{aligned}$$

The inspiral rate in this limit is given by equating the energy loss due to gravitational radiation with the energy change resulting from a decrease in separation, such that

$$\begin{aligned} \frac{dr}{dt} &= = \left(\frac{dE_{GW}}{dt}\right)\left(\frac{dE(r)}{dr}\right)^{-1} && (1.37)\\ &= \frac{32 G^4 \mu^2 M^3}{5c^5 r^5} \frac{2r^2}{GM\mu} && (1.38)\\ &= \frac{64 G^3 \mu M^2}{5c^5 r^3}. && (1.39) \end{aligned}$$

This equation can be solved easily for $r(t)$, yielding

$$r(t) = r_0 \left(1 - \frac{t}{\tau_0}\right)^{\frac{1}{4}} \tag{1.40}$$

where $\tau_0 = \frac{5}{256}\frac{c^5 r_0^4}{G^3 \mu M^2}$ is the time remaining until the binary could be expected to merge if both stars were point-masses. The point-mass formalism breaks down, though, when tidal interactions become important in describing the dynamics of the situation, and numerical hydrodynamics calculations are required.

1.4 Detecting binary compact object mergers

The detection of gravity waves stands as one of the great outstanding challenges presented by the general theory of relativity. Indirect detections of gravity waves have been provided by measurements of relativistic effects in the binary pulsar system PSR 1913+16 (Taylor & Weisberg 1989), exactly in accordance with theoretical predictions. However, only the direct detection of oscillations in the metric of space time would provide virtually unassailable proof that Einstein's theory is correct in this respect.

Experimental evidence of gravity wave signals has heretofore been elusive, due to the remarkable challenge posed by measuring an effect which will likely be no bigger than 1 part in 10^{20}, if not smaller. There have been many attempts to observe gravity waves directly, though, starting with the pioneering work of Joseph Weber, who attempted to measure the effect of passing gravity waves on resonant bars (Weber 1961). However, at present, there have been no confirmed detections. A new generation of detectors going online in the next few years may very well change this picture forever. Large scale laser interferometers are currently being built and in some cases tested in the United States (LIGO), Europe (GEO and VIRGO) and Japan (TAMA) with the goal of measuring gravity waves in the frequency range between $10 - 1000$ Hz, and with strain amplitudes as small as $h \approx 10^{-23}$.

The first detector to go online in the year 2000 was the TAMA detector in Japan. It consists of a Michelson interferometer containing two 300m Fabry-Perot cavities oriented perpendicularly to each other. It is designed so that in the absence of a passing gravity wave, the laser beams from both beam arms will interfere destructively when combined. The measurement of a signal at a photodetector should indicate a

mismatch in the lengths of the two arms, theoretically caused by the presence of a passing gravity wave. No signals have been detected yet, but it serves as an important tool for studying the noise spectra of large interferometers (Tagoshi et al. 2001).

The next to go online was LIGO, the Laser Interferometric Gravitational Observatory, which has also entered the testing phase. It consists of two sites, one in Hanford, WA, the other in Livingston, LA, both with a pair of 4km Fabry-Perot cavity tubes. LIGO is most sensitive to oscillations with frequencies in the range $50 - 500$Hz. At lower frequencies, seismic noise swamps any possible detectable signals, while at frequencies above 200Hz, photon shot noise limits the effectiveness of the detector, as there are simply too few photons to be measured within a given time interval with which to construct statistics. In its current state, the detector should be able to measure signals with a strain of $h \sim 10^{-21}$, several orders of magnitude more sensitive than all other previous detectors. The maximum sensitivity is limited near frequencies of 100 Hz by thermal noise within the system optics (Barish 1999).

Even though the technical challenges facing the builders of LIGO have been vast, it is expected that by the latter half of the decade of the 2000's, technology should advance far enough to significantly increase the sensitivity of LIGO, and thus the volume of the universe which it can survey. Better seismic shielding is expected to lower the minimum frequency LIGO can observe by a factor of at least 5, down to ~ 10 Hz. Improved optics are expected to lower the peak sensitivity of the detector to strains of $h \sim 10^{-22} - 10^{-23}$ at frequencies of $f \sim 100 - 300$Hz. Improved laser power should increase the maximum observable frequency of the detector to ~ 1 kHz.

In addition to the American effort, the European detector VIRGO will consist of a pair of 3km Fabry-Perot cavities, to be located in Italy. Additionally, a German-French collaboration is working on 600m interferometer, which will be able to measure signals at high frequencies (> 1 kHz) with unrivaled sensitivity. Special purpose narrow-band detectors that can sweep up frequency in real time will be used to try to catch the last ~ 10 cycles of the gravitational waves during the final coalescence (Meers 1988; Strain & Meers 1991). These "dual recycling" techniques are being tested right now on the German-British interferometer GEO 600 (Freise et al. 2000),

and involve the creation of an additional resonant cavity by means of a mirror located between the Michelson interferometer and the photodetector. Tuned properly, it will operate as an extremely sensitive gravity wave detector, but only near a previously chosen frequency.

In addition to ground-based detectors, plans have been developed for a space-based interferometer composed of three satellites using laser ranging to monitor precisely their relative position in space (Danzmann 2000). Unlike its terrestrial cousins, LISA, the Laser Interferometric Space Antenna, will be sensitive in the millihertz frequency regime. Such frequencies are impractical for studying binary NS mergers, but are ideal for studying the merger of massive binary BH systems. In an ironic touch, the primary noise source for LISA in its peak frequency range will be a confusion limit set by galactic binary white dwarf systems, for although they are extremely weak emitters of gravitational radiation, they far outnumber merging compact object binaries.

It is reasonably safe to say that the theory of gravity wave signals is well understood, at least in the regime where the binary separation is large compared to the radii of the NS. Many calculations of gravitational wave emission from coalescing binaries have focused on the waveforms emitted during the last few thousand orbits, as the frequency sweeps upward from $\sim 10\,\mathrm{Hz}$ to $\sim 300\,\mathrm{Hz}$. The waveforms in this frequency range, where the sensitivity of ground-based interferometers is highest, can be calculated very accurately by performing post-Newtonian (hereafter PN) expansions of the equations of motion for two point masses (Lincoln & Will 1990; Junker & Schäfer 1992; Kidder, Will, & Wiseman 1992; Will 1994; Blanchet et al. 1996). However, at the end of the inspiral, when the binary separation becomes comparable to the stellar radii (and the frequency is greater than 1 kHz), hydrodynamics becomes important and the character of the waveforms must change.

In general, extracting information from observed waveforms, requires detailed theoretical knowledge about all relevant hydrodynamic processes involved in a merger. If the NS merger is followed by the formation of a BH, the corresponding gravitational radiation waveforms will also provide direct information on the dynamics of rotating core collapse and the BH "ringdown" (Flanagan & Hughes 1998). If the

merger produces an remnant which is stable against gravitational collapse, it should eventually be possible to detect the oscillations of the newly formed remnant, using the dual recycling techniques being studied by the GEO detector. This may allow for intensive study of the properties of merger remnants, whose characteristic oscillation frequencies lie above the range at which all other interferometers are effective. Such waveforms contain information not just about the effects of GR, but also about the interior structure of a NS and the nuclear equation of state (hereafter EOS) at high density. Given the large noise background which will hamper all initial observations undertaken at the laser interferometers, it will only be possible to derive meaningful results about the physical properties of NS if features in the gravity wave signal are associated with them prior to any detection.

1.5 Further motivation

While gravity wave emission from coalescing NS binaries has been the main focus of most calculations of such systems performed to date, it is certainly not the only motivating factor leading to their study. In particular, although it is generally assumed that long-period gamma-ray bursts (GRBs) result from the collapse of massive stars, it is quite possible that binary compact object coalescence is responsible for short period bursts. Additionally, there are suggestions that the ejecta of binary NS mergers are responsible for seeding the r-process elements of the universe. In the sections below, we discuss both these topics in greater detail.

1.5.1 Gamma ray bursts

Many theoretical models of gamma-ray bursts (GRBs) have relied on coalescing compact binaries to provide the energy of GRBs at cosmological distances (Eichler et al. 1989; Mészáros & Rees 1992; Narayan, Paczyński, & Piran 1992). The close spatial association of some GRB afterglows with faint galaxies at high redshifts is not inconsistent with a compact binary origin, in spite of the large recoil velocities acquired by compact binaries at birth (Bloom, Sigurdsson, & Pols 1999). Currently the most

popular models all assume that the coalescence leads to the formation of a rapidly rotating Kerr BH surrounded by a torus of debris. Energy can then be extracted either from the rotation of the BH or from the material in the torus so that, with sufficient beaming, the gamma-ray fluxes observed from even the most distant GRBs can be explained (Bloom, Sigurdsson, & Pols 1999). Here also, it is important to understand the hydrodynamic processes taking place during the final coalescence before making assumptions about its outcome. For example, contrary to widespread belief, it is not clear that the coalescence of two $1.4\,M_{\odot}$ NS will form an object that must collapse to a BH, and it is not certain either that a significant amount of matter will be ejected during the merger and form an outer torus around the central object (Rasio 2001).

Further difficulties arise when an explanation is sought for the source of the gamma ray emission. It is generally assumed that the gamma-rays emitted in bursts from coalescing compact binaries result from electron-positron annihilation, fueled in turn by neutrino emission from the hot merger remnant. The details of such calculations are extremely difficult to handle properly, although attempts have been made to study the neutrino emission from merging systems containing either two NS (Ruffert, Janka, & Schäfer 1996; Ruffert et al. 1997; Ruffert, Rampp, & Janka 1997; Ruffert & Janka 1998) or a neutron star in orbit around a black hole (Janka et al. 1999). While the results of these and other calculations cannot conclusively prove or disprove the idea that merging binaries are the progenitors of short-period GRBs, many have so far shown that it is possible to create an axis perpendicular to the orbital plane containing virtually no baryons. This is generally taken as a requirement for maintaining the ultra-relativistic shocks which are observed in GRBs.

1.5.2 Nuclear abundances

The shocks formed during the collision of two NS generate high internal temperatures in the forming merger remnant, typically of order $T \approx 10$ MeV. This allows for rapid neutron capture (r-process) nuclear processes, which can form elements heavier than iron, in the range $A > 90$. Traditionally, it was assumed that all such material was formed in supernovae, but recently questions have been raised as to whether the

entropy in the explosion is large enough to correctly give the elemental ratios seen in older stars (Freiburghaus, Rosswog, & Thielemann 1999; Thielemann et al. 2001).

Rosswog and collaborators have suggested that compact object mergers are a better source site for the production of heavy elements (Rosswog et al. 1999; Rosswog, Freiburghaus, & Thielemann 2000; Rosswog et al. 2000). Their calculations have shown that the ratios of elements produced in the ejecta of mergers matches well with observed abundances, including a decrement in elements with nuclear masses $A < 130$, which has been seen in metal-poor stars (Sneden et al. 2000a,b).

The relevance of binary coalescences hinges on whether or not such systems eject enough mass per event to produce the observed amount of matter seen in metal-poor stars. As we will show in Sec. 6.2, irrotational mergers with equal-mass components eject very little matter whatsoever. Asymmetric mergers, on the other hand, may be an attractive alternative for producing the required quantity of ejected material. Given the fact that only two binary systems have been observed which will merge within a Hubble time, both with nearly equal-mass components, the resolution of this issue may require waiting until observations can provide us with a better estimate of the mass ratio distribution of the binary NS population.

Chapter 2

Previous work on coalescing binaries

The past decade has seen a dramatic increase in our theoretical knowledge of coalescing compact binary systems, spurred on primarily by advances in computing power. Foremost among the problems to be faced is the difficulty associated with numerical hydrodynamics calculations in full general relativity. Most of the history of the field has involved using simpler gravity schemes, which seek to approximate relativistic effects while remaining numerically tractable. A summary is provided in this chapter.

2.1 The innermost stable circular orbit

The final hydrodynamic merger of two compact objects is driven by a combination of relativistic and fluid effects. Even in Newtonian gravity, an innermost stable circular orbit (ISCO) is imposed by global hydrodynamic instabilities, which can drive a close binary system to rapid coalescence once the tidal interaction between the two stars becomes sufficiently strong. The classical analytic work for close involved treating the respective stars as an incompressible fluid (Chandrasekhar 1987). This was extended to compressible fluids analytically in the work of Lai, Rasio, & Shapiro (1993a; 1993b; 1994a; 1994b; 1994c, hereafter LRS1–5 or collectively LRS). This study confirmed the

existence of dynamical instabilities for sufficiently close binaries. Although these simplified analytic studies can give much physical insight into difficult questions of global fluid instabilities, 3D numerical calculations remain essential for establishing the stability limits of close binaries accurately and for following the nonlinear evolution of unstable systems all the way to complete coalescence.

In GR, strong-field gravity between the masses in a binary system is alone sufficient to drive a close circular orbit unstable. In close NS binaries, GR effects combine nonlinearly with Newtonian tidal effects so that the ISCO should be encountered at larger binary separation and lower orbital frequency than predicted by Newtonian hydrodynamics alone, or GR alone for two point masses. The combined effects of relativity and hydrodynamics on the stability of close compact binaries have been studied, using both analytic approximations which are basically PN generalizations of LRS (Lai & Wiseman 1997; Lombardi, Rasio, & Shapiro 1997; Shibata & Taniguchi 1997), as well as numerical calculations in 3D incorporating simplified treatments of relativistic effects (Wang, Swesty, & Calder 1998). It should be noted that 1PN calculations performed by Taniguchi and collaborators (Taniguchi & Shibata 1997; Taniguchi 1999) to study the location of the ISCO for corotating and irrotational binaries find that the ISCO moves inwards as post-Newtonian corrections are increased, due primarily to the effect of 1PN potentials with momentum-based source terms present in the system. Similarly, Buonanno and Damour (1999) find that the ISCO for point masses in a binary under GR moves inwards with increasingly massive objects.

These have been extended to full general relativity by several groups, for both synchronized (Baumgarte et al. 1997, 1998; Gourgoulhon et al. 2001) and irrotational (Bonazzola, Gourgoulhon, & Marck 1999; Marronetti, Mathews, & Wilson 1999; Uryu & Eriguchi 2000; Uryu, Shibata, & Eriguchi 2000; Gourgoulhon et al. 2001) sequences. While these calculations are difficult, they can be done with greater and greater accuracy for a variety of NS parameters. However, for reasons explored in greater detail below, particularly the fact that the orbital instability in binary systems in fundamentally dynamical, hydrodynamics calculations are required to correctly predict the

gravity wave signal produced in binary mergers.

2.2 Newtonian hydrodynamics calculations

A number of different groups have performed hydrodynamics calculations of coalescing NS in Newtonian gravity, using a variety of numerical methods and focusing on different aspects of the problem. Oohara and Nakamura were the first to perform 3D hydrodynamic calculations of binary NS coalescence, using a traditional Eulerian finite-difference code (Oohara & Nakamura 1989; Nakamura & Oohara 1989; Oohara & Nakamura 1990; Nakamura & Oohara 1991; Oohara & Nakamura 1992). Rasio and Shapiro (1992; 1994; 1995, hereafter RS1–3 or collectively RS), instead used the Lagrangian method SPH (Smoothed Particle Hydrodynamics). They focused on determining the ISCO for initial binary models in strict hydrostatic equilibrium and calculating the emission of gravitational waves from the coalescence of unstable binaries. Many of the results of RS were later independently confirmed by New & Tohline (1997) and Swesty et al. (Swesty, Wang, & Calder 2000; Wang, Swesty, & Calder 1998), who used completely different numerical methods but also focused on stability questions, and by Zhuge, Centrella, & McMillan (1994; 1996), who also used SPH. Several groups have incorporated a treatment of the nuclear physics in their hydrodynamic calculations, done using SPH (Davies et al. 1994; Rosswog et al. 1999, 2000) and PPM codes (Ruffert, Janka, & Schäfer 1996; Ruffert, Rampp, & Janka 1997; Ruffert et al. 1997; Ruffert & Janka 1998), motivated by cosmological models of GRBs.

Zhuge et al. (1994; 1996) and Ruffert et al. (Ruffert, Janka, & Schäfer 1996; Ruffert, Rampp, & Janka 1997) also explored in detail the dependence of the gravitational wave signals on the initial NS spins. Because the viscous timescales for material in the NS is much longer than the dynamical timescale during inspiral, it is generally assumed that NS binaries will be non-synchronized during mergers. It is generally found than non-synchronized binaries yield less mass loss from the system, but very similar gravity wave signals, especially during the merger itself when the gravity wave

luminosity is highest (Ruffert, Janka, & Schäfer 1996).

Much of the early work on coalescing NS binaries assumed Newtonian gravity for simplicity. Later studies added a treatment of the radiation reaction, which is responsible for driving the system towards coalescence, either by adding a frictional drag term to model point-mass inspiral (Davies et al. 1994; Zhuge, Centrella, & McMillan 1994, 1996; Rosswog et al. 1999, 2000), or by an exact PN treatment (Ruffert, Janka, & Schäfer 1996; Ruffert et al. 1997; Ruffert, Rampp, & Janka 1997). In essence, 2.5PN radiation reaction terms (which scale like $1/c^5$) are added onto a Newtonian framework, but all lower-order non-dissipative terms are ignored. Unlike adding a frictional drag term which dissipates energy according to the point-mass prediction, the lowest-order treatment of the radiation reaction allows for its effects to be included throughout the entire calculation, including the period after the merger remnant has formed. Unfortunately, however, Newtonian gravity is known to be a poor description of the physical problem at hand. Even NS with stiff EOS generate strong gravitational fields. During the final moments before merger, the velocities found in the system also become relativistic. Thus, the hydrodynamics of the actual coalescence can only be calculated properly by taking into account GR effects.

All recent hydrodynamic calculations agree on the basic qualitative picture that emerges for the final coalescence. As the ISCO is approached, the secular orbital decay driven by gravitational wave emission is dramatically accelerated (see also LRS2, LRS3). The two stars then plunge rapidly toward each other, and merge together into a single object in just a few rotation periods. In the corotating frame of the binary, the relative radial velocity of the two stars always remains very subsonic, so that the evolution is nearly adiabatic. This is in sharp contrast to the case of a head-on collision between two stars on a free-fall, radial orbit, where shock heating is very important for the dynamics (RS1, Shapiro 1998). Here the stars are constantly being held back by a slowly receding centrifugal barrier, and the merging, although dynamical, is much more gentle. After typically $1 - 2$ orbital periods following first contact, the innermost cores of the two stars have merged and the system resembles a single, very elongated ellipsoid. At this point a secondary instability occurs: mass

shedding sets in rather abruptly. Material, typically composing $\sim 10\%$ of the total mass of the system, is ejected through the outer Lagrange points of the effective potential and spirals out rapidly. In the final stage, the inner spiral arms widen and merge together, forming a nearly axisymmetric torus around the inner, maximally rotating dense core.

2.3 Post-Newtonian calculations

The Newtonian limit also fails to describe accurately the onset of dynamical instability. PN effects combine nonlinearly with finite-size fluid effects and this can dramatically increase the critical binary separation (and thus lower the frequency) at which dynamical instability sets in. Indeed, the quasi-equilibrium description applies so long as the dynamical timescale of the NS in the binary remains large compared to the timescale on which the gravitational radiation drives the inspiral, with the infall rate being given by Eq. 1.37. Relativistic corrections to the gravitational energy of as system have a strong effect on the equilibrium energy, and can lead to the minimum value being moved further out. Beyond this, they can also flatten the slope of the relationship out beyond the ISCO, leading to a divergence in the formula for the inspiral rate, and thus a breakdown of dynamical stability well out beyond the ISCO.

The middle ground between Newtonian and fully relativistic calculations is the study of the hydrodynamics in PN gravity. Formalisms exist describing not only all lowest-order corrections (1PN) to Newtonian gravity, but also the lowest-order (2.5PN) effects of gravitational radiation reaction (Blanchet, Damour, & Schäfer 1990, hereafter BDS; Shibata, Oohara, & Nakamura 1992). Such calculations have been undertaken by Shibata, Oohara & Nakamura (1992; 1993; 1997) using an Eulerian grid-based code of their own devising, and more recently by Ayal et al. (2001) using SPH along with the formalism of BDS.

PN calculations of NS binary coalescence are particularly relevant for stiff NS EOS. Indeed, for most recent stiff EOS, the compactness parameter for a typical $1.4\,M_\odot$ NS is in the range $GM/Rc^2 \simeq 0.1 - 0.2$, justifying a PN treatment. Af-

ter complete merger, an object close to the maximum stable mass is formed, with $GM/Rc^2 \simeq 0.3 - 0.5$, and relativistic effects become much more important. However, even then, a PN treatment can remain qualitatively accurate if the final merged configuration is stable to gravitational collapse on a dynamical timescale (see the discussion in Sec. 4.4). Most recent theoretical calculations, such as the latest version of the Argonne/Urbana EOS (Akmal, Pandharipande, & Ravenhall 1998), and a number of recent observations of cooling NS (Wang et al. 1999) provide strong support for a stiff NS EOS.

The most significant problem facing PN hydrodynamic simulations is the requirement that all 1PN quantities be small compared to unity. Unfortunately, this precludes the use of realistic NS models. Shibata, Oohara & Nakamura (1992; 1993; 1997) computed 1PN mergers of polytropes with $\Gamma = 5/3$ and a compactness $GM/Rc^2 = 0.03$, leaving out the effects of the gravitational radiation reaction. Ayal et al. (2001) performed calculations for polytropes with $\Gamma = 1.6$ or $\Gamma = 2.6$ and compactness values in the range $GM/Rc^2 \simeq 0.02 - 0.04$, including the effects of the gravitational radiation reaction. For comparison, a realistic NS of mass $M = 1.4\,M_\odot$ and radius $R = 10\,\mathrm{km}$ has $GM/Rc^2 = 0.2$, i.e., about an order of magnitude larger. Unfortunately, performing calculations with artificially small values of GM/Rc^2 also has the side effect of dramatically inhibiting the radiation reaction, which scales as $(GM/Rc^2)^{2.5}$.

The PN SPH code we use in this work, described in detail in Sec. 3.2, combines a new parallel version of the Newtonian SPH code used by RS with a treatment of PN gravity based on the formalism of BDS. Our calculations include all 1PN effects, as well as a PN treatment of the gravitational radiation reaction. We have also developed a relaxation technique by which accurate quasi-equilibrium configurations can be calculated for close binaries in PN gravity. These serve as initial conditions for our hydrodynamic coalescence calculations. In addition, we present in this work a simple solution to the problem of suppressed radiation reaction for models of NS with unrealistically low values of GM/Rc^2.

2.4 Relativistic work

Several groups have been working on fully general relativistic (GR) calculations of NS mergers, combining the techniques of numerical relativity and numerical hydrodynamics in 3D (Baumgarte, Hughes, & Shapiro 1999; Shibata 1999; Shibata & Uryu 2000, 2001). However, this work is still in the early stages of development, and only preliminary results have been reported so far. Obtaining accurate gravitational radiation wave forms from full GR simulations is particularly difficult, since the waves must be extracted at the outer boundaries of large 3D grids extending out into the true wave zone of the problem. However, fully GR calculations are essential for addressing the question of the stability to gravitational collapse and ultimate fate of a merger. Using a GR formalism developed by Shibata (1999), Shibata and Uryu (2000; 2001) find that collapse to a black hole on a dynamical time scale during final coalescence does not happen for NS with stiff EOS and realistic parameters. Only with unrealistically compact initial NS models (starting already very close to the maximum stable mass) does collapse to a black hole occur on the merger time scale. This serves as reassurance that for realistic NS with stiff EOS, PN calculations of binary coalescence can provide results that remain at least qualitatively correct all the way to a complete merger.

Chapter 3

Numerical methods

The code described in this work is a Smoothed Particle Hydrodynamics (SPH) scheme which includes not only Newtonian physics, but also all lowest-order (1PN) corrections of general relativity, as well as the lowest-order dissipative terms (2.5PN) which result from the gravitational radiation reaction. It was constructed by the author of this thesis, by adapting the Newtonian SPH code which was used in RS. A description of the theory behind SPH, as well as the specific adaptations employed by the author follow below.

Note: This chapter contains an edited version of appendices contained in two articles published in Physical Review D. Please see Chapters 4 and 5 for more information.

3.1 The SPH method

Smoothed Particle Hydrodynamics (SPH) is a Lagrangian method ideally suited to calculations involving self-gravitating fluids moving freely in 3D. The key idea of SPH is to calculate pressure gradient forces by kernel estimation, directly from the particle positions, rather than by finite differencing on a grid. SPH was introduced more than 20 years ago by Lucy, Monaghan, and collaborators (Lucy 1977; Gingold & Monaghan 1977), who used it to study dynamical fission instabilities in rapidly rotating stars. Since then, a wide variety of astrophysical fluid dynamics problems have been tackled

using SPH (Monaghan 1992; Dave, Dubinsky, & Hernquist 1997; Rasio 2000).

Because of its Lagrangian nature, SPH presents some clear advantages over more traditional grid-based methods for calculations of stellar interactions. Most importantly, fluid advection, even for stars with a sharply defined surface such as NS, is accomplished without difficulty in SPH, since the particles simply follow their trajectories in the flow. In contrast, to track accurately the orbital motion of two stars across a large 3D grid can be quite tricky, and the stellar surfaces then require a special treatment (to avoid "bleeding"). SPH is also very computationally efficient, since it concentrates the numerical elements (particles) where the fluid is at all times, not wasting any resources on empty regions of space. For this reason, with given computational resources, SPH provides higher averaged spatial resolution than grid-based calculations, although Godunov-type schemes such as PPM typically provide better resolution of shock fronts (this is certainly not a decisive advantage for binary coalescence calculations, where no strong shocks ever develop). SPH also makes it easy to track the hydrodynamic ejection of matter to large distances from the central dense regions. Sophisticated nested-grid algorithms are necessary to accomplish the same with grid-based methods.

The idea behind the SPH method is to follow the motion of a large number of particles N, which will be indexed by m and n in the following description (as opposed to i and j, which will refer to spatial indices of vectors and tensors). In Newtonian systems, the position and velocity of each particle is updated using a leap-frog time stepping algorithm such that

$$\frac{d\vec{x}_m}{dt} = \vec{v}_m \tag{3.1}$$

$$m_m \frac{d\vec{v}_m}{dt} = \vec{F}_m^{(grav)} + \vec{F}_m^{(hydro)} \tag{3.2}$$

where m_m is the mass of each particle. In all calculations presented in this work, the number of particles per NS was the same for both components of the binary. In unequal-mass calculations the individual particle masses, which do not vary in time, were uniform within each NS but differed from one to the other in proportion to the

mass of the respective NS. The local density is defined by summing over the nearest neighbors of a particle, weighting each by a term derived from a smoothing kernel. The ideal number of neighbors N_N is constant throughout the calculation, and is generally ~ 100 particles. In what follows, all summations are over neighbors, unless otherwise noted. The density at each particle position is thus calculated as

$$\rho_m = \sum_n m_n W_{mn} \tag{3.3}$$

where W_{mn} is a symmetric function of the relative separation of the particles and their smoothing lengths h_m and h_n, given by (Hernquist & Katz 1989)

$$W_{mn} = \frac{1}{2}[W(|\vec{x}_m - \vec{x}_n|, h_m) + [W(|\vec{x}_m - \vec{x}_n|, h_n)] \tag{3.4}$$

and the interpolation kernel $W(r,h)$ is defined as (Monaghan & Lattanzio 1985)

$$W(r,h) = \frac{1}{\pi h^3} \begin{cases} 1 - \frac{3}{2}\left(\frac{r}{h}\right)^2 + \frac{3}{4}\left(\frac{r}{h}\right)^3, & 0 \leq \frac{r}{h} < 1 \\ \frac{1}{4}\left[2 - \left(\frac{r}{h}\right)\right]^3, & 1 \leq \frac{r}{h} < 2 \\ 0, & \frac{r}{h} \geq 2 \end{cases} \tag{3.5}$$

so as to be continuous and smooth to second order. The smoothing length h_m is updated after every iteration so as to keep the number of neighbors as close as possible to N_N, and represents the effective size of the particle in the simulation. It is the finite extent of the smoothing kernel, combined with its differentiability, that helps us avoid almost all problems associated with trying to differentiate over otherwise discrete quantities.

All calculations in this work feature polytropic equations of state (EOS), with pressures defined in terms of an adiabatic index Γ, such that

$$P_m \equiv k\rho_m^\Gamma \tag{3.6}$$

with k a constant which takes a single value for all particles, in the absence of artificial viscosity terms, which are not employed in any of the calculations we describe. The

hydrodynamic force on each particle is found by

$$F_m^{(hydro)} = -\sum_n m_m m_n \left(\frac{P_m}{\rho_m^2} + \frac{P_n}{\rho_n^2} \right) \nabla_m W_{mn}. \tag{3.7}$$

It should be noted that the above equations satisfy Newton's third law when neighborhood is a symmetric process, i.e. particle A being a neighbor of particle B implies the converse. This condition is extremely difficult to meet in practice, although it does occur for the majority of particle pairs. In order to maintain conservation of linear momentum properly, we use a "gather-scatter technique" which ensures force balance between pairs of particles. The equations for computing the local density, Eq. 3.3, and hydrodynamic pressure force, Eq. 3.7, are modified by splitting the sum between the particle and its neighbors. When calculating the density, half of the indicated sum is added to the total for the particle, and half to the neighbor's total. The full sum is attained should the particles both be each other's neighbor. When calculating forces, half the indicated total is given to the particle in question, and an equal but opposite amount to the neighbor. While it may seem odd at first, this method does yield the correct densities when applied to arbitrary matter configurations, and does maintain force balance to within the numerical precision limits of the code. The formalism presented above for Newtonian SPH can be shown to conserve energy if the smoothing lengths of particles were fixed quantities. As they vary slowly through the calculation, the total energy can show slight variations, but the effect is tiny compared to other energy scales in the calculation.

Our simulations were performed using a modified version of an SPH code that was originally designed to perform 3D Newtonian calculations of stellar interactions (Rasio & Shapiro 1991, RS1). Although the fluid description is completely Lagrangian, the gravitational field in our code (including PN terms) is calculated on a 3D grid using an FFT-based Poisson solver. Essentially, the method relies on the fact that the equation for the gravitational potential, and in fact any Poisson equation, is a convolution over the source term. Since

$$\nabla^2 \Phi = 4\pi G \rho \tag{3.8}$$

has a solution given by

$$\Phi(\vec{x}) = \int d^3\vec{x'} \frac{G\rho(\vec{x'})}{|\vec{x} - \vec{x'}|} \tag{3.9}$$

we use Fourier techniques to transform this to

$$F(\Phi) = F\left(\int d^3\vec{x'} \frac{G\rho(\vec{x'})}{|\vec{x} - \vec{x'}|}\right) \tag{3.10}$$

$$= F(\rho) \times F\left(\frac{1}{|\vec{x'}|}\right) \tag{3.11}$$

This method has the advantage that the second term in the above equation, representing $1/r$ fall-off of a potential, can be calculated at the beginning of a run and stored in memory from then on, so that each Poisson equation requires only one forward and one reverse FFT per iteration of the code. Our Poisson solver is based on the FFTW of Frigo & Johnson (1997), which features fully parallelized real-to-complex transforms. Boundary conditions are handled by zero-padding all grids, which has been found to produce accurate results and to be the most computationally efficient method (Swesty, Wang, & Calder 2000). Particle quantities are placed on the numerical grid by a cloud-in-cell method, which distributes their value to the eight corners of the cell surrounding the particle, weighted by its location within the cell. Field values, such as the gravitational potential, are read from the grid by the same method. Since we are primarily interested in the gravitational wave emission, which originates mainly from the inner dense regions of NS mergers, we fix our grid boundaries to be ± 4 NS radii in all directions from the center of mass. Particles that fall outside these boundaries are treated by including a simple monopole gravitational interaction with the matter on the grid. Our code has been developed on the SGI/Cray Origin2000 parallel supercomputer at NCSA. MPI (the Message Passing Interface) reduces the memory overhead of the code by splitting all large grids among the processors. All hydrodynamic loops over SPH particles and their neighbors have also been fully parallelized using MPI, making our entire code easily portable to other parallel supercomputers. The parallelization provides nearly linear speedup with increasing number of processors up to ~ 10, with a progressive degradation for larger numbers.

3.2 The BDS formalism

To investigate the hydrodynamics of NS binary coalescence beyond the Newtonian regime, the equations of RS were modified to account for PN effects described by the formalism of BDS, converted into a Lagrangian, rather than Eulerian form. The formalism is correct to first (1PN) order, with all new forces calculated from eight additional Poisson-type equations with compact support, allowing for the computation of all 1PN terms using the same FFT-based convolution algorithm as for the Newtonian Poisson solver. PN corrections to hydrodynamic quantities are calculated by the SPH method, i.e., by summations over particles. Dissipation of energy and angular momentum by gravitational radiation reaction is included to lowest (2.5PN) order, requiring the solution of one additional Poisson-type equation.

The key changes to the BDS formalism involve a conversion to quantities based on SPH particle positions, rather than grid points. All quantities in the BDS scheme are essentially 1PN analogues of familiar Newtonian terms. The coordinate rest-mass density r_* and momentum per unit rest-mass w_i take the place of the density and velocity of each particle, and are given in terms of the proper rest-mass density ρ and the 4-velocity u^μ by

$$r_* \equiv \sqrt{g}u^0\rho \tag{3.12}$$

$$w_i \equiv \left(1+\frac{H}{c^2}\right)cu_i, \tag{3.13}$$

where H is the specific enthalpy of the fluid. The rest-mass density is calculated at each particle position as a weighted sum over the masses of neighboring particles, just as the density is calculated in Newtonian SPH, such that

$$r_*^{(m)} = \sum_n m_n W_{mn}, \tag{3.14}$$

where m_m is the rest mass of particle m. For a PN polytropic equation of state, where

the pressure p_* is defined as a function of the coordinate rest mass density as

$$p_*(r_*) = kr_*^\Gamma, \tag{3.15}$$

it is found that the specific enthalpy is given by

$$H = k\frac{\Gamma}{\Gamma - 1}r_*^{\Gamma-1} = \frac{\Gamma}{\Gamma - 1}\frac{p_*}{r_*}. \tag{3.16}$$

It should be noted that p_* is not the Newtonian pressure, but rather a 1PN variant of it.

The BDS formalism requires the solution of nine Poisson equations, one for the Newtonian gravitational potential U_*, seven for 1PN corrections, and a final one to handle the gravitational radiation reaction.

The equation for the gravitational potential is

$$\nabla^2 U_* = -4\pi r_*. \tag{3.17}$$

Note that with this sign convention, the gravitational potential is a positive quantity. The 1PN correction potentials are given by

$$\nabla^2 U_i = -4\pi r_* w_i \tag{3.18}$$

$$\nabla^2 C_i = -4\pi x^i \partial_k (r_* w_k) \tag{3.19}$$

$$\nabla^2 U_2 = -4\pi r_* \delta. \tag{3.20}$$

Note that the summation in Eq. 3.18 runs over $i = x, y, z$, thus U_2 is an entirely separate quantity than U_y in Eq. 3.20. Using these, we define the quantity

$$A_i \equiv 4U_i + \frac{1}{2}C_i - \frac{1}{2}x^i \partial_s U_s. \tag{3.21}$$

It is important to note that the volume integral of the source term of Eq. 3.19 vanishes, assuming that the origin is at the center of mass and momentum of the

system, and thus it contains no monopole term. In Eq. 3.20, the quantity δ in the source term is one of three quantities which are assumed to be of order $O(\frac{1}{c^2})$. They are, assuming the equation of state Eq. 3.15, and with the definition $w^2 \equiv \delta^{ij} w_i w_j$,

$$\alpha = 2U_* - \Gamma(\frac{1}{2}w^2 + 3U_*) \tag{3.22}$$

$$\beta = \frac{1}{2}w^2 + \frac{\Gamma}{\Gamma - 1}\frac{p_*}{r_*} + 3U_* \tag{3.23}$$

$$\delta = \frac{3}{2}w^2 + \frac{3\Gamma - 2}{\Gamma - 1}\frac{p_*}{r_*} - U_*. \tag{3.24}$$

The third derivative of the symmetric, trace-free (STF) quadrupole tensor, $Q_{ij}^{[3]}$, is calculated by using the SPH equation for the second derivative

$$\ddot{Q}_{ij} = \sum_m m_m (w_i^{(m)} w_j^{(m)} + x_i^{(m)} \dot{w}_j^{(m)} + x_j^{(m)} \dot{w}_i^{(m)}) \tag{3.25}$$

and numerically differentiating once. It is used in the source term for the radiation reaction potential U_5, of order $O(\frac{1}{c^5})$. This is calculated from the final Poisson equation,

$$U_5 = \frac{2}{5}G\left(R - Q_{ij}^{[3]} x^i \partial_j r_*\right) \tag{3.26}$$

$$\nabla^2 R = -4\pi Q_{ij}^{[3]} x^i \partial_j r_*. \tag{3.27}$$

Since we are dealing with the trace-free quadrupole tensor, it is easy to show that the volume integral of the source term of Eq. 3.27 also vanishes, for any mass distribution. The resulting expression for the radiation reaction potential differs from the third derivative expression given in BDS by a term of $O\left(v^2/c^2\right)$, but all radiation reaction terms into which it enters already contain factors of $O\left(v^5/c^5\right)$. While only approximate, this method proved more stable since it does not require the numerical evaluation of several second derivatives on a grid.

The PN forces are defined by

$$F_i^{press} = -\left(1 + \frac{\alpha}{c^2}\right)\frac{\partial_i p_*}{r_*} - \frac{1}{c^2}\frac{p_*}{r_*}\partial_i \alpha \tag{3.28}$$

$$F_i^{1PN} = \left(1 + \frac{\delta}{c^2}\right) \partial_i U_* + \frac{1}{c^2}\partial_i U_2 - \frac{1}{c^2} w_s \partial_i A_s \tag{3.29}$$

$$F_i^{reac} = \frac{1}{c^5}\partial_i U_5. \tag{3.30}$$

Finally, the evolution system, in Eulerian form, is given by

$$\partial_t r_* = \partial_i (r_* v^i) \tag{3.31}$$

$$\partial_t w_i = -v^s \partial_s w_i + F_i^{press} + F_i^{1PN} + F_i^{reac}, \tag{3.32}$$

where the particle velocities v^i are related to the specific coordinate momentum w_i by

$$v^i = \left(1 - \frac{\beta}{c^2}\right) w_i + \frac{1}{c^2} A_i + \frac{4}{5}\frac{G}{c^5} w_s Q_{is}^{[3]}. \tag{3.33}$$

The quantities $\vec{v}$ and $\vec{w}$ will be referred to simply as the velocity and momentum vectors, respectively (Ruffert, Janka, & Schäfer 1996).

In the SPH method, the evolution equations must be expressed in a Lagrangian form, given simply by

$$\dot{x}^i = v^i \tag{3.34}$$

$$\dot{w}_i = F_i^{press} + F_i^{1PN} + F_i^{reac}. \tag{3.35}$$

In BDS, there also appear evolution equations for the entropy and the pressure. The former is automatically conserved in adiabatic calculations such as those we present here, and the latter is not necessary since we calculate the pressure directly from the density at each time step.

Since the parameters α and β, defined by Eqs. 3.22 & 3.23 become rather large for NS with $GM/Rc^2 \sim 0.05$, we make some small adjustments to Eqs. 3.28 & 3.33. We note that for an adiabatic exponent $\Gamma > \frac{2}{3}$, α is everywhere negative. To ensure that the pressure force always acts in the proper direction, we make a substitution in Eq. 3.28,

$$-\left(1 + \frac{\alpha}{c^2}\right)\frac{\partial_i p_*}{r_*} \rightarrow -\left(1 - \frac{\alpha}{c^2}\right)^{-1}\frac{\partial_i p_*}{r_*}. \tag{3.36}$$

This new form is entirely equivalent to the one it replaces to 1PN order. Similarly, β is everywhere positive, so we make the following substitution in Eq. 3.33,

$$\left(1 - \frac{\beta}{c^2}\right) w_i \rightarrow \left(1 + \frac{\beta}{c^2}\right)^{-1} w_i. \tag{3.37}$$

For the PN pressure force (Eq. 3.28), we now find

$$F_i^{press} = -(1 - \frac{\alpha}{c^2})^{-1} F_i^{hydro} - \frac{1}{c^2}\frac{p_*}{r_*}\partial_i \alpha. \tag{3.38}$$

In the calculation of $\partial_i \alpha = (2 - 3\Gamma)\partial_i U_* - \frac{\Gamma}{2}\partial_i w^2$, we must take a derivative of the local dynamic velocity-squared field, which we do by SPH summations, i.e., we first write

$$\partial_i (w^2) = \frac{1}{r_*}(\partial_i (r_* w^2) - w^2 \partial_i r_*), \tag{3.39}$$

and we then calculate the derivative terms as

$$\partial_i r_*^{(m)} = \sum_n m_n \partial_i W_{mn}, \tag{3.40}$$

$$\partial_i (r_* w^2)^{(m)} = \sum_n m_n w_{(n)}^2 \partial_i W_{mn}. \tag{3.41}$$

The nine Poisson-type equations in the full PN formalism of BDS are all solved by the same FFT convolution method. All 3D grids used by the Poisson solver are distributed among the processors in the z-direction. Real-to-complex transforms are computed using the RFFTWND_MPI package of the FFTW library (Frigo & Johnson 1997). The source terms of the Poisson equations that do not contain density derivatives, Eqs. 3.17,3.18, & 3.20, are laid down on the grid by a cloud-in-cell method. All integrals over the density distribution are converted into sums over particles, e.g.,

$$U_*(x) = \int d^3x \frac{r_*(x')}{|x - x'|} \rightarrow \sum_b \frac{m_b}{|x - x_b|}. \tag{3.42}$$

Source terms containing density derivatives are calculated by finite differencing on the grid, rather than by SPH-based derivatives at particle positions. This has two

benefits. First, for integrals of the type

$$\Phi = \int d^3x \; \partial_i r_* \ldots \tag{3.43}$$

we cannot convert directly from a volume integral to a sum over discrete particle masses. Second, it guarantees that the volume integral of the source term vanishes in Eqs. 3.19 & 3.27, as it should. Derivatives of the potentials are computed by finite differencing on the grid, and then interpolated between grid points to assign values at SPH particle positions.

For calculations in which we include the radiation reaction, but ignore 1PN corrections, all terms containing a factor of $1/c^2$ can be ignored. In this case our equations reduce to those of the purely Newtonian case, with two exceptions. First, we include F_i^{reac} (Eq. 3.30) in the SPH equations of motion, replacing Eq. 3.32 by

$$\dot{w}_i = -\frac{\partial_i p_*}{r_*} + \partial_i U_* + F_i^{reac}. \tag{3.44}$$

Second, the relationship between the particle velocity $\vec{v}$ and momentum $\vec{w}$ is given by

$$v_i = w_i + \frac{4}{5}\frac{G}{c^5} Q_{ij}^{[3]} w_j. \tag{3.45}$$

This has been shown (Ruffert, Janka, & Schäfer 1996) to give the correct energy loss rate as predicted by the classical quadrupole formula, Eq. 1.25.

Ignoring 1PN terms reduces the number of Poisson equations to be solved per iteration from nine to two. The obvious advantage is a proper handling of the dissipative PN effects, while leaving the hydrodynamic equations in a simple form that can be directly compared to the Newtonian case. In addition, because the corrections are $O(v^5/c^5)$, the radiation reaction terms always remain small, even when 1PN corrections would be large.

We have performed a number of test calculations to establish the accuracy of our treatment of PN effects in the SPH code. These include tests for single rotating and nonrotating polytropes in PN gravity, which we have compared to well-known analytic

and semi-analytic results (Shapiro & Teukolsky 1983). In particular, we have verified that our code reproduces correctly the dynamical stability limit to radial collapse for a single PN polytrope with $\Gamma = 5/3$ (see Sec. 3.4.1).

3.3 Our hybrid method

Throughout what follows, unless otherwise specified, we will use units in which Newton's gravitational constant G, and the rest mass M and radius R of a single, spherical NS are set equal to unity. In Newtonian physics, this leads to a scale-free calculation. When we include PN effects, specifying the physical mass and radius of the NS then sets the value of the speed of light c, and the magnitude of all PN terms. In our units, the compactness ratio GM/Rc^2 of a NS is expressed simply as $1/c^2$.

The equations of BDS assume that all 1PN corrections are small. As mentioned in Sec. 2.3, this places a rather severe constraint on the allowed NS mass and radius, since

$$\frac{1}{c^2} = 0.14 \left(\frac{M}{1.5\,M_\odot}\right)\left(\frac{15\,\mathrm{km}}{R}\right). \tag{3.46}$$

If, for example, we estimate the potential at the center of the star as $U_*/c^2 \simeq 1.5/c^2 = 0.21$ (Eq. 3.17), which is appropriate for $\Gamma = 3$ models, we find that our "first-order" correction term α/c^2 (Eq. 3.22), with $\Gamma = 3$ and no internal motions, is

$$\frac{\alpha}{c^2} = (2 - 3\Gamma)\frac{U_*}{c^2} = -7\frac{U_*}{c^2} \simeq -1.5. \tag{3.47}$$

This is clearly problematic since the derivation of the BDS formalism assumes that $|\alpha|/c^2 \ll 1$. For a fixed radius of 15 km and $\Gamma = 3$, a NS mass $< 0.9\,M_\odot$, or $1/c^2 < 0.09$ is required to keep $|\alpha| < 1$. This problem is less severe for a lower value of Γ, since the coefficient of α is then smaller. For $\Gamma = 5/3$, we have $\alpha = -3U_*$, but these configurations are known to be unstable against gravitational collapse for compactness parameters $1/c^2 > 0.14$ (Shapiro & Teukolsky 1983). These problems are the reason why previous PN hydrodynamic simulations of NS binary coalescence have used unrealistic NS models with low masses and large radii. In practice, we

find that we cannot calculate reliably NS mergers including 1PN corrections, unless $1/c^2 \leq 0.05$, or $c \geq 4$. With such a small compactness parameter, radiation reaction effects would then be suppressed by a factor $\sim 2^5 = 32$.

Recognizing that the 1PN and 2.5PN terms describe essentially independent phenomena, and that the proper form for energy and angular momentum loss holds even if 1PN corrections are ignored, we adopt a hybrid scheme. Specifically, in all calculations which we will describe below, we set $c = 4.47 \equiv c_{1PN}$ for all 1PN corrections, which is unphysically large, but we use a physically realistic value of $c = 2.5 \equiv c_{2.5PN}$ for the 2.5PN corrections, corresponding, for example, to a NS mass $M = 1.5\,M_\odot$ with radius $R = 13.9\,\mathrm{km}$. We feel that this hybrid formulation provides a reasonable trade-off between physical reality and the limitations of the 1PN approximation.

Note that this method should better extrapolate toward physical reality, compared with unrealistically undercompact NS models. If $0 + 2.5\mathrm{PN}$ simulations are interpreted as taking the limit $c_{1PN} \to \infty$ for the 1PN corrections, we see that by reducing the compactness in both the $0 + 2.5\mathrm{PN}$ and $0 + 1 + 2.5\mathrm{PN}$ cases, the value of $c_{2.5PN}$ is fixed at an unphysical value while c_{1PN} is varied, which can never truly extrapolate to the physical case. By setting $c_{2.5PN}$ to a realistic physical value while varying c_{1PN}, we may be able to extrapolate our results toward a correct physical limit. However, a disadvantage of this approach is that it does not allow for direct quantitative comparison with full GR simulations of binary NS coalescence. In these simulations, which essentially handle corrections to all orders simultaneously, separation into various PN orders has no meaning.

3.4 Initial conditions

In addition to its normal use for dynamical calculations, our SPH code can also be used to construct hydrostatic equilibrium configurations in 3D, which provide accurate initial conditions for binary coalescence calculations. This is done by adding artificial friction terms to the fluid equations of motion and forcing the system to relax to a minimum-energy state under appropriate constraints (RS1). The great ad-

vantage of using SPH itself for setting up equilibrium solutions is that the dynamical stability of these solutions can then be tested immediately by using them as initial conditions for dynamical SPH calculations. Very accurate 3D equilibrium solutions can be constructed using such relaxation techniques, with the virial theorem satisfied to better than 1 part in 10^3 and excellent agreement found with known quasi-analytic solutions in both Newtonian (LRS1, LRS4, RS2) and PN gravity (Lombardi, Rasio, & Shapiro 1997). The careful construction of accurate quasi-equilibrium initial conditions is a distinguishing feature of our PN calculations of binary coalescence. In contrast, many other studies have used very crude initial conditions, placing two spherical stars in a close binary orbit, and, for calculations that went beyond Newtonian gravity, adding the inward radial velocity for the inspiral of two point masses. Unfortunately, spurious fluid motions are created as the stars respond dynamically to the sudden appearance of a strong tidal force can corrupt the gravitational radiation waveforms. Spurious velocities have additional effects in the full 1PN case, where spurious motions enter repeatedly into the evolution equations, by propagating through the 1PN quantities α, β, and δ in Eqs. 3.22, 3.23, & 3.24. A specific cause of worry is the influence of velocities adding to δ, which affects not only the self-gravity of the stars, but also their mutual gravitational attraction.

We have developed a method, described in detail in Sec. 3.4.2 that allows for more realistic initial conditions for PN synchronized binaries. It reduces dramatically the initial oscillations around equilibrium when the dynamical calculation is started.

3.4.1 Single star models

Constructing hydrostatic equilibrium initial conditions in PN gravity is a much more difficult problem than in Newtonian gravity, primarily because of the complex relationship between the particle velocity and momentum. We get around this problem by implementing a multistage approach to the construction of relaxed configurations.

First, we construct a series of hydrostatic equilibrium models for single $\Gamma = 3$ polytropes with increasing values of $1/c^2$, to gauge the effects of the PN corrections on the structure of the stars. Specifically, we construct relaxed models with compactness

parameters of $1/c^2 = 0.01$ to 0.07, in steps of 0.01.

In the relaxation procedure, spurious velocities arising from configurations adjusting toward equilibrium are ignored as sources for the force equations. Thus particles move during the relaxation, but the force exerted on each particle is that of a static mass configuration. We thus solve all Poisson equations assuming $\vec{w} = 0$, which eliminates Eqs. 3.18 & 3.19. In addition, the velocity terms in the definition of the 1PN quantities α, β, and δ are removed from Eqs. 3.22, 3.23, & 3.24. This greatly simplifies the equations giving us the set

$$\nabla^2 U_* = -4\pi r_* \tag{3.48}$$

$$\nabla^2 U_2 = -4\pi r_* \delta \tag{3.49}$$

$$\alpha = (2 - 3\Gamma)U_* \tag{3.50}$$

$$\beta = \frac{\Gamma}{\Gamma - 1}\frac{p_*}{r_*} + 3U_* \tag{3.51}$$

$$\delta = \frac{3\Gamma - 2}{\Gamma - 1}\frac{p_*}{r_*} - U_* \tag{3.52}$$

$$F_i^{press} = -\left(1 + \frac{\alpha}{c^2}\right)\frac{\partial_i p_*}{r_*} - \frac{1}{c^2}\frac{p_*}{r_*}\partial_i \alpha \tag{3.53}$$

$$F_i^{1PN} = \left(1 + \frac{\delta}{c^2}\right)\partial_i U_* + \frac{1}{c^2}\partial_i U_2 \tag{3.54}$$

$$v^i = \left(1 - \frac{\beta}{c^2}\right) w_i \tag{3.55}$$

$$\dot{x}^i = v^i \tag{3.56}$$

$$\dot{w}_i = F_i^{press} + F_i^{1PN} - \frac{w_i}{t_{relax}}, \tag{3.57}$$

where t_{relax} is the relaxation time.

To construct our first model, with $1/c^2 = 0.01$ we start from a Newtonian $\Gamma = 3$ polytrope and let it relax to an equilibrium configuration. Then, using the maximum particle radius R_{max}, we adjust the radial position, smoothing length, and specific entropy of all particles according to

$$\vec{r} \rightarrow \frac{\vec{r}}{R_{max}} \tag{3.58}$$

$$h_m \rightarrow \frac{h_m}{R_{max}} \tag{3.59}$$

$$k_m \rightarrow k_m R_{max}^{4-3\Gamma}. \tag{3.60}$$

Velocities are set to zero at the end of this rescaling. This new configuration is relaxed again, and the process is repeated until convergence is achieved. For the $\Gamma = 3$ models, we rescaled every $t = 5.0$, with a relaxation time $t_{relax} = 1.0$, The final profile is used as the initial test configuration of the next model, which is then relaxed iteratively as described above.

In addition to $\Gamma = 3$ models, we also computed a sequences of single PN polytropes with $\Gamma = 2$ and $\Gamma = 5/3$, and tested their stability. PN effects should make the star unstable to gravitational collapse when $1/c^2 > 0.141$ for $\Gamma = 5/3$ (Shapiro & Teukolsky 1983). Thus, for $\Gamma = 5/3$, We tested $1/c^2$ values in steps of $1/c^2 = 0.02$, until we reached 0.10, at which point we halved the step size until we reached $1/c^2 = 0.13$. To make the relaxation overdamped, we reduced the rescaling time to $t = 2.0$, with $t_{relax} = 1.0$. It was found that $1/c^2 = 0.13$ is always unstable, collapsing inward uncontrollably, no matter how short the rescaling time. This agrees well with the theoretical prediction when we account for the magnitude of the 1PN corrections we deal with, and the approximations made in the analytic treatment. In Fig. 3-1, we show the time evolution of the specific entropy k for all three sequences, taken as a ratio with the Newtonian value of the specific entropy derived from the Lane-Emden equation. We see a gradual increase of k as the compactness is increased, in all sequences, except when we get to $1/c^2 = 0.12$ for $\Gamma = 5/3$, for which k is 50% larger than the corresponding value for $1/c^2 = 0.11$. Note that the vertical scale in the figure is different for each plot. Thus, the value of k/k_N actually increases with increasing adiabatic exponent Γ for a given compactness $1/c^2$.

Parameters for the single star sequences are shown in Table 3.1. Radial profiles of the density, as well as all important 1PN quantities are shown in Figs. 3-2, 3-3, & 3-4 for $\Gamma = 5/3$, $\Gamma = 2$ and $\Gamma = 3$, respectively. We see in the $\Gamma = 5/3$ case that increasing the compactness increases the central concentration of the model, which can be seen in the factor of two increase in central density. For compactnesses near

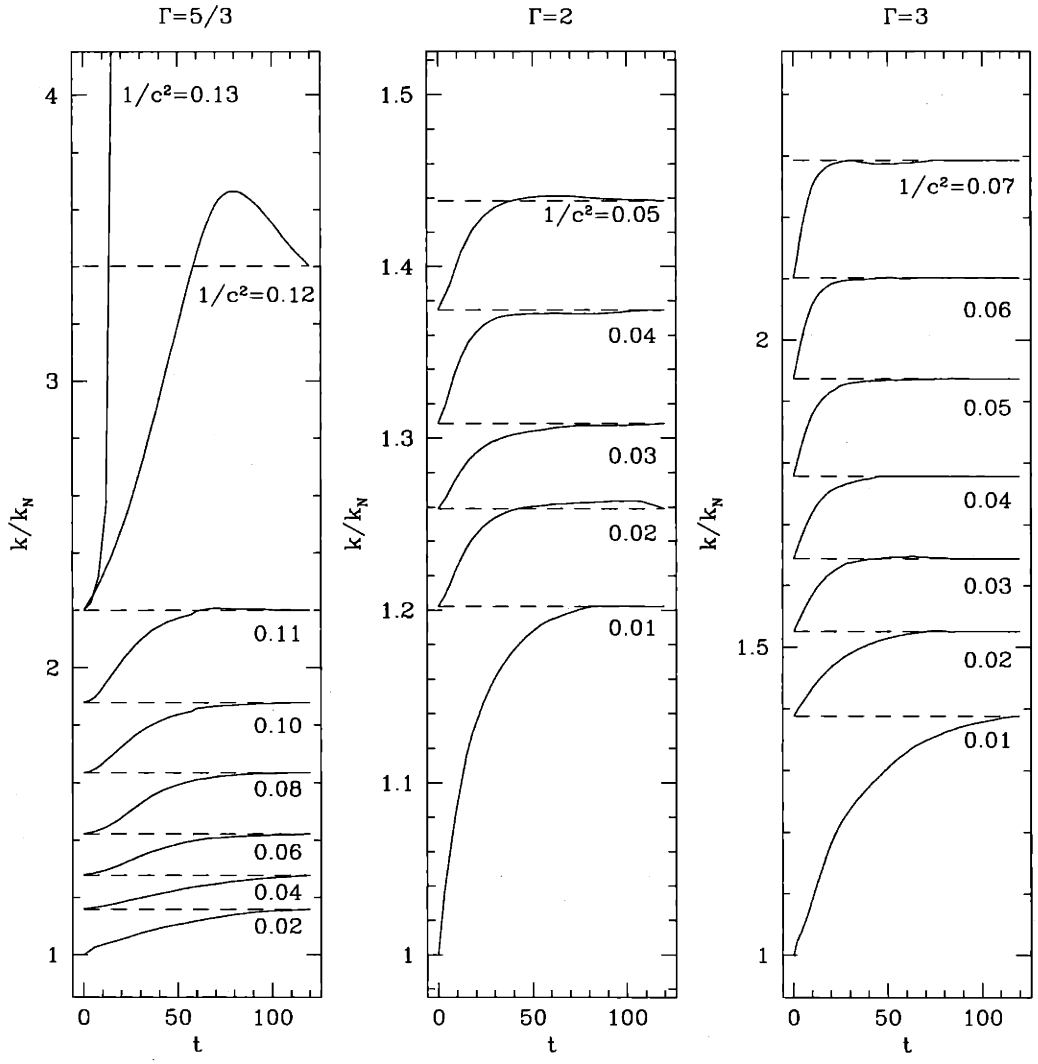

Figure 3-1: Results of SPH relaxation calculations for single stars. The ratio of the PN specific entropy k to the Newtonian value k_N, is shown for $\Gamma = 5/3$, $\Gamma = 2$, and $\Gamma = 3$, computed for sequences of increasing compactness $1/c^2$. The dotted lines give the final value for each case, which was used as the initial value for the next relaxation. For $\Gamma = 5/3$, we see that for $1/c^2 > 0.12$, k/k_N increases without bounds, indicating instability. For $\Gamma = 3$ and $1/c^2 > 0.07$, the 1PN approximation breaks down. Note the different vertical scales.

$1/c^2$	k/k_N	$(r_*)_c$	$(P/r_*c^2)_c$	$(U_*/c^2)_c$
		$\Gamma = 5/3$		
0.02	1.177	1.201	0.0111	0.0438
0.04	1.281	1.292	0.0257	0.0893
0.06	1.421	1.452	0.0464	0.1377
0.08	1.634	1.708	0.0792	0.1902
0.10	1.879	1.976	0.1255	0.2470
0.11	2.198	2.336	0.1806	0.2820
0.12	3.400	2.295	0.3011	0.2968
		$\Gamma = 2$		
0.01	1.202	0.6549	0.0050	0.0187
0.02	1.260	0.6670	0.0107	0.0376
0.03	1.308	0.6963	0.0174	0.0571
0.04	1.375	0.7173	0.0251	0.0767
0.05	1.439	0.7490	0.0343	0.0968
		$\Gamma = 3$		
0.01	1.403	0.3822	0.0052	0.0165
0.02	1.553	0.3818	0.0114	0.0326
0.03	1.649	0.3882	0.0187	0.0486
0.04	1.780	0.3948	0.0280	0.0649
0.05	1.918	0.4051	0.0397	0.0813
0.06	2.084	0.4170	0.0549	0.0989
0.07	2.262	0.4321	0.0746	0.1154

Table 3.1: Parameters for Single Star Models. For each model, we list the compactness parameter $1/c^2$, the ratio of the PN specific entropy k to the Newtonian value k_N, the central values of density r_* in units of M/R^3, and the dimensionless ratios P/r_*c^2 and U_*/c^2.

the stability limit, we see that α, β, and δ are all of order unity. A different behavior is seen in the $\Gamma = 2$ and $\Gamma = 3$ cases, for which the internal structure of the star remains almost unchanged as the 1PN order parameters get large. We see that α and β both get relatively large for more compact models, but δ is rather small, since the potential and pressure terms cancel each other to some extent.

We typically find excellent agreement between our single star models and Runge-Kutta integrations of the equations of structure, with the equations satisfied to well within a fraction of a percent. The only discrepancy appears at the outer edge of the star, where surface effects alter the SPH mass profile slightly. This results from a

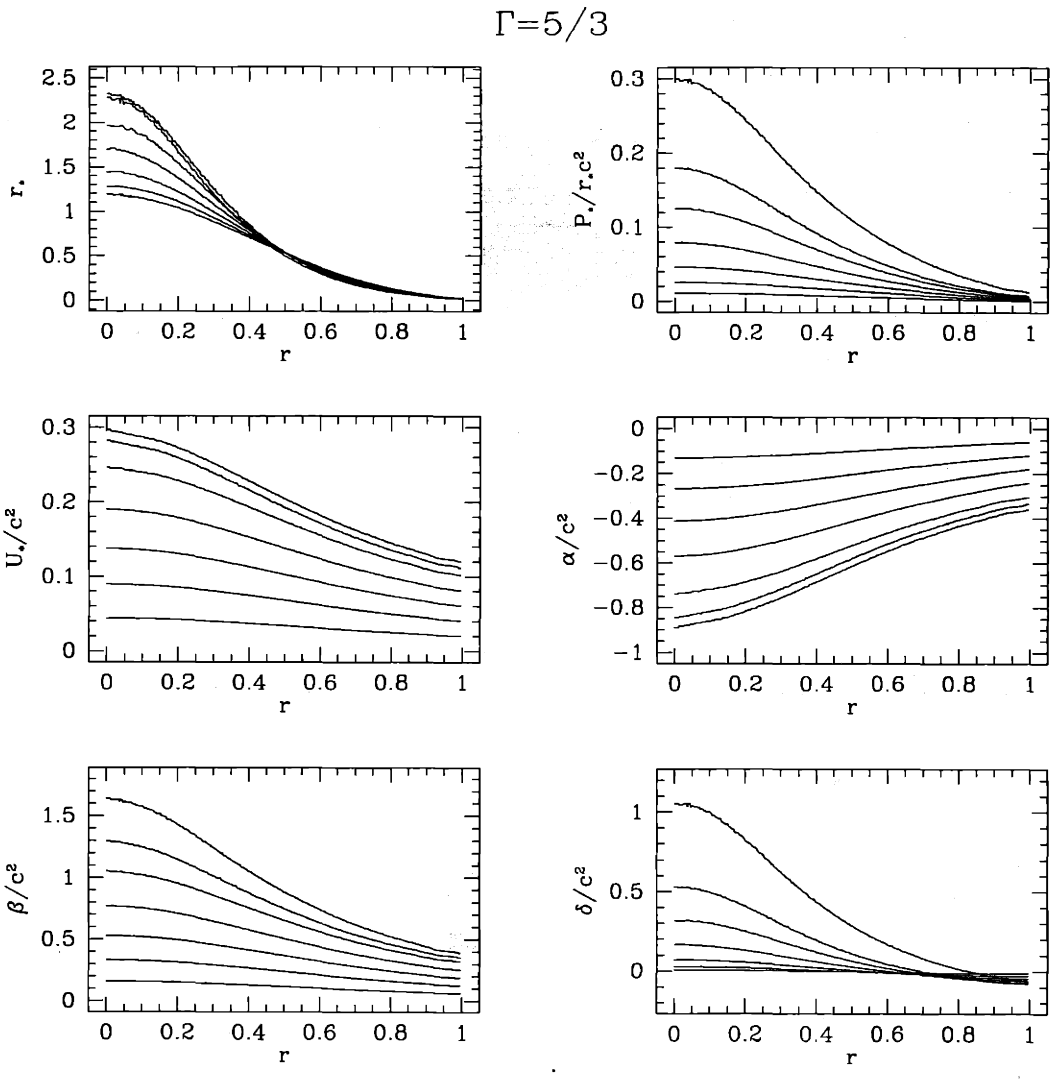

Figure 3-2: Radial profiles for the $\Gamma = 5/3$ single star models. The various lines correspond, in monotonic fashion, to the stable configurations indicated by dotted lines in the left panel of Fig. 3-1.

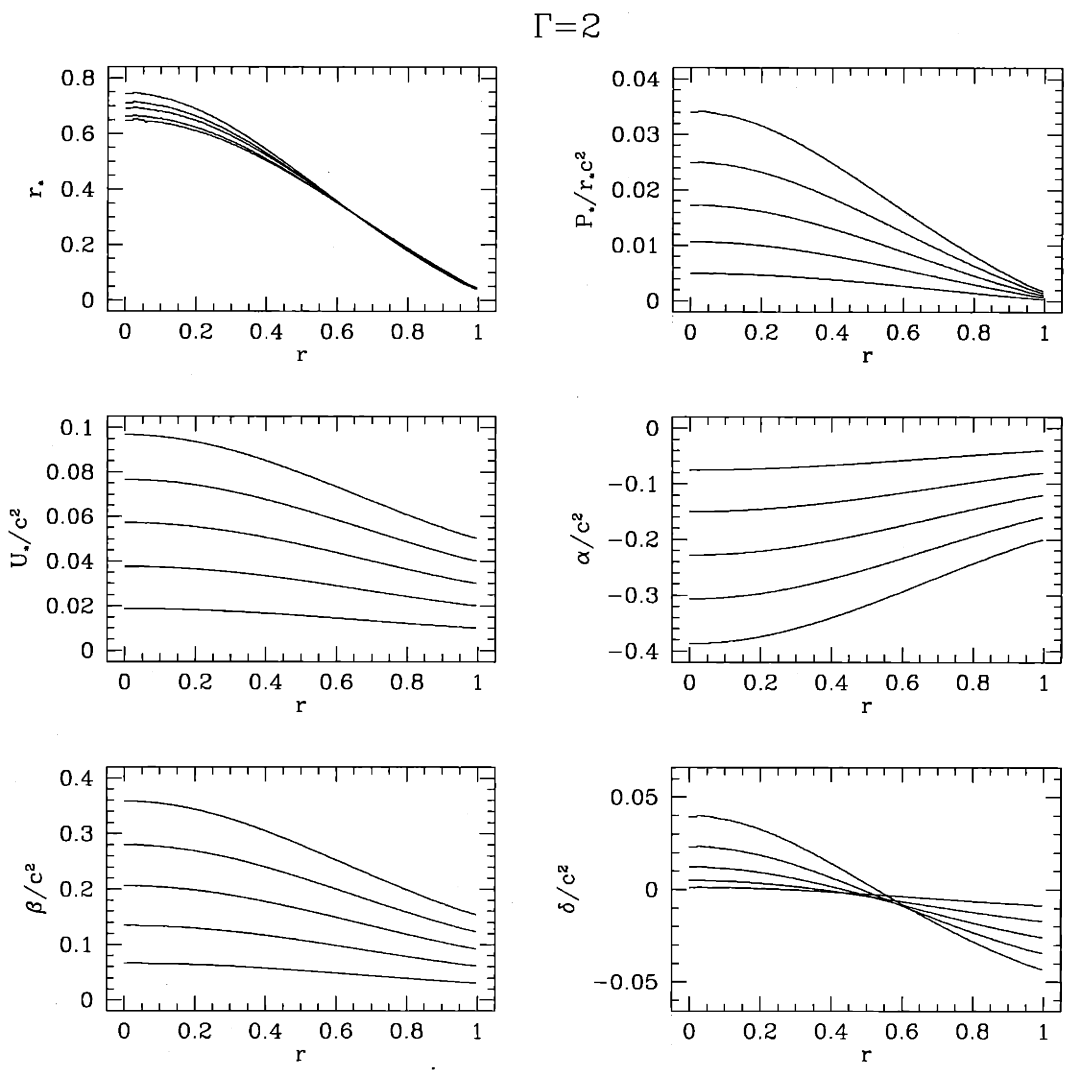

Figure 3-3: Radial profiles for the $\Gamma = 2$ single star models. The lines correspond, in monotonic fashion, to the stable configurations indicated by dotted lines in the middle panel of Fig. 3-1.

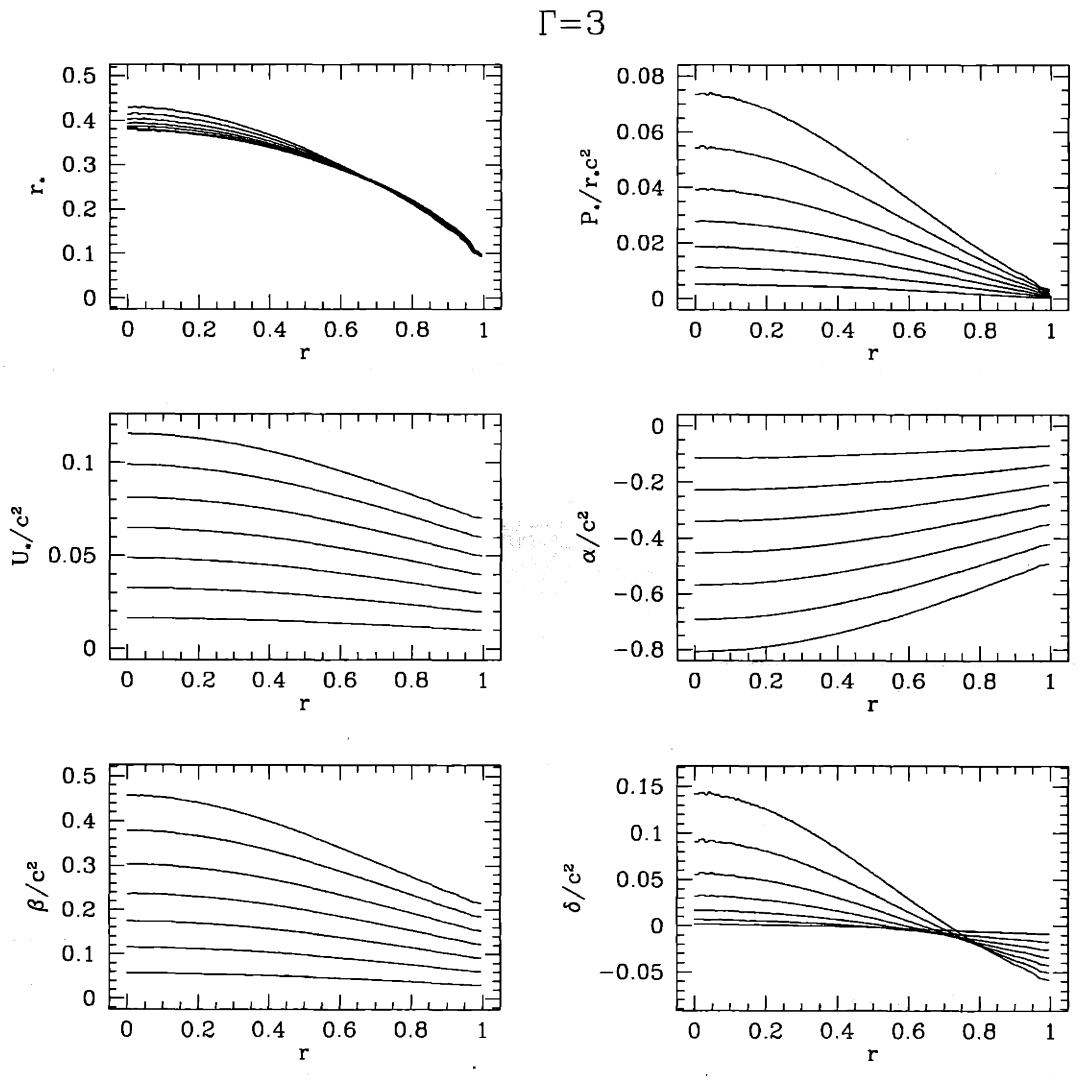

Figure 3-4: Radial profiles for the $\Gamma = 3$ single star models. The lines correspond, in monotonic fashion, to the stable configurations indicated by dotted lines in the right panel of Fig. 3-1.

M	R	$(r_*)_c$	$(P/r_*c^2)_c$	$(U_*/c^2)_c$
		$\Gamma = 2, k/k_N = 1.439$		
1.0	1.0	0.7490	0.0343	0.0968
0.8	1.025	0.5311	0.0243	0.0747
		$\Gamma = 3, k/k_N = 1.918$		
1.0	1.0	0.4051	0.0397	0.0813
0.9	0.986	0.3781	0.0349	0.0757
0.8	0.969	0.3501	0.0299	0.0683

Table 3.2: Properties of the PN polytropic models for NS of varying masses. Here the equation of state remains fixed for a given adiabatic index. All initial models have $1/c^2 = 0.05$. Quantities are defined as in Table 3.1.

layer of particles developing at the surface of the stars, with a slight density decrement immediately within, but involves only a very small fraction of the total mass of the system.

To construct models for the secondary NS for use in binaries with $q \neq 1$, we kept the same value of the polytropic constant k determined for a primary with $GM/Rc^2 = 0.05$, but we computed models with a lower mass using a relaxation technique. Note that, in contrast to their Newtonian counterparts, PN polytropes do not obey a simple power-law mass-radius relation, and therefore models for the secondary cannot be obtained simply by rescaling models for the primary. While Newtonian polytropes with $\Gamma = 2$ have a radius independent of the mass (for fixed k), the radius of a PN $\Gamma = 2$ polytrope increases with decreasing mass. The properties of NS models with lower masses are listed in Table 3.2.

3.4.2 Initially synchronized binaries

To construct synchronized systems, our single star models were placed in duplicate in a binary configuration, which was assumed to be in a state of synchronized rotation, i.e., the velocity of every SPH particle is given as a function of position by

$$\vec{v_0} = \vec{\Omega} \times \vec{r}. \tag{3.61}$$

The main difficulty in relaxing PN configurations is in the interplay between $\vec{v}$ and $\vec{w}$, which not only differ in magnitude but also in direction. Thus, one or the other can be relaxed in the corotating frame, but not both. Here $\vec{v}$ was assumed to be zero in the corotating frame for a relaxed configuration, satisfying the equation above.

We created a method to calculate $\vec{w}_0(\vec{v}_0)$, which is not invertible in closed form. As can be seen from Eq. 3.33, the relationship between particle velocity and momentum is a function of several potentials at the particle position, through the term containing A_i. Since A_i is itself a function of $\vec{w}$ (see Eq. 3.21), and vice versa, we need to solve consistently for both. It was found to be best to use an iterative procedure, which alternately solves for $\vec{w}$ and then uses these trial values in the source terms of the relevant Poisson equations.

In the initial step, using known values of $\vec{v}_0$, we first approximate $\vec{w}_0$ by the equations

$$\beta_{test} = \frac{1}{c^2}\left(3U_* + \frac{\Gamma}{\Gamma - 1}\frac{p_*}{r_*}\right) \tag{3.62}$$

$$\vec{w}_0 = \vec{v}_0\left(1 + \frac{\beta_{test}}{c^2} + \frac{v_0^2}{2c^2}\left[1 + \frac{\beta_{test}}{c^2}\right]^2\right). \tag{3.63}$$

The computed value of $\vec{w}$ enters into the source terms of both U_i and C_i in Eqs. 3.18 & 3.19. Using these two potentials, we calculate A_i and β from Eqs. 3.21 & 3.23, and recalculate a new approximation to $\vec{w}_0$, denoted $\vec{w}_{new}$, from the previous one, $\vec{w}_{old}$, by an iterative method, using only $\frac{1}{3}$ of the correction to avoid overshooting, thus

$$\vec{w}_{new} = \frac{2}{3}\vec{w}_{old} + \frac{1}{3}\left(1 + \frac{\beta}{c^2}\right)\left(\vec{v}_0 - \frac{\vec{A}}{c^2}\right). \tag{3.64}$$

It was found that, for the models we tested, about ten iterations would give convergence to within 1 part in 10^3 to the correct value of $\vec{v}$ when compared to the value of $\vec{v}(\vec{w}_{new})$ calculated by Eq. 3.33. For every timestep afterwards, we followed the same iteration procedure, and about six iterations were found to produce the same convergence to the proper values.

Once convergence to an acceptable solution was found, forces were calculated, and $\dot{v}$ was estimated by finite differencing,

$$\dot{v}_{force} = \frac{\vec{v}(\vec{w}(t+dt)) - \vec{v}(\vec{w}(t))}{dt}. \tag{3.65}$$

We relax the binary models at fixed center-of-mass separation r, in the corotating frame, adjusting Ω such that the inward force of gravity is balanced exactly by the centrifugal force. At every time step, we calculate

$$\Omega = \sqrt{\frac{F_{in}^1 + F_{in}^2}{2r}}, \tag{3.66}$$

where F_{in} refers to the net inward force on each component of the binary. Particle velocities are advanced according to

$$\dot{v} = \dot{v}_{force} - \frac{v}{t_{relax}} + \Omega^2 r. \tag{3.67}$$

After every time step, the two stars were adjusted slightly to maintain a center of mass separation at the desired value.

Setting up initially synchronized conditions for binaries which use Newtonian gravity but include radiation reaction effects is much simpler. In the regime where the dynamical timescale of the neutron stars is much smaller than the characteristic timescale for gravitational radiation, we expect the stars to evolve through a series of quasi-equilibrium configurations. If synchronized rotation is assumed, these equilibrium configurations can be constructed by adding a centrifugal force and drag term to the acceleration equation, giving us

$$\dot{v}_i = F_i^{hydro} - \nabla_i(\Phi + \Phi_{rot}) - \frac{v_i}{t_{relax}}, \tag{3.68}$$

where the centrifugal potential is given by

$$\Phi_{rot} = \frac{1}{2}\Omega^2(x^2 + y^2). \tag{3.69}$$

The relaxation timescale, t_{relax} is set initially to 1.0, close to the value required for critical damping of oscillations (RS1). For the purposes of relaxation, the radiation back-reaction, which is time-asymmetric, is ignored. In addition, during the relaxation, we ignore the distinction between velocity and momentum vectors in Eq. 3.45, taking $\vec{v} = \vec{w}$. The rate of rotation is calculated as in the PN case by Eq. 3.66. Once the binary has relaxed to a suitable initial configuration, it is set in motion, and we commence the dynamical run. Initial velocities are given by

$$\vec{w}_x = -\Omega y, \ \vec{w}_y = \Omega x, \tag{3.70}$$

and $\vec{v}$ is calculated from $\vec{w}$ by Eq. 3.33. In the point mass limit, this would reduce to Eq. 35 of Ruffert, Janka, and Schäfer (1996), who use

$$v_r = -\frac{16}{5}\frac{M^3}{r^3} \tag{3.71}$$

as their initial condition.

3.4.3 Initially irrotational binaries

Since there is no simple way to relax an irrotational binary configuration, to strict equilibrium, we used the results of Lombardi, Rasio, and Shapiro (1997) to construct approximate initial conditions. They calculated PN equilibrium solutions for irrotational binary NS with polytropic EOS, assumed to have self-similar ellipsoidal density profiles, with the density as a function of radius given by the 1PN expansion of the Lane-Emden equation. Approximate solutions were determined by minimizing the total energy of the binary configuration, including 1PN terms. The resulting NS models are the compressible, PN analogues of the classical Darwin-Riemann ellipsoids for incompressible fluids (Chandrasekhar 1987, LRS1). Here, we transform our single star models linearly in three dimensions into triaxial ellipsoids with the proper axis ratios.

For equal mass binaries, and an initial separation given by $r_0 = 4.0R$, we find

from Table III that the axis ratios are given by $a_1/R \simeq 1.02$, $a_2/a_1 \simeq 0.96$, and $a_3/a_1 \simeq 0.96$, where a_1, a_2, and a_3 are taken to lie along the binary axis (x-direction), the direction of the orbital motion (y-direction), and the rotation axis (z-direction), respectively. For binaries with an initial separation of $r_0 = 3.5R$, we find $a_1/R \simeq 1.05$, $a_2/a_1 \simeq 0.93$, and $a_3/a_1 \simeq 0.93$. We adapt the initial velocity pattern of the material to the ellipsoidal configuration, so that the initial velocity is given by

$$v_x = -\Omega y \left(1 - \frac{2a_1^2}{a_1^2 + a_2^2}\right) \tag{3.72}$$

$$v_y = \Omega y \left(1 - \frac{2a_2^2}{a_1^2 + a_2^2}\right). \tag{3.73}$$

It can be verified that this initial velocity field yields zero vorticity in the inertial frame.

Calculating the proper value of Ω proves to be much more difficult in PN gravity than in Newtonian gravity. In Newtonian gravity, the gravitational attraction between two NS is independent of the tidal deformations of the bodies to lowest order. Thus, even if the initial configuration of the binary is only near equilibrium, the orbit calculated for the two stars will be almost perfectly circular (assuming that gravitational wave damping is ignored). In PN gravity, the situation is radically different. From the PN expression of the gravitational force, Eq. 3.29, which includes terms proportional to the density of the NS, we see that radial oscillations of each star about equilibrium will produce an ellipticity in the orbit, although the period will related to the dynamical timescale for each NS, not the orbital period.

To account for this problem, we alter the standard formula for calculating the binary angular velocity to account for deviations from the equilibrium value, by admitting a correction factor κ, such that

$$\Omega = \kappa \sqrt{\frac{F_{in}^1 + F_{in}^2}{2r_0}}, \tag{3.74}$$

where F_{in}^1 and F_{in}^2 are the net forces inward acting on the respective members of the binary. For a Newtonian calculation, $\kappa \simeq 1.0$. For our PN calculations, we calculate

orbits for $\kappa > 1.0$, with radiation reaction drag forces turned off, until we find a value of κ for which the binary separation at the end of the orbit has changed by no more than 0.1%. Typically, the value of κ in our runs is in the range $\kappa \approx 1.1 - 1.115$. In the top half of Fig. 3-5, we show the binary separation as a function of time for several runs, all of which have equal-mass irrotational NS with a $\Gamma = 3$ EOS, but different values of κ. All runs except the curve represented by the thick solid line have radiation reaction effects turned off. For $\kappa = 1.111$, we find that the binary executes a nearly circular orbit. For other values of κ the orbit shows the quadratic deviation from circularity characteristic of an elliptical orbit. The thick solid curve shows the effect of turning on radiation reaction effects, resulting in a slow binary inspiral. The bottom half of the figure shows in more detail the effect of radial oscillations on the binary separation, plotting the radial acceleration of the binary and the central density of the NS as a function of time. We see a clear correlation between the maximum density of the respective NS, shown as a dashed curve, and the outwardly directed acceleration of the binary, shown as a solid curve. The numerical scatter is an artifact of the small number of particles located in the very center of each NS for the density curve, and of precision limits in the calculation for the acceleration curve. When averaged over time, we see nearly perfect correlation between the two quantities.

3.5 Summary of calculations

We have performed several large-scale SPH calculations of NS binary coalescence, primarily for the equal-mass case, as well as a series of runs designed to study the effect of varying the mass ratio q. Table 3.3 summarizes the relevant parameters of all runs performed. We refer to all runs that included both 1PN and 2.5PN effects as "PN runs", while those runs performed without 1PN corrections are referred to as "N runs." Note that all runs include the 2.5PN gravitational radiation reaction effects. We did not perform any new completely Newtonian calculations (except for a brief test run mentioned in Sec. 5.1).

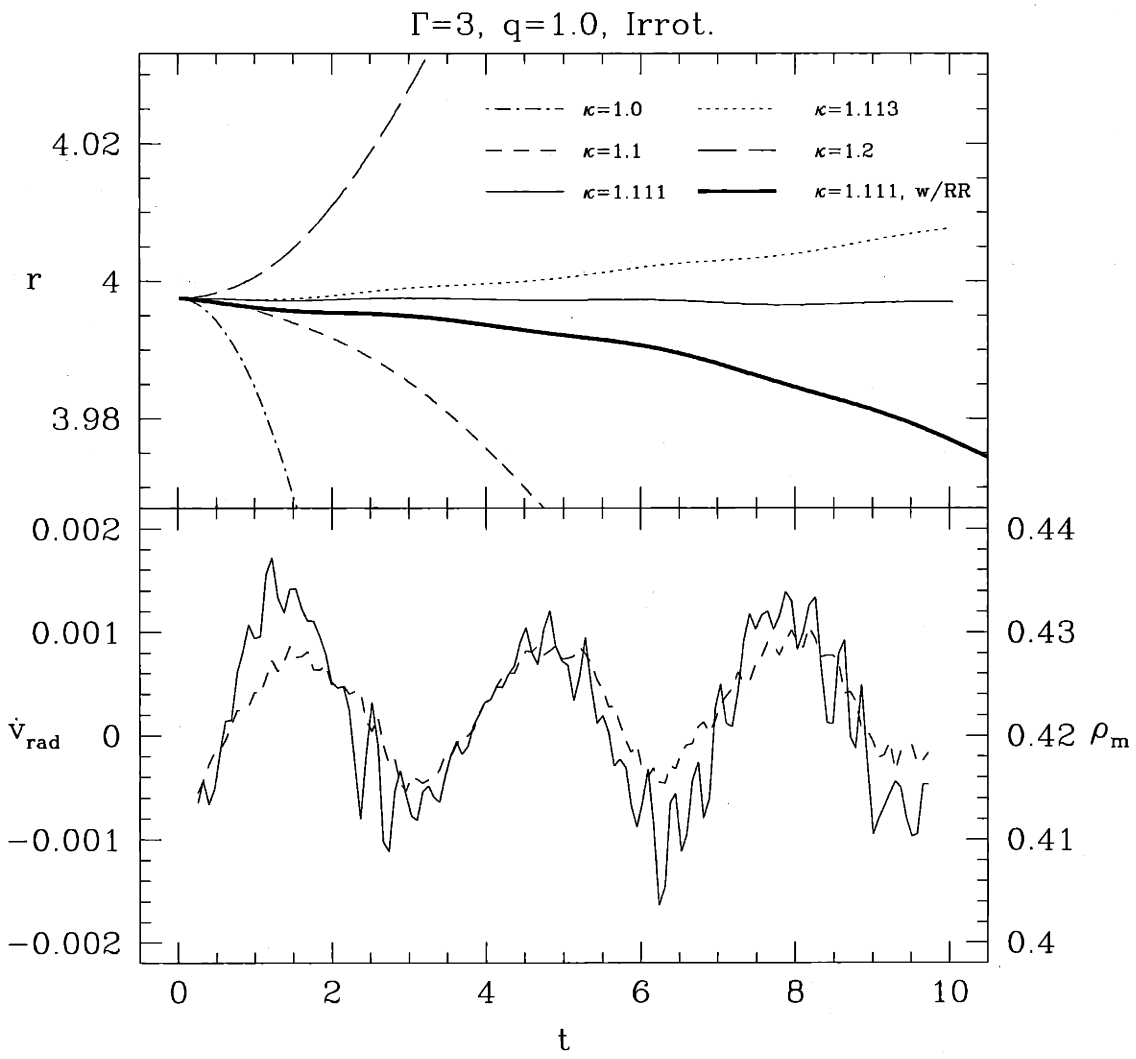

Figure 3-5: The binary separation as a function of time for runs without radiation reaction effects and $\kappa = 1.0$ (dot-dash), $\kappa = 1.1$ (short dash), $\kappa = 1.111$ (thin solid), $\kappa = 1.113$ (dotted), and $\kappa = 1.2$ (long dash), as well as for a run with $\kappa = 1.111$ including radiation reaction effects (thick solid). In the bottom panel, we show the radial acceleration of the binary system for the run with $\kappa = 1.111$ (solid) plotted against the maximum density in the system (dashed) as a function of time, finding excellent correlation.

All runs, unless otherwise noted, use 5×10^4 SPH particles per NS (i.e., the total number of particles $N = 10^5$), independent of q. The number of SPH particle neighbors is set $N_N = 100$ for these runs. Shock heating, which is normally treated via an SPH artificial viscosity, was ignored, since it plays a negligible role in binary coalescence, especially for fluids with a very stiff EOS. All Poisson equations were solved on grids of size 256^3, including the space for zero-padding, which yields the proper boundary conditions. All PN runs were done using $1/c_{1PN}^2 = 0.05$ and $c_{2.5PN} = 2.5$. Since we have an ambiguity in defining the relative time coordinate for different runs, we redefine the initial time t_0 of each run in such a way that the time of the first gravity wave luminosity peak $t_{\rm max}^{(1)} = 20$. As a result, all runs start before $t = 0$ (the starting time t_0 for each run is given in the third column of Table 3.3).

Run A1 is a Newtonian run with a binary containing two identical NS modeled as $\Gamma = 3$ polytropes. This run uses Newtonian gravity with radiation reaction (2.5PN) corrections, and started from an initial separation $r_0 = 3.1\,R$. Runs A2, A3, A4, and A5 feature the same initial conditions, but have mass ratios $q = 0.95$, 0.90, 0.85, and 0.80, respectively. Unlike A1, in which the simulation ran until a stable triaxial remnant was formed, runs A2–A5 were terminated after the completion of the first peak in the gravity wave luminosity.

Run B1 is a PN run, also for two identical $\Gamma = 3$ polytropes, but with 1PN and 2.5PN corrections included, and an initial separation of $r_0 = 4.0R$. Runs B2 and B3, like their Newtonian counterparts, correspond to mass ratios $q = 0.9$ and 0.8, respectively, and the same shorter integration time.

Run C1 is a Newtonian run (with radiation reaction effects) for two identical $\Gamma = 2$ polytropes. Since the ISCO for this softer EOS is located at smaller binary separation than for $\Gamma = 3$ (Lombardi, Rasio, & Shapiro 1997), we start this run with $r_0 = 2.9\,R$. As a test, we compared the results of this run to one with all identical parameters but with a slightly larger initial separation, $r_0 = 3.1\,R$, and found no measurable differences. Run C2 has a mass ratio of $q = 0.8$ and the same EOS and initial separation. Runs D1 and D2 are the 1PN counterparts of C1 and C2, with $\Gamma = 2$, an initial separation $r_0 = 4.0\,R$, and $q = 1$ and $q = 0.8$, respectively. Run C2

was terminated after the first gravity wave luminosity peak, whereas run D2 was continued until a stable remnant configuration was reached, to allow for comparison with D1.

All the previous runs started from a synchronized initial binary configuration. In contrast, run E1 started from an irrotational initial condition, with the EOS, mass ratio, and initial separation as in run B1, and including all 1PN and 2.5PN terms. It was continued until a stable remnant configuration was reached. Run E2 had the same $\Gamma = 3$ EOS, but a mass ratio of $q = 0.8$, and was started from a smaller initial separation of $r_0 = 3.5\,R$, since binaries with smaller masses take longer to coalesce. Runs F1 and F2 are similar to E1 and E2 in every way, but use a $\Gamma = 2$ EOS instead.

Finally, for the sake of testing our irrotational initial condition, we performed three runs which were primarily designed to test the dependence of the physical results of the calculation on numerical issues. We performed one run which was identical to E1, with the exception of the initial separation being set to $r_0 = 3.5\ R$. This run was used to study whether or not irrotational runs would maintain the proper rotation profile during the early stages of inspiral, and what affect any tidal synchronization effects would have on the gravity wave signal or other measured quantities.

We also performed runs which differed from the previous testing run by the number of particles used. We computed coalescences using 5000 and 500,000 SPH particles per NS (for a total of $N = 10^4$ and $N = 10^6$ particles, respectively), to study the effect of numerical resolution on calculations which should develop numerical instabilities on small scales. The nearest number of neighbors was adjusted in the two runs to be $N_N = 50$ and $N_N = 200$, respectively. The primary consideration behind this choice was the high computational cost of million particle runs, which encourage setting the initial separation r_0 as small as possible to maximize the use of resources available.

In Table 3.3 we list the gravitational formalism (N or PN), the adiabatic exponent Γ, the initial spin, the mass ratio q, the initial separation r_0, and the log of the number of SPH particles $\log_{10} N$ used for each of the runs described in detail in the remaining chapters of this work.

In Table 3.4, we show quantitatively some basic numbers pertaining our gravity

Run	Gravity	Γ	Spin	q	r_0	$log_{10}N$
A1	N	3.0	Synch.	1.00	3.1	5
A2	N	3.0	Synch.	0.95	3.1	5
A3	N	3.0	Synch.	0.90	3.1	5
A4	N	3.0	Synch.	0.85	3.1	5
A5	N	3.0	Synch.	0.80	3.1	5
B1	PN	3.0	Synch.	1.00	4.0	5
B2	PN	3.0	Synch.	0.90	3.5	5
B3	PN	3.0	Synch.	0.80	3.5	5
C1	N	2.0	Synch.	1.00	2.9	5
C2	N	2.0	Synch.	0.90	2.9	5
C3	N	2.0	Synch.	0.80	2.9	5
D1	PN	2.0	Synch.	1.00	4.0	5
D2	PN	2.0	Synch.	0.80	3.5	5
E1	PN	3.0	Irrot.	1.00	4.0	5
E2	PN	3.0	Irrot.	0.80	3.5	5
F1	PN	2.0	Irrot.	1.00	4.0	5
F2	PN	2.0	Irrot.	0.80	3.5	5
T1	PN	3.0	Irrot.	1.00	3.5	4
T2	PN	3.0	Irrot.	1.00	3.5	5
T3	PN	3.0	Irrot.	1.00	3.5	6

Table 3.3: Input parameters for the runs described in this work. Gravity refers to the use of either our 0+2.5PN formalism (N), or our hybrid BDS-based scheme (PN). The initial spins for all runs were either synchronized (Synch.) or irrotational (Irrot.). All runs featured 10^5 total SPH particles, except testing runs T1 and T3, with 10^4 and 10^6 SPH particles, respectively. Testing run T2 differs from run E1 only in the initial separation, but otherwise contains no differences.

wave results, as well as the initial time for all runs, and the tidal lag angle θ_{lag} which existed at the moment of first contact. As mentioned above, all our runs start at different initial times t_0, since we align the relative times such that the peak gravity wave luminosity occurs at $t = 20$. During the coalescence, the NS tend to get misaligned with the axis connecting the two stars. As the NS continuously try to maintain equilibrium while the coalescence timescale gets shorter and shorter, a lag angle develops. The inner edge of each NS rotates forward relative to the binary axis, and the outer edge of each NS rotates backward. We define θ_{lag} to be the angle in the horizontal plane between the axis of the primary moment of inertia in the binary and the axis connecting the centers of mass of the respective NS. For equal-mass systems, the angle is the same for both NS. For binaries with $q < 1$ we always find a larger lag angle for the secondary than the primary. These effects are described in detail in the remaining chapters.

Each gravity wave signal we compute typically shows an increasing gravity wave luminosity as the stars approach contact, followed by a peak and then a decline as the NS merge together. Most runs then show a second gravity wave luminosity peak of smaller amplitude. For all of our runs we list the maximum gravity wave luminosity L_{max} and maximum gravity wave amplitude h_{max}, where we compute the gravity wave amplitude as

$$h \equiv \sqrt{h_+^2 + h_\times^2} \tag{3.75}$$

for both the first and second peaks, assuming the latter exists, denoting the respective quantities by labels "1" and "2". In addition, we show the time $t^{(2)}$ at which the second peak occurs.

We continued several of our runs to late times to study the full gravity wave signal produced during the coalescence, as well as to study the properties of the merger remnants that may form in these situations. For each of these runs, we list several of the basic parameters of the merger remnant in Table 3.5, using the values computed for the remnant at $t = 65$. We identify the remnant mass M_r, defining the edge of the remnant by a density cut $r_* > 0.005$, as well as the gravitational mass

Run	t_0	$\theta_{lag}(deg)$	$c^5L^{(1)}$	$c^4(dh^{(1)})$	$c^5L^{(2)}$	$c^4(dh^{(2)})$	$t^{(2)}$
A1	-13	4.2	0.406	2.247	0.062	0.642	33
A2	-15	3.0, 3.5	0.328	2.050			
A3	-18	3.0, 3.7	0.262	1.844			
A4	-22	3.0, 4.8	0.204	1.654			
A5	-27	3.0, 5.0	0.157	1.485			
B1	-51	11.2	0.387	2.124	0.121	0.897	37
B2	-15	10.3, 11.1	0.228	1.799			
B3	-20	9.1, 12.1	0.122	1.529			
C1	-13	4.0	0.583	2.383	0.072	0.567	38
C2	-13	5.1, 11.5	0.089	1.363			
D1	-102	11.0	0.481	2.128	0.050	0.542	30
D2	-35	5.2, 10.1	0.088	1.445	0.053	1.090	31
E1	-86	7.5	0.374	2.023	0.093	0.807	33
E2	-39	6.5, 8.4	0.156	1.524	0.045	0.602	35
F1	-105	10.0	0.479	2.129	0.050	0.545	30
F2	-55	3.8, 12.1	0.098	1.364	0.056	0.564	35
T1	-21	7.8	0.358	2.009	0.125	0.932	32
T2	-3	12.0	0.337	1.972	0.087	0.746	30
T3	-16	5.8	0.356	1.989	0.111	0.907	32

Table 3.4: Selected quantities from each of the simulations. Note that only some of the runs were extended until the second gravity wave peak to study the property of the remnant formed. All other runs were terminated shortly after the first gravity wave luminosity peak. Here t_0 is the time at which the run was started, and $\theta_{\rm lag}$ is the lag angle at first.contact, given for both NS (see Sec. 4.2). Quantities involving the first and second gravity wave luminosity peaks are labeled with superscripts (1) and (2).

run	M_r	M_{gr}	a_r	Ω_c	Ω_{eq}	a_1	a_2/a_1	a_3/a_1	I_2/I_1
A1	1.78	N/A	0.54	0.439	0.645	1.61	0.81	0.59	1.35
B1	1.89	1.83	0.72	0.737	0.488	1.77	0.92	0.53	1.32
C1	1.83	N/A	0.64	0.821	0.602	1.80	0.81	0.50	1.01
D1	1.90	1.84	0.71	0.782	0.510	1.76	0.92	0.53	1.19
E1	1.95	1.88	0.73	0.668	0.435	1.81	0.94	0.55	1.07
F1	1.94	1.79	0.81	0.838	0.436	1.83	0.96	0.49	1.01
T1	1.97	1.91	0.74	0.711	0.433	1.81	0.94	0.54	1.10
T2	1.97	1.91	0.74	0.735	0.414	1.80	0.98	0.57	1.07

Table 3.5: Properties of the Merger Remnants. Units are such that $G = M = R = 1$, where M and R are the mass and radius of a single, spherical NS. Here, M_r is the rest mass of the remnant, M_{gr} is its gravitational mass, a_r the Kerr parameter, Ω_c and Ω_{eq} are the angular rotation velocities at the center and at the equator, and the a_i's and I_i's are the radii of the principal axes and moments of inertia.

of the remnant in the PN runs, where the gravitational mass, which differs from the rest mass, is given by $M_{gr} \equiv \int r_*(1+\delta)d^3x$. Additionally, we list the Kerr parameter $a_r \equiv cJ_r/M_{gr}^2$, central and equatorial values of the angular velocity, Ω_c and Ω_{eq}, the semi-major axis a_1 and ratios of the equatorial and vertical radii a_2/a_1 and a_3/a_1, and the ratio of the principal moments of inertia I_2/I_1.

Chapter 4

Calculations in Newtonian and PN gravity

Note: This chapter is an edited version of an article that was published in Physical Review D (Faber & Rasio 2000), and is printed here with the editor's approval. My co-author was Frederic A. Rasio.

We start our study by examining two calculations of binary coalescence: Run A1, featuring Newtonian gravity, and B1, using PN gravity. Both simulations included radiation reaction throughout the entire run, treated in the formalism of Sec. 3.2. For both runs, we used 50,000 particles per NS (total of 10^5), with a $\Gamma = 3$ polytropic EOS. The two NS are identical. Synchronized rotation was assumed in the initial condition. The optimal number of neighbors for each SPH particle was set to 100. Shock heating, which plays a completely negligible role in the case studied here, was ignored. All Poisson equations were solved on grids of size 256^3, including the added space necessary for zero-padding. For the 1PN run, we used a compactness parameter $1/c_{1PN}^2 = 0.05$ (see Sec. 3.3). In both runs, we used $c_{2.5PN} = 2.5$ in calculating radiation reaction terms. Run A1 required a total of 600 CPU hours and Run B1 required 1200 hours on the NCSA Origin2000, including the relaxation phase. Particle plots illustrating qualitatively the evolution of the system are shown in Fig. 4-1 (A1) and Fig. 4-2 (B1).

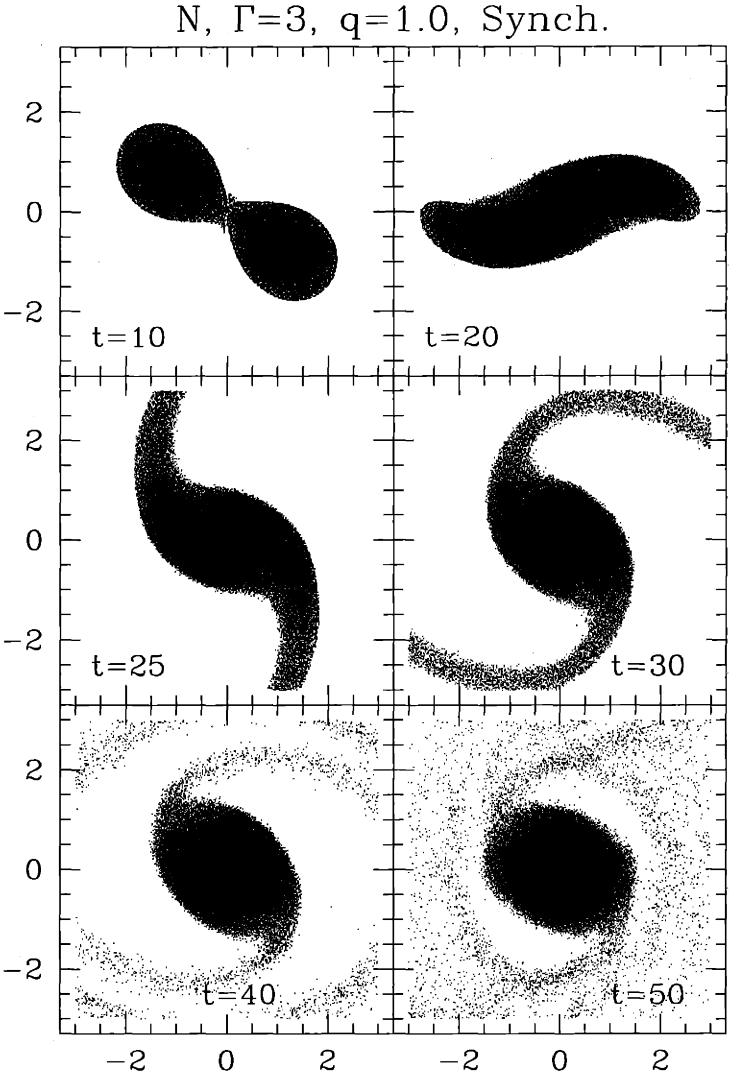

Figure 4-1: Evolution of the system in run A1. Projections of a all SPH particles onto the orbital (x-y) plane are shown at various times. The orbital motion is counter-clockwise. Units are such that $G = M = R = 1$, where M and R are the mass and radius of a single, spherical NS. Note that the development of a mass-shedding instability after $t \simeq 25$, and the rapid contraction of the remnant toward an axisymmetric state at late times.

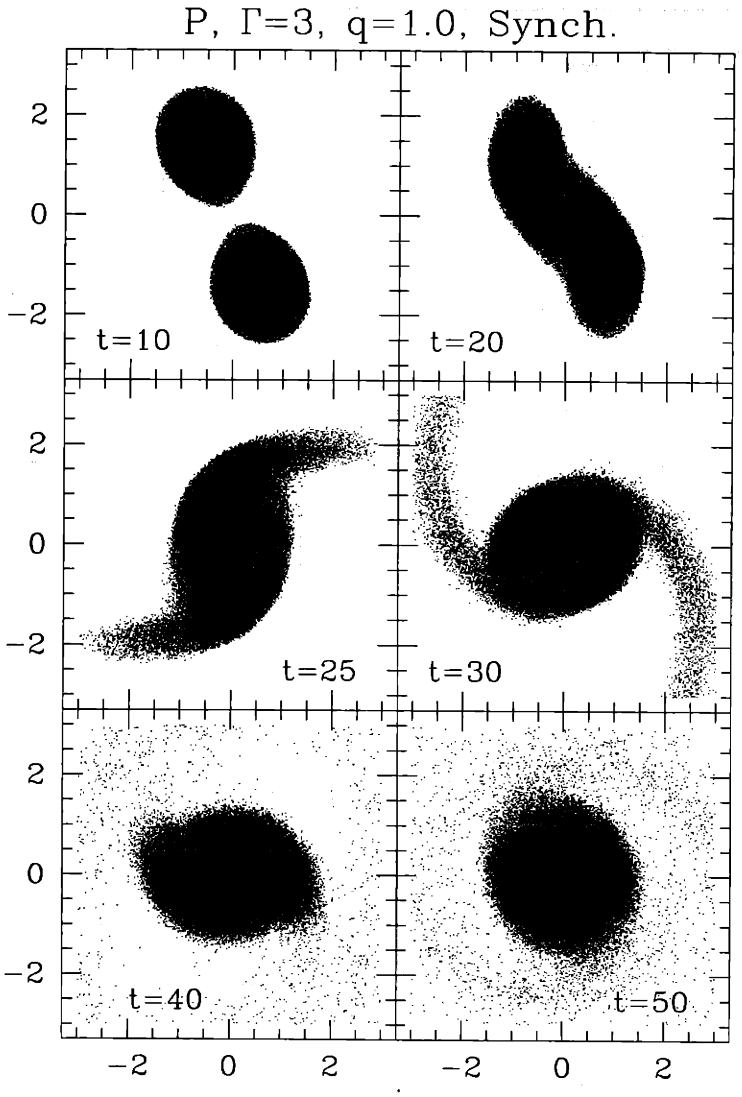

Figure 4-2: Evolution of the system in the PN run B1. Conventions are as in Fig. 4-1. We see in the initial frame that the long axes of the NS are misaligned before contact. Note also that the mass-shedding is suppressed compared to the Newtonian case.

4.1 Dynamical instability and the inspiral process

It was shown by RS and LRS that equilibrium configurations for close binary NS become dynamically unstable when the center of mass separation r is less than a critical value. For Newtonian, synchronized, equal-mass binaries with $\Gamma = 3$, the ISCO is at $r = 2.95\,R$. Purely Newtonian calculations for binaries starting from equilibrium configurations with a separation larger than this value will show no evolution in the system. Binaries starting from a smaller separation, though, are dynamically unstable, and coalesce within a few orbital periods, even without the energy and angular momentum loss due to radiation reaction (RS; New & Tohline 1997; Swesty, Wang, & Calder 2000).

In simulations with radiation reaction included, coalescence will always be the end result. The limiting factor on how large to make the initial separation is the computing time required for the binary orbit to slowly spiral inward. Ideally, one should make sure that the stars are in quasi-equilibrium when the orbit approaches the ISCO and the inspiral timescale undergoes a shift from the slow radiation-reaction timescale to the much faster dynamical timescale.

Since the effective gravitational attraction between two stars is increased by PN effects, we expect the ISCO to move outwards when 1PN corrections are included. This was demonstrated by Lombardi, Rasio, & Shapiro (1997), who used the same energy variational method as LRS to find equilibrium configurations for binary NS models including 1PN corrections. Taking into account these results, we used an initial separation of $r_0 = 3.1\,R$ for run A1, and $r = 4.0\,R$ for the PN simulation, run B1. As a consequence, there is an ambiguity in the relative time between the two runs, which we resolve by adjusting the initial time of both runs such that the maximum gravity wave luminosity occurs at the same time in each. This was found to require shifting the time in the N run backwards so that it starts at $t = -13$, while the PN run starts at $t = -51$.

In Fig. 4-3, we show the evolution of the center-of-mass binary separation during the initial inspiral phase for our runs. Fig. 4-4 shows the inspiral phase of the run

A1, as well as the inspiral tracks predicted by the classical quadrupole formula for two point masses, and by the methods of LRS3 for two corotating spheres and two ellipsoids. We note that the results of LRS3 predict for extended objects a significantly more rapid inspiral rate, which is confirmed by the numerical run. In addition, we note that the approach of the ISCO is clearly visible in the plots, where the inspiral rate switches from the slow radiation-reaction-driven orbital decay to the faster dynamical infall. This appears to happen at $r \simeq 2.7\,R$ in the Newtonian case, in good agreement with previous results.

Comparing the PN run to the Newtonian run, we see that the stability limit must lie at a larger separation. This agrees with the results of Lombardi et al. (1999), who find that PN corrections not only move the ISCO outward, but also flatten out the equilibrium binary energy curve $E(r)$ near the stability limit (where $E(r)$ reaches a minimum). Following the arguments of LRS3, we conclude that unstable inspiral begins when the rate of energy loss to gravitational radiation increases inspiral velocity in Eq. 1.37 to the point where the timescale on which the individual NS must react to changing conditions grows shorter than the dynamical timescale of the stars. The condition for unstable inspiral is then encountered further outside the ISCO (as determined for binaries in strict equilibrium), since PN corrections decrease the left-hand side. This effect can also be seen in the results of Ayal et al. (2001) by careful examination of their Fig. 5a. Even though the binary separation in their PN run has a large initial oscillation, caused by the use of non-equilibrium initial conditions, it still converges at a much more rapid rate than in their corresponding Newtonian model.

Even though the effective stability limits of Newtonian and PN binaries differ significantly, their actual inspiral velocities are very close before the moment of first contact, at a separation of $r \simeq 2.5\,R$, until the merger of the NS cores. The only significant difference is the break in the inspiral velocity for run A1 at $t \simeq 20$, which occurs as the cores start to come into direct contact with each other. The lack of this feature in the PN run will be explained in Sec. 4.2.

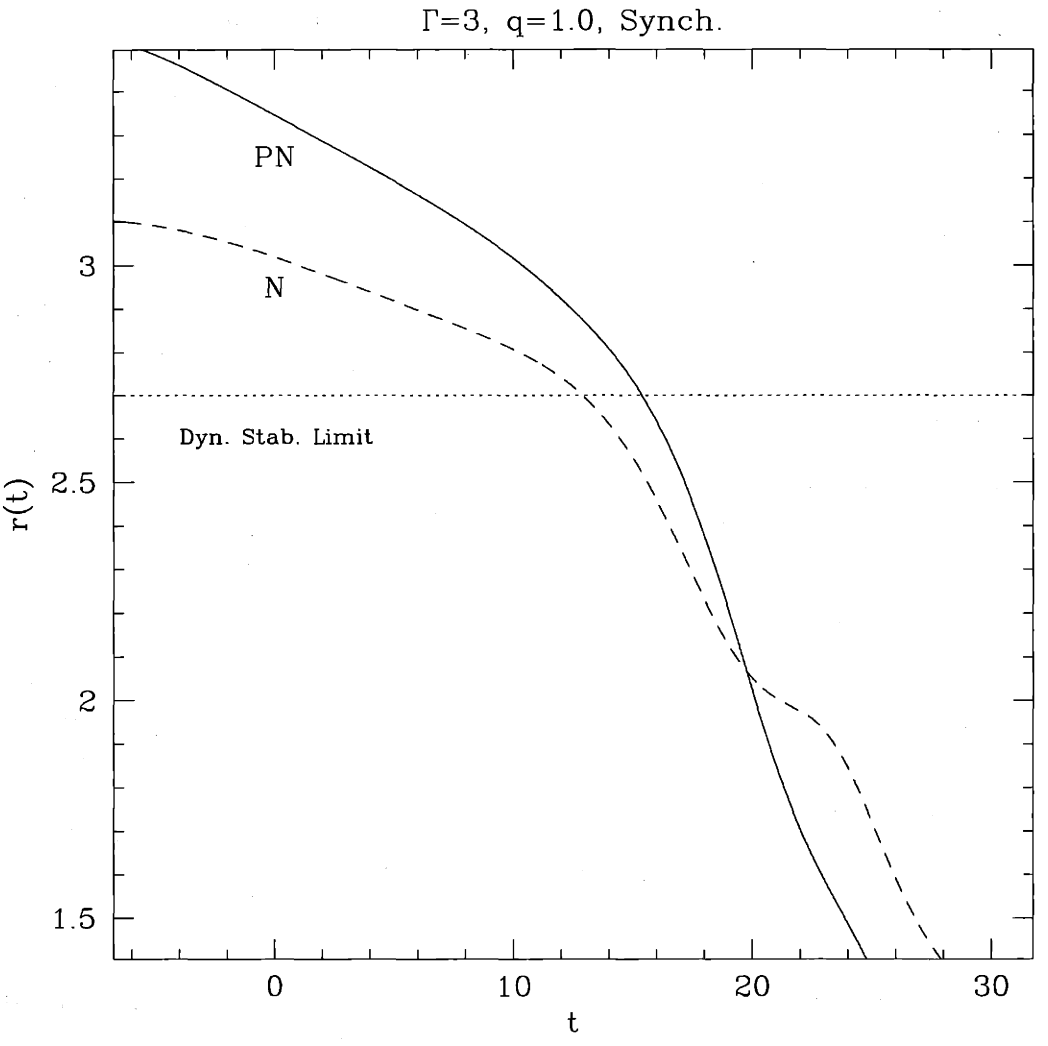

Figure 4-3: Evolution of the binary center of mass separation during the inspiral phase for the two calculations. The solid line is for the PN run B1, the dashed line for the Newtonian run A1. The horizontal line represents the dynamical stability limit for a Newtonian, equilibrium binary, at $r \simeq 2.7\,R$. The inspiral rate of the Newtonian binary shows a break at that separation, whereas the PN binary inspiral becomes dynamically unstable at a greater separation.

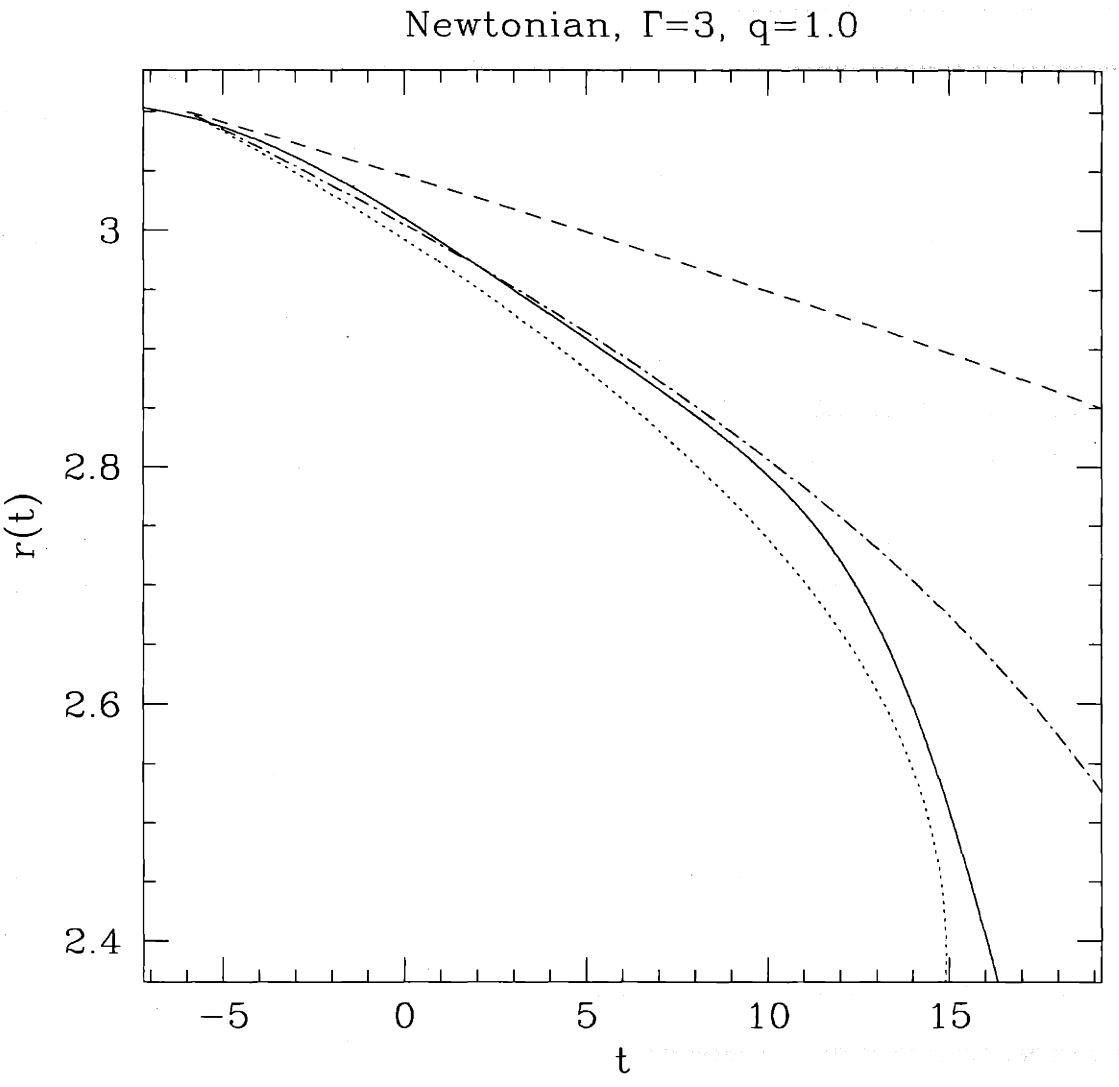

Figure 4-4: Same as Fig. 4-3, but focusing on the early inspiral of the Newtonian binary. The solid line is the result from the SPH calculation (N run). The dashed line shows the point-mass approximation, the dash-dotted and dotted lines the approximations for two spheres and two ellipsoids, respectively. See text for details. The point mass approximation clearly fails when tidal interactions become significant, but note the excellent agreement with semi-analytic results for extended stars before the ISCO is encountered.

4.2 Coalescence

In Fig. 4-5, we show the time evolution of the maximum density in both runs. The maximum density is at the center of either star initially, but it shifts eventually to the center of the merger remnant. The initial oscillations with a period of $T \simeq 2-3$ correspond to the fundamental radial pulsations of the polytropes, and represent the errors resulting from small departures from strict equilibrium in the initial conditions. We see that $\delta\rho/\rho \simeq 0.02$ and 0.01, respectively, for the Newtonian and PN runs, which provides a measure of the numerical accuracy of the initial conditions.

As the binary system contracts to separations of $r < 2.7\,R$, we see a rather sudden and rapid decrease in the maximum density found at the core of each star, corresponding closely with the moment of first contact of the two stars, after which the cores get tidally stretched. For run B1, this follows a gradual increase in the average density maximum, which is caused by the contraction of each NS in response to the growing gravitational potential of its companion, rather than a pure tidal effect. This effect, which seems to result primarily from the weakening of the pressure force in Eq. 3.28 as α becomes more negative in response to the growing gravitational potential (from Eq. 3.22), was also seen by Ayal et al. in one of their runs (2001, see their Fig. 6, run P3). When the center of mass separation reaches a value of $r \simeq 2.0\,R$ the maximum density stops decreasing, turning around and increasing sharply as the cores come into direct contact and merge.

In Fig. 4-6, we show the gravity wave signatures of both runs. The waveforms in the two polarizations of gravitational radiation are calculated for an observer at a distance d along the rotation axis of the system in the quadrupole approximation, given by Eqs. 1.21 and 1.22. In Fig. 4-7 we show the corresponding gravity wave luminosity of the system, given by Eq. 1.25. We see that, as the inner NS cores merge, the gravity wave luminosity peaks for both runs, with the characteristic frequency of the waves increasing like (twice) the rotation frequency of the system. This frequency increase is more rapid in the PN case, since the inspiral is faster.

After $t \simeq 30$, the evolution of the Newtonian binary is rather straightforward. A

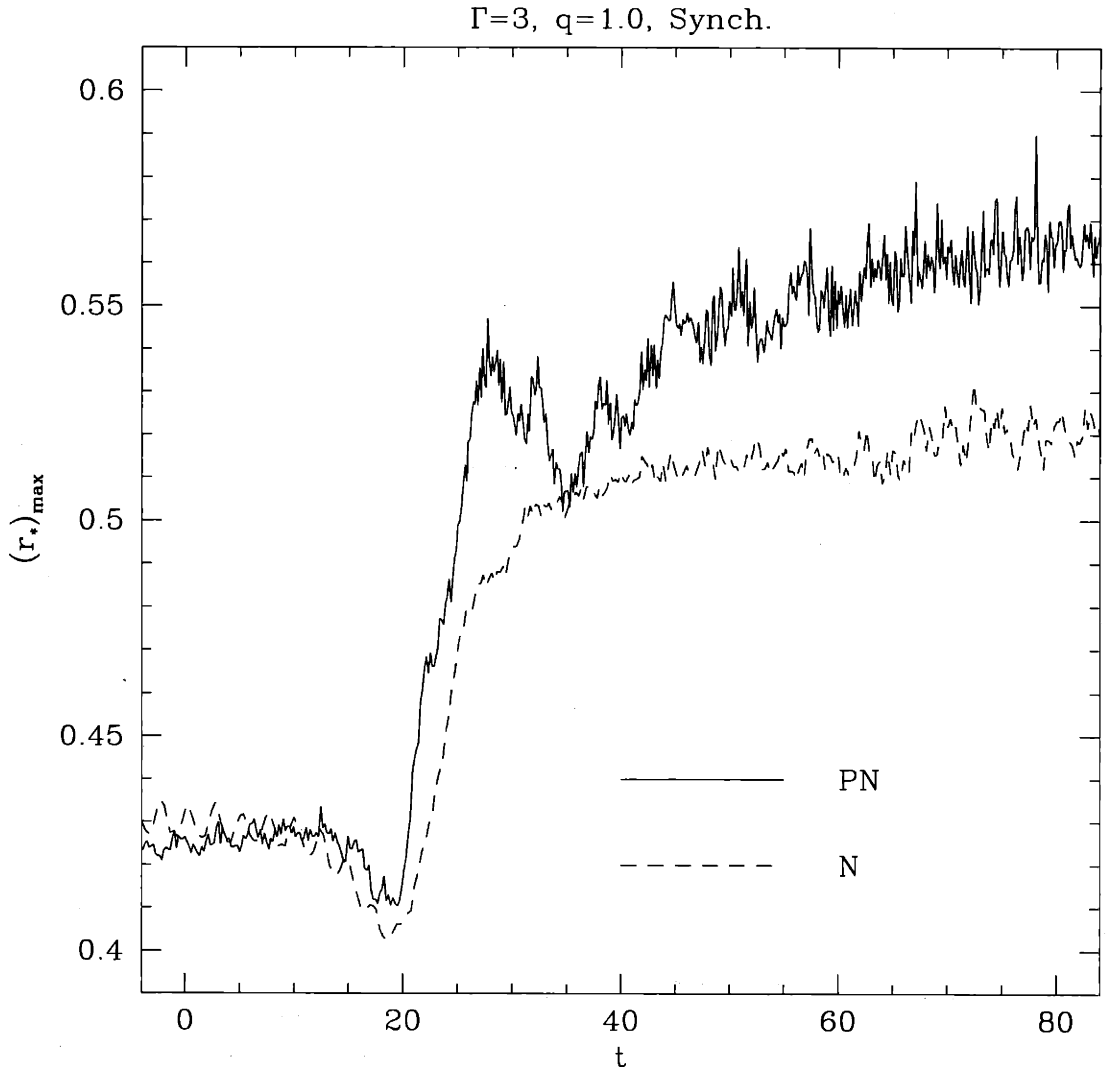

Figure 4-5: Evolution of the maximum density in the two coalescence calculations. The solid curve is for run B1, the dashed curve for the run A1. The sharp decline in density at $t \simeq 15$ occurs as the two NS are tidally disrupted, followed by a larger increase as they coalesce.

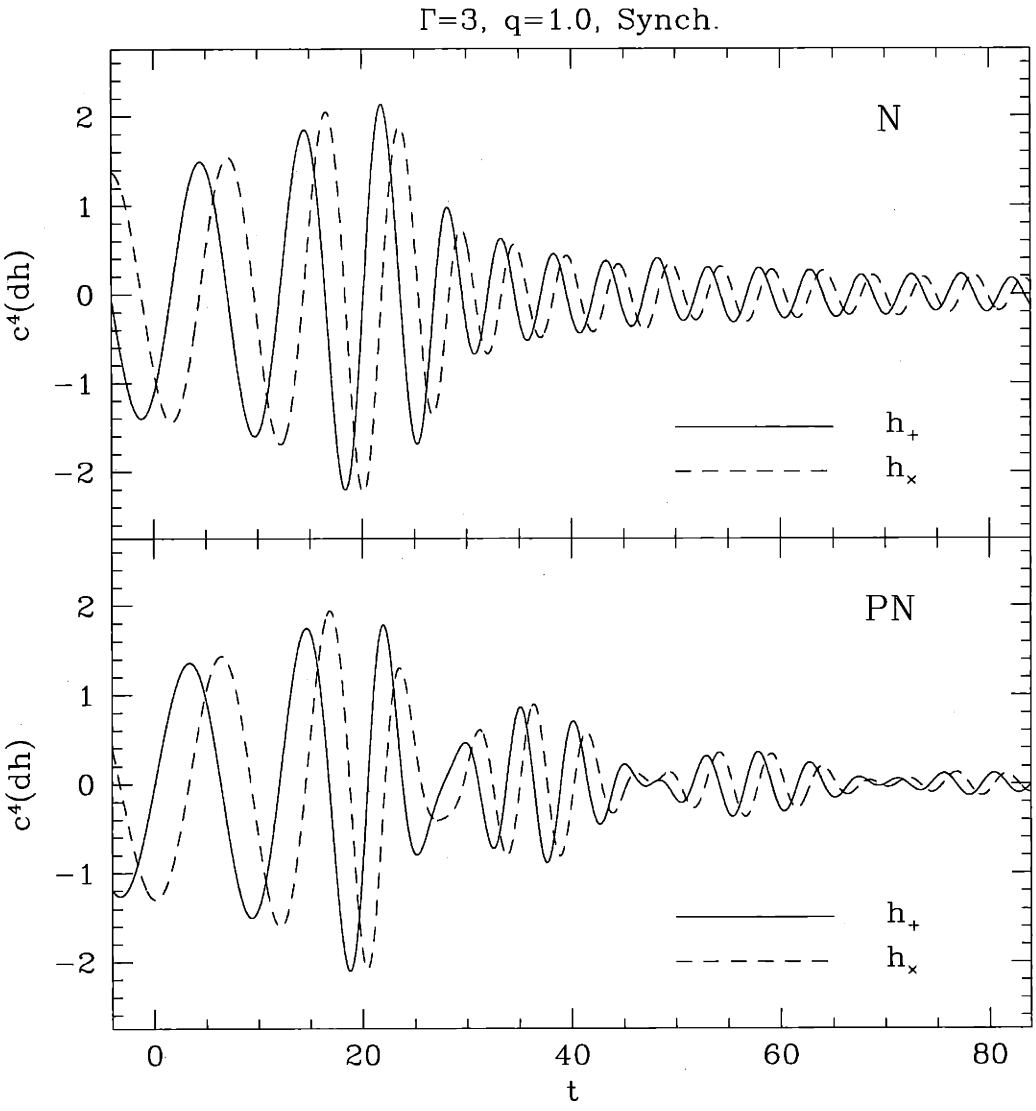

Figure 4-6: Gravity wave signatures for the two coalescence runs. The waveforms are calculated for an observer at a distance d along the rotation axis. The solid line shows the h_+ polarization, the dashed line the $h_\times$ polarization (see Eqs. 1.21 and 1.22). At late times in the Newtonian run A1 the waveforms show a simple, exponentially damped oscillation, whereas in the PN run B1 an additional large-amplitude modulation is apparent.

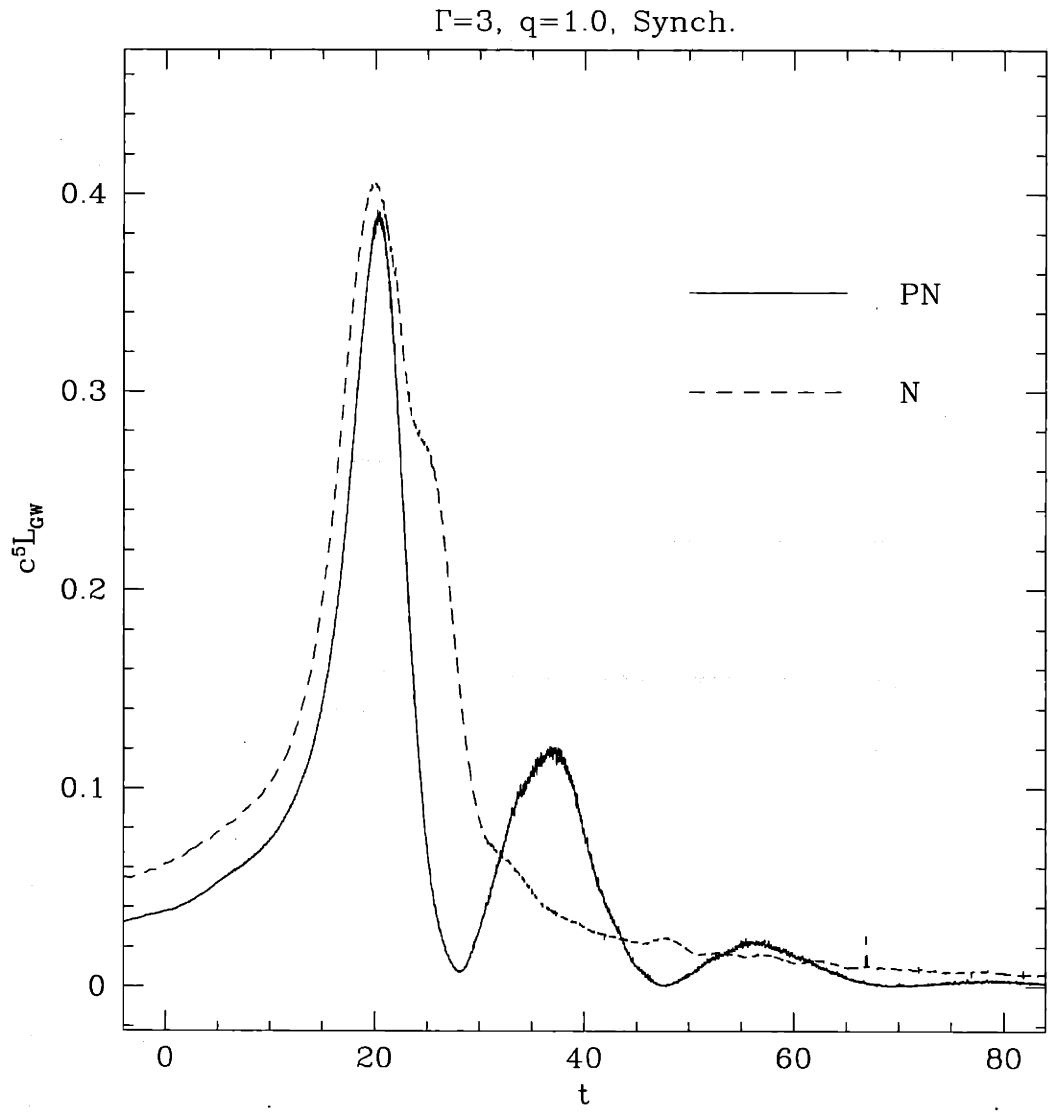

Figure 4-7: Gravity wave luminosity for the two coalescence runs (see Eq. 1.25). The solid line is for the run B1, the dashed line for the run A1. The peak luminosity in the PN run is similar that of the Newtonian run, but secondary peaks occur at $t \simeq 35$, 50, and 70.

triaxial object is formed at the center of the system, with spiral outflows emanating from the outer parts of each star. The spiral arms remain coherent for several windings before slowly dissipating, and finally leaving a low-density halo of material in the region $r/R \simeq 2 - 15$. During this time, the central triaxial object acts as the predominant source for the gravity waves as it spins down, leading to a characteristic damped oscillatory signature, at a luminosity approximately 1/30 that of the peak. The rise in central density from the initial value at $t = 0$ to the final value at $t = 80$ is consistent with what is expected from the mass-radius relation for a Newtonian polytrope with $\Gamma = 3$.

This simple picture, which is familiar from many previous Newtonian simulations, is seen to break down when 1PN effects are taken into account. As is clear from the upper left panel of Fig. 4-2, at $t = 10$, just prior to the final coalescence, 1PN effects cause the long axis of each star to rotate forward relative to the binary axis, so that the inner part of each star leads the center of mass in the orbital rotation. This dynamical tidal lag is expected from the rapidly changing tidal forces during the final inspiral phase (LRS5). It is not to be confused with the tidal lag produced by viscous dissipation in nonsynchronized binaries (Zahn 1992). The dynamical tidal lag angle can be estimated analytically for a Newtonian binary whose orbit decays slowly by gravitational wave emission. Using Eq. 9.21 of LRS5, we estimate a lag angle $\theta_{lag} \simeq 0.01$ for $1/c^2 = 0.16$ and $r \simeq 2R$. This is in agreement with the very small lag angle observed in our Newtonian run (barely visible at $t = 10$ in Fig. 4-1). In contrast, from our PN run, we find $\theta_{lag} \simeq 0.14$, indicating that the more rapid inspiral can dramatically increase this effect.

As the PN merger proceeds, material from the leading edge of each star wraps around the other, so that the cores simply slide past each other instead of striking more nearly head-on as in the Newtonian case. The result is a gravity wave peak of nearly the same amplitude, but of a shorter duration than that of the Newtonian calculation. At $t \simeq 25$, the maximum density drops slightly, and the gravity wave luminosity rises again, reaching a second peak at $t \simeq 37$, with a maximum luminosity $L_2 = 0.31\, L_1$ compared to the first peak of luminosity L_1. A cursory examination of Fig. 4-2 reveals

a highly asymmetric, triaxial configuration near this time. The subsequent oscillations of the two cores in their sliding motion against each other damp out rather quickly, and the central object becomes more nearly axisymmetric while the maximum density rises again. A third peak of maximum luminosity $L_3 = 0.08\,L_1$ is clearly visible near $t \simeq 57$, as is another very slight drop in the central density at that time, and a fourth, much smaller luminosity peak occurs at $t \simeq 78$.

To better understand this oscillation of the merger, and the corresponding modulation of the gravitational radiation waveforms, we show in Fig. 4-8 a comparison between the gravity wave luminosity and the ratio of the principal moments of inertia of the central object in run B1. As can be seen clearly, the two quantities are strongly correlated, except for the initial period where the binary is still merging. If we ignore the details of the internal motion of the fluid, it may be tempting to model the late-time behavior of the remnant in terms of a simple quadrupole ($l = 2$ f-mode) oscillation of a rapidly and uniformly rotating single star. Adopting an average value for the angular velocity of the central object, $\bar{\Omega}^2 = 0.4$, and using Eq. 3.30 of LRS5 for the frequency of the quadrupole oscillation of a compressible Maclaurin spheroid, we obtain a frequency $\sigma = 0.38$, which gives us a modulation period $T_{\rm mod} = 16.6$, very close to what we observe in Figs. 6 and 7.

The occurrence of a second peak in the gravity wave luminosity can also be seen in the PN calculations presented in Ayal et al. (2001) for polytropes with $\Gamma = 2.6$, but the second peak appears considerably less pronounced for $\Gamma = 2.6$ than for $\Gamma = 3$. This may simply result from the higher central concentration of objects with lower values of Γ, which decreases the emission of gravitational radiation for a quadrupole deformation of given amplitude. Grid-based Newtonian calculations by Ruffert et al. (1996) for nonsynchronized binaries with a different EOS also show a second peak in the gravity-wave luminosity. For Newtonian systems with $\Gamma < 2.2$, the merger remnant evolves quickly to axisymmetry and the emission of gravitational radiation stops abruptly after the first peak (RS1; RS2).

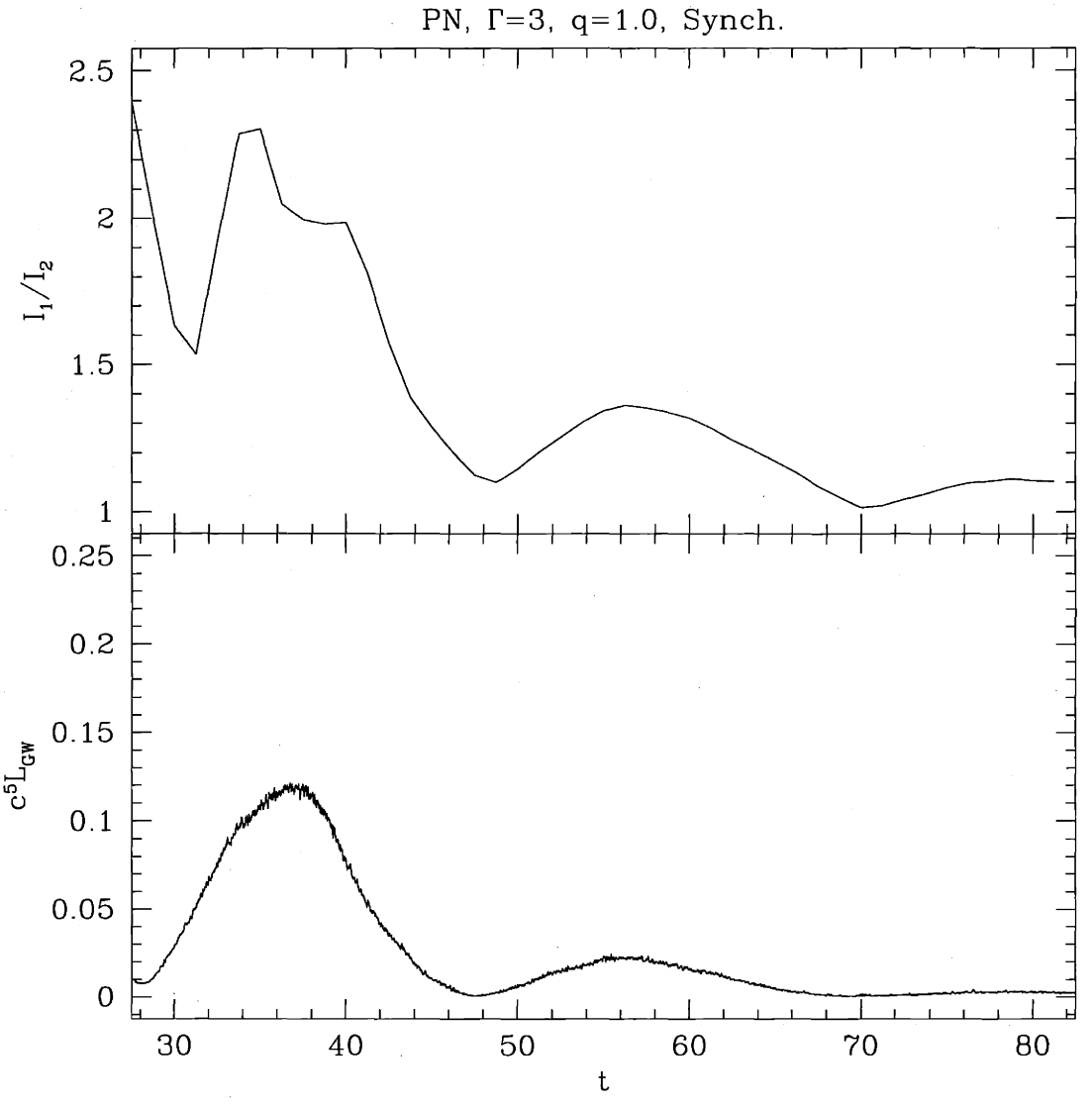

Figure 4-8: The ratio of the principal moments of inertia in the equatorial plane for the PN merger remnant of run B1, compared to the gravity wave luminosity at late times. The times of maximum elongation correspond to maxima in the gravity wave luminosity, and to decreases in the maximum density in Fig. 4-5 at $t \simeq 37$ and $t \simeq 57$ (and less clearly at $t \simeq 78$).

4.3 The final merger product

In Fig. 4-9, we show density contours of the central merger remnants in both the equatorial and vertical planes, defining the remnant to include all material with $r_* > 0.005$. In the top panels, for run A1, the remnant is shown at $t = 70$, which is at the end of the calculation. For run B1, we show the remnant at $t = 55$, which corresponds to the third gravity wave luminosity peak, and at $t = 70$, the end of the simulation and close to a gravity wave luminosity minimum. Axes for the contour plots are aligned with the principal axes of the remnant. A summary of values for the principal axes and moments of inertia for the three configurations is presented in Table 3.5.

We see that the final remnant in the PN calculation is larger and more centrally condensed than in the Newtonian case, with a higher degree of flattening in the vertical direction. This is in part because in the PN case less mass and angular momentum is extracted from the central region and deposited in the halo. Figures 4-10 and 4-11 show the evolution of the angular momentum of the various components in both runs. In run A1, most of the angular momentum lost by the remnant has gone into the halo. For run B1, nearly equal amounts of angular momentum are lost to the halo and to the gravity waves.

Nevertheless, the axis ratio a_2/a_1 in the equatorial plane is approximately the same for the run A1 at $t = 70$ and for run B1 at $t = 55$ and at $t = 70$, indicating a reasonably constant shape for the outermost region. Further comparison between the remnants, however, shows that their interior structures are remarkably different. In the PN remnant, the isodensity surfaces do not maintain a consistent orientation or shape as we move from the center to the equator of the remnant, indicating that the structure of the remnant is much more complex than that of a self-similar ellipsoid. Gravity-wave luminosity peaks are seen to occur when the inner and outer contours are aligned, leading to a larger net quadrupole moment (this is nearly the case at $t = 55$ in Fig. 4-9). Minima occur when the orientations lie at right angles, as can be seen near $t = 70$ for run B1 in Fig. 4-9.

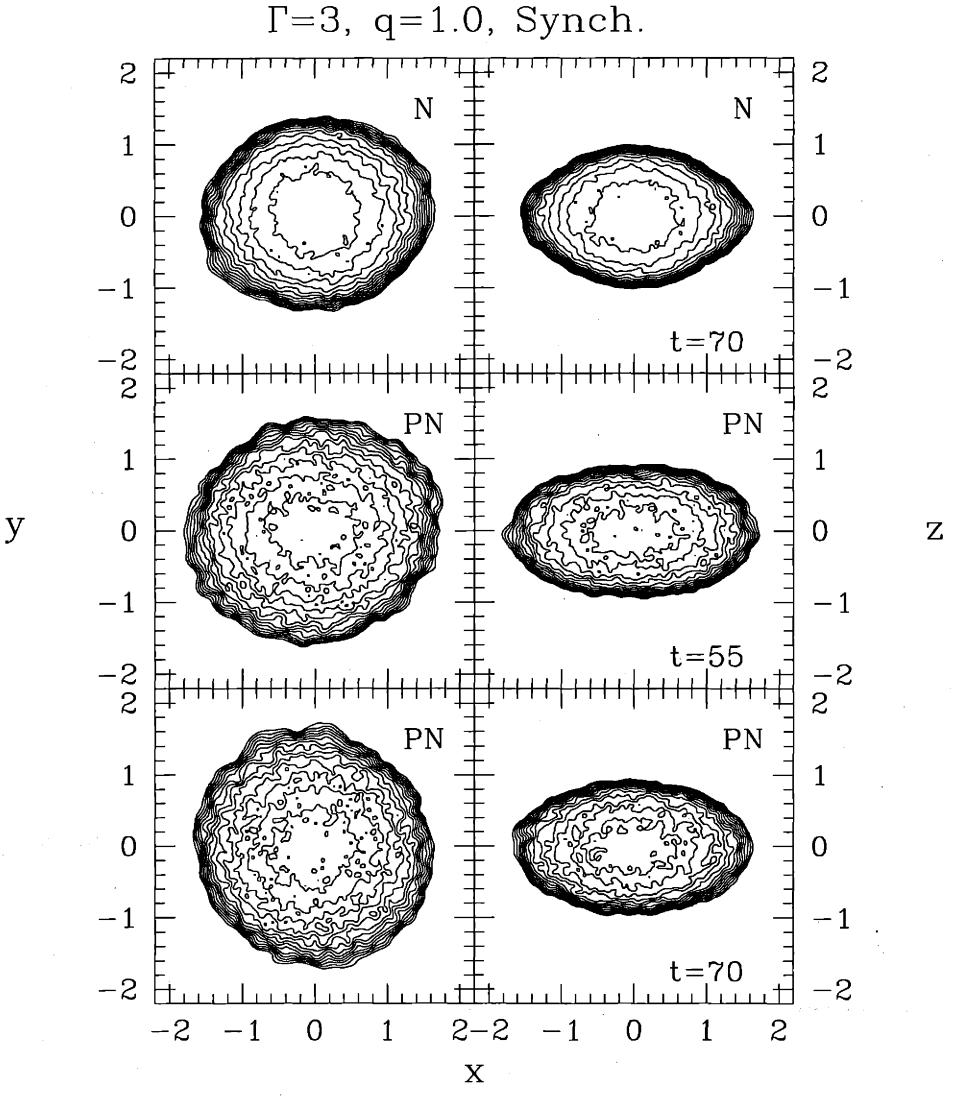

Figure 4-9: Density contours of the merger remnants. The top frames show the Newtonian remnant of run A1 at $t = 70$, the middle ones show the PN remnant of run B1 at $t = 5$, and the lower ones show the latter at $t = 70$. The left frames show a cut through the equatorial plane, the right frames through the vertical plane (containing the rotation axis). Contours are logarithmic, ten per decade, starting from the maximum density of $(r_*)_{max} = 0.567$ for the run B1 at $t = 55$, $(r_*)_{max} = 0.563$ for the run B1 at $t = 70$, and $(r_*)_{max} = 0.521$ for the run A1 at $t = 70$. The axes have been rotated to fall along the principal axes of the remnant. Note the cusp-like shape of the contours near the equator in the vertical plane, indicating maximal rotation.

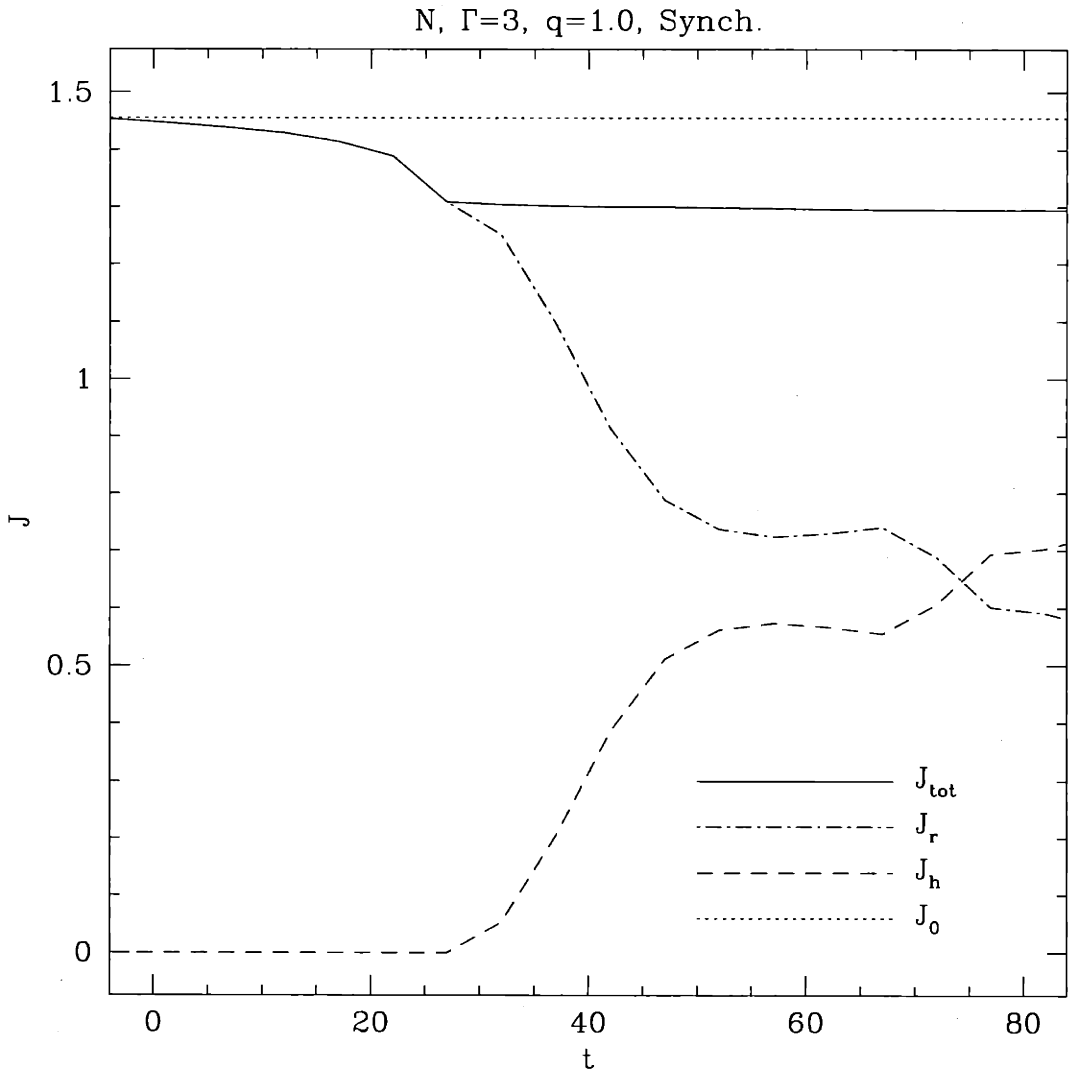

Figure 4-10: Evolution of the angular momentum in various components in the run A1. Here J_{tot} is the total angular momentum in the system, J_r is for the inner remnant (defined by the condition $r_* > 0.005$, which includes the entire binary initially, but only the inner remnant at later times), and J_h is for the outer halo (so that $J_{tot} = J_r + J_h$). The dotted line shows the initial angular momentum of the system.

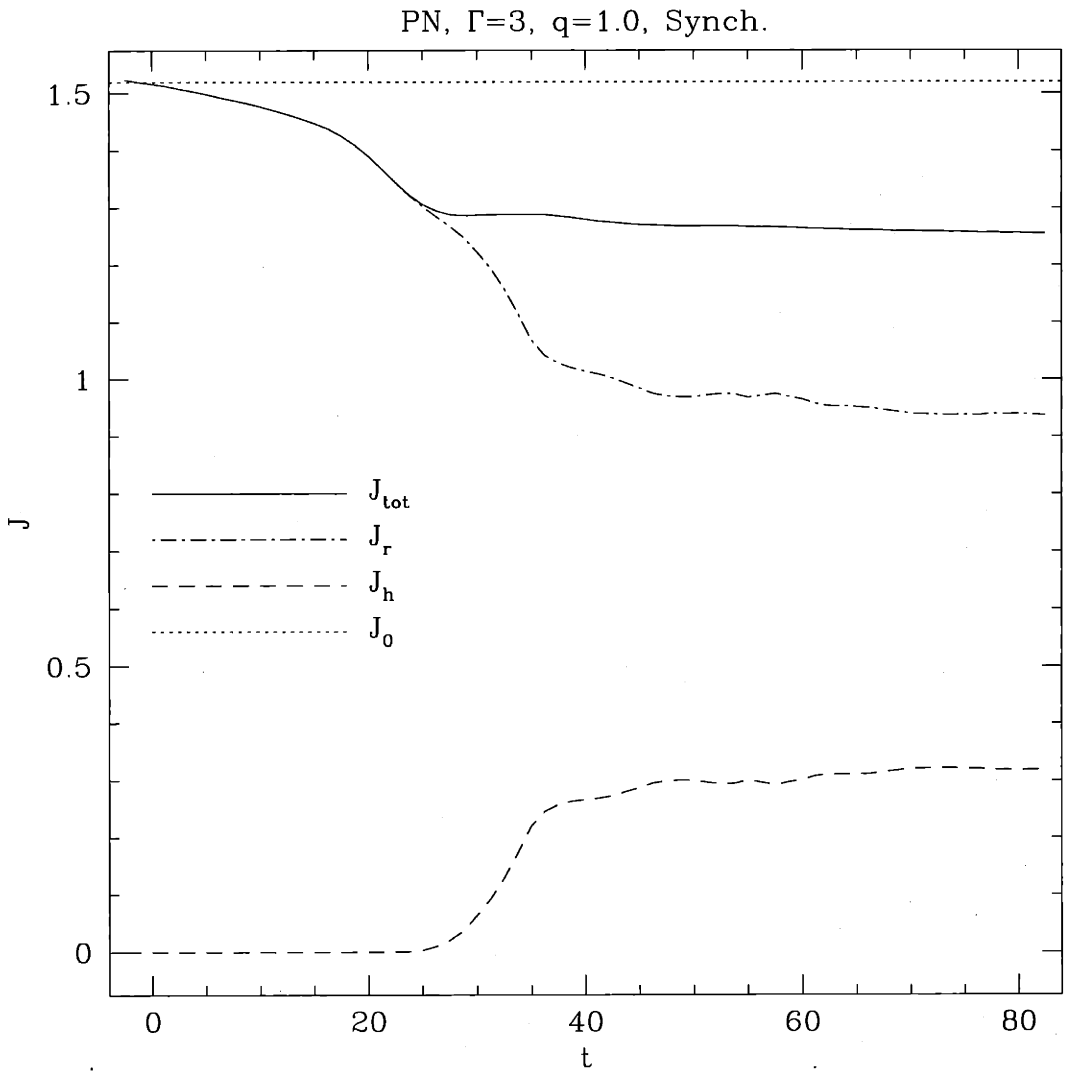

Figure 4-11: Evolution of the angular momentum in various components in the run B1. Conventions are as in Fig. 4-10.

In Fig. 4-12, we show the radial mass and rotational velocity profiles of the remnant. Horizontal cuts through the matter indicate that the rotation is cylindrical, with rotational velocity a function only of the distance from the rotation axis, independent of height relative to the equatorial plane (the same type of rotation profile has been obtained from strictly Newtonian calculations; see RS1). Neither case gives a rigid rotation law. The angular velocity of the Newtonian remnant shows an increase as a function of increasing radius, whereas the PN remnant shows a decreasing angular velocity. Thus, both exhibit signs of differential rotation, but in opposite directions. We find that the centrifugal acceleration and gravitational acceleration become equal at the outer edge of the remnant for both cases, at $r \simeq 1.6\,R$ and $r \simeq 1.85\,R$ for the Newtonian and PN runs, respectively. This is in good agreement with the morphology of the remnants seen in Fig. 4-9, where a noticeable cusp-like deformation is visible in the outermost density contours near the equator in the vertical plane. We conclude that in both runs, the final remnant is maximally and differentially rotating.

The rest mass of the Newtonian remnant at $t = 80$ is $M_r = 1.73\,M$, while that of the PN remnant $M_r = 1.90\,M$. The remaining mass, $0.27\,M$ for the run A1 and $0.10\,M$ for the run B1, has been shed during the coalescence, forming the spiral arms seen in the middle panels of Figs. 4-1 and 4-2. These spiral arms later merge to form a halo of matter around the central remnant. With a crude linear extrapolation from a halo mass of $M_h = 0.27\,M$ for a Newtonian run, with $1/c^2_{1PN} = 0$, and $M_h = 0.10\,M$ for the PN run with $1/c^2_{1PN} = 0.05$, we might expect that, for physically reasonable NS with $1/c^2 \sim 0.15 - 0.20$, the vast majority of the mass will remain in the central remnant. However, this result is crucially dependent on our choice of initial spins and the EOS, and it is limited by the restrictions we have placed on the magnitude of the 1PN corrections. It should also be noted that fully GR calculations of the coalescence of NS with a $\Gamma = 2$ EOS suggest that significant mass loss occurs even for extremely compact NS (Shibata & Uryu 2000).

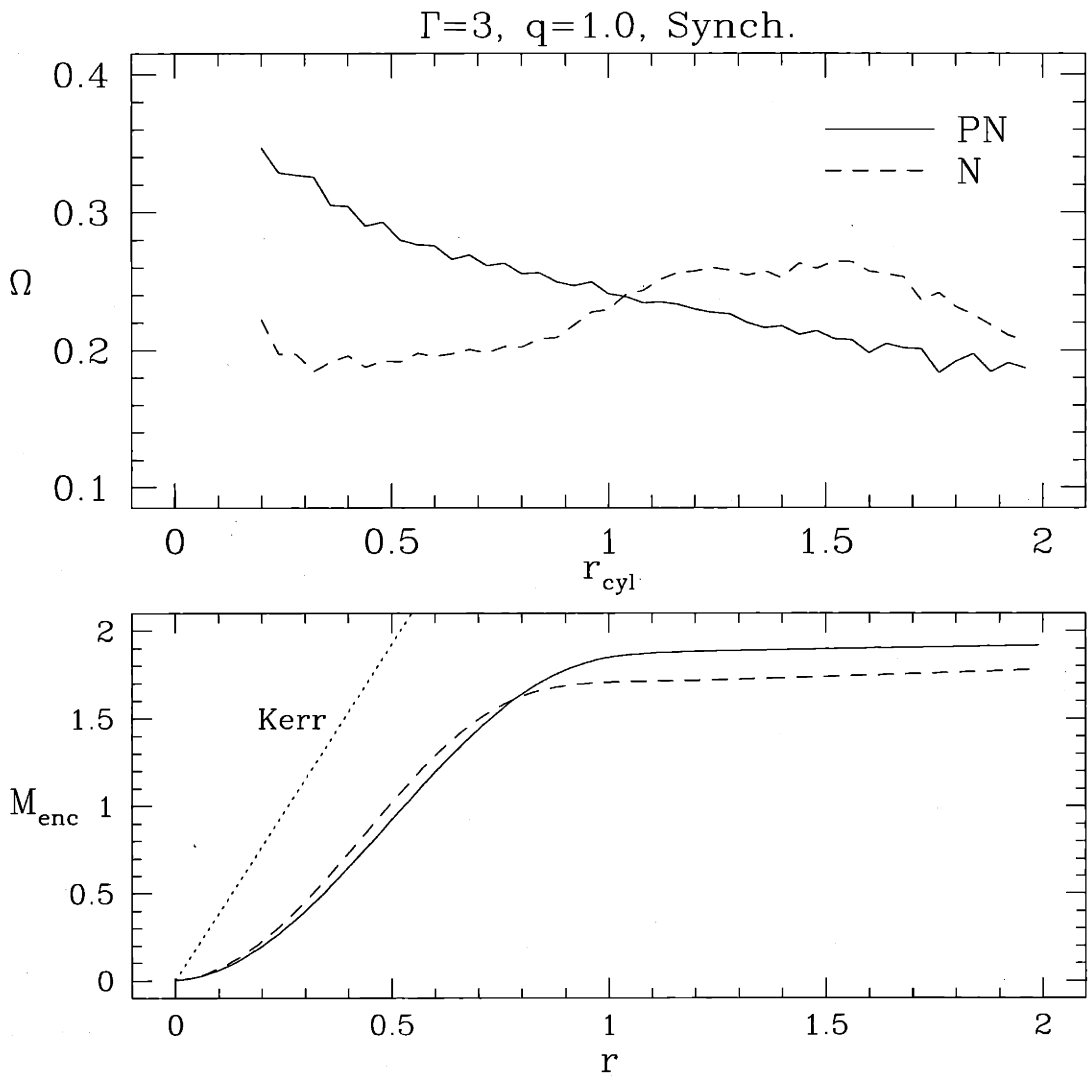

Figure 4-12: Enclosed rest mass and radially averaged rotational velocity profiles of the final merger remnant at t=70 for the two runs. Here, r_{cyl} is the distance from the rotation axis, while r is the radius from center. In both plots, the solid line is for the run B1, the dotted line for the run A1. The dashed line shows the radius for a Kerr black hole with $a = 0.7$ (the value we find for the run B1 at t=70). For the rotational profile, we show only the data for $-0.1 < z < 0.1$, all other horizontal cuts yielding similar profiles extending to smaller radii.

4.4 The final fate of the remnant

By their very nature our calculations cannot address directly the question of whether the NS merger remnant will collapse to form a BH. Indeed the parameters of our PN run were chosen so that all 1PN quantities remain small throughout the evolution, which, for $\Gamma \gg 4/3$, guarantees stability. This can be verified directly by checking, for example, that the mass distribution in the final merger remnant remains everywhere well outside the corresponding horizon radius (see Fig. 4-12). However, given some of the general properties of the merger remnant as determined by our calculations, we can ask whether an object with similar properties, but with a more realistic EOS and higher compactness, would still remain stable to collapse in full GR. For the coalescence of two $1.4\,M_\odot$ NS with realistic stiff EOS, it is by no means certain that the core of the final merged configuration will collapse on a dynamical timescale to form a BH (Rasio 2000; Del Noce, Preti, & de Felice 1998).

The final fate of a NS binary merger in full GR depends not only on the NS EOS and compactness, but also on the rotational state of the merger remnant. It has been suggested, for example, that the Kerr parameter $a_r \equiv J_r/M_{gr}^2$ of the remnant may exceed unity for extremely stiff EOS (Baumgarte et al. 1998). This does not appear to be the case, at least for our choice of EOS. In Fig. 4-13, we show the evolution of the Kerr parameter throughout the entire coalescence, including only particles for which the rest-mass density satisfies $r_* > 0.005$. This cut includes essentially all matter in the initial stages, and effectively cuts out particles in the spiral outflow once the coalescence begins, as well as those remaining in the outer halo at the end. We see that a_r is very near unity just prior to the final merger, but, in contrast to what has been assumed in some previous studies (Del Noce, Preti, & de Felice 1998), it decreases significantly during the final coalescence. The decrease occurs mainly during periods of maximum gravity-wave luminosity, as angular momentum is radiated away, and during the mass-shedding phase after $t \simeq 20$, since angular momentum is transferred from the core to the outside spiral outflow. By the end of run B1, a_r has decreased to $\simeq 0.7$, well below unity, and certainly not large enough

to prevent collapse. The final value of the Kerr parameter for the PN run, $a_r = 0.70$, is considerably greater than that of the Newtonian run, $a_r = 0.34$. The difference is attributable to the greater mass ejected in the Newtonian run, which carries off a significant fraction of the angular momentum of the system (see Figs. 4-10 and 4-11).

Quite apart from considerations of the Kerr parameter, the rapidly rotating core may be dynamically stable. Indeed, most stiff NS EOS (including the recent "AU" and "UU" EOS of Wiringa, Fiks, & Fabrocini 1988) allow stable, maximally rotating NS with baryonic masses exceeding $3\,M_\odot$ (Cook, Shapiro, & Teukolsky 1994), i.e., well above the mass of the final merger core (which is $1.9\,M \simeq 2.85\,M_\odot$ for $M = 1.5\,M_\odot$ in our PN calculation; see Fig. 4-12). Differential rotation (not taken into account in the calculations of Cook, Shapiro, & Teukolsky 1994) can further increase this maximum stable mass very significantly (Del Noce, Preti, & de Felice 1998). For slowly rotating stars, the same EOS give maximum stable baryonic masses in the range $2.5 - 3\,M_\odot$, implying that the core would probably, but not certainly, collapse to a BH in the absence of rotational support.

If the final merger remnant is being stabilized against collapse by rotation, one must then consider ways in which it may subsequently loose angular momentum. Further reduction of the angular momentum of the core by gravitational radiation or dynamical instabilities cannot occur, since, at the end of the dynamical coalescence, the core is, by definition, dynamically stable and nearly axisymmetric (i.e., no longer radiating gravity waves; see Fig. 4-7). The development of a secular bar-mode instability (a quadrupole mode growing unstably on the viscous dissipation timescale; see LRS1 and LRS4) has been discussed as a way of reducing the angular momentum of a rapidly rotating compact object (Lai & Shapiro 1995). However, this cannot occur either for a binary merger remnant because, if the remnant were rotating fast enough to be secularly unstable, it would still be triaxial. For example, that the point of bifurcation of the classical Maclaurin spheroid sequence into the Jacobi ellipsoid sequence coincides with the onset of secular instability for Maclaurin spheroids (Shapiro & Teukolsky 1983; LRS1). Note that other processes, such as electromagnetic radiation or neutrino emission, which may also lead to angular momentum losses, take

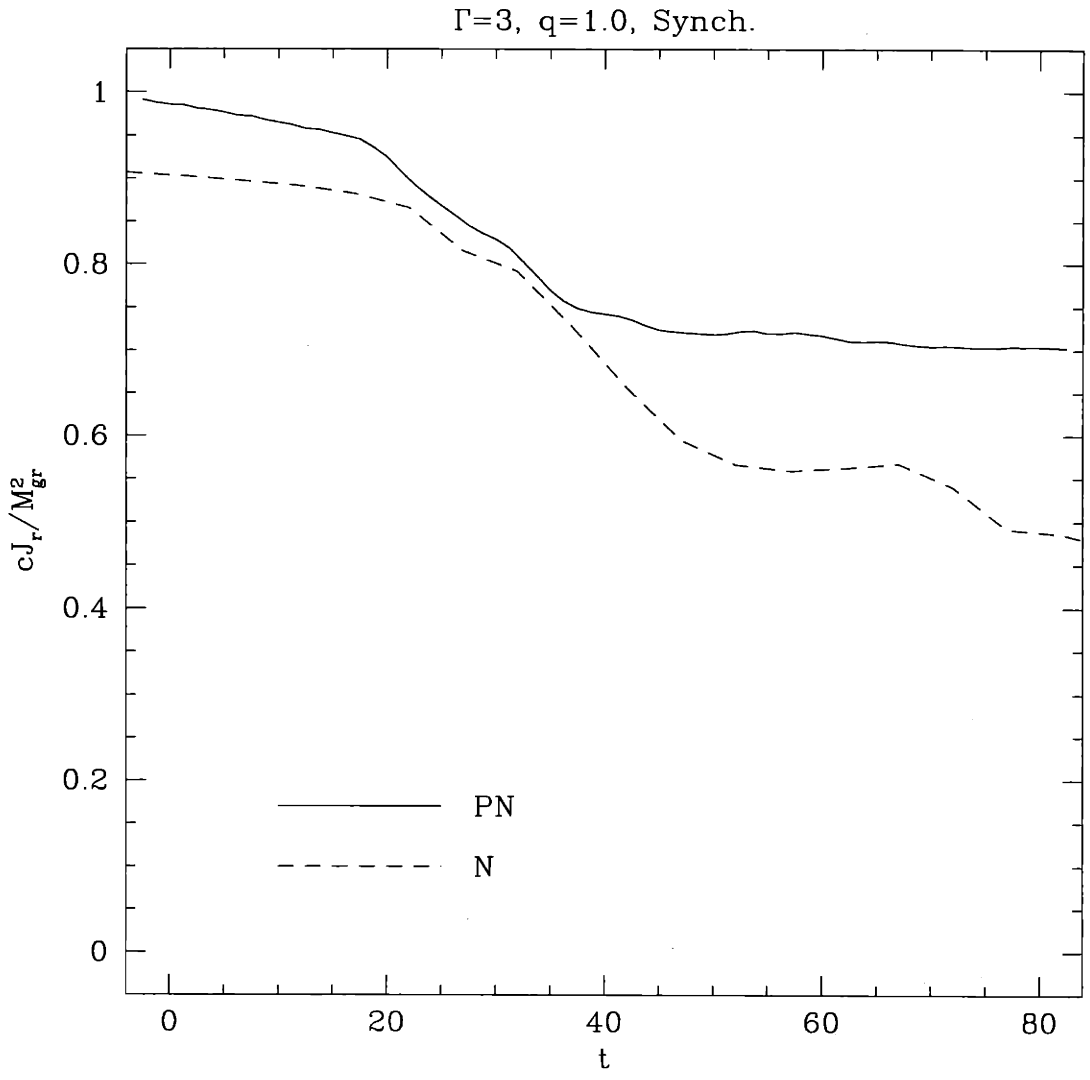

Figure 4-13: The evolution of the Kerr parameter $a_r \equiv cJ_r/M_{gr}^2$, for the inner remnant in run B1 (solid line) and in run A1 (dashed line). At no time do we have $a_r > 1$. The inner remnant (or core) is defined by the same density cut as in Fig. 4-10.

place on timescales much longer than the dynamical timescale, since it can be shown that neutrino emission is probably negligible in these cases (Baumgarte & Shapiro 1998). These processes are therefore decoupled from the hydrodynamics of the coalescence. Unfortunately their study is plagued by many fundamental uncertainties in the microphysics.

Chapter 5

Initially synchronized PN calculations

Note: This chapter is an edited version of an article that was published in Physical Review D (Faber, Rasio, & Manor 2001), and is printed here with the editor's approval. My co-authors were Frederic A. Rasio and Justin B. Manor.

As in the previous chapter, we focus here on initially synchronized binary systems, but expand our study to determine the effect of the choice of EOS and the system mass ratio q on the gravity wave signals. We begin with a brief qualitative discussion of the coalescence process for binaries containing NS described by a softer EOS with $\Gamma = 2$. In Figs. 5-1 and 5-2, we show the evolution of the system in runs C1 and D1. Both of these runs are for two identical NS with a $\Gamma = 2$ EOS, but run D1 includes 1PN effects whereas run C1 does not. These plots can be directly compared to Figs. 4-1 and 4-2, which shows the evolution of runs A1 and B1 (for two identical NS with $\Gamma = 3$). We see that most of the features described in the previous chapter are present in these calculations as well, with the width of the spiral arms and the ellipticity of the remnant as the two primary differences. Both of these effects are well understood. The width of the spiral arms reflect mass shedding occuring over a larger area in the merger with the softer $\Gamma = 2$ EOS, which contains more low-density material in the outer layers of the NS than would a stiffer EOS. It should be noted that when we speak of "mass shedding", we mean that matter is ejected from the

central dense core into an outer halo, but not necessarily to infinity. By the end of our simulations, much of the matter forming the outer halo is still gravitationally bound to the system. The more spherical merger remnant present in the merger with a $\Gamma = 2$ EOS reflects the fact that such an EOS cannot maintain a permanent ellipsoidal configuration stably.

As seen in Fig. 5-2, a significant tidal lag angle θ_{lag} develops in the PN system just prior to final merging. Values of θ_{lag} (calculated as the angle between the binary axis and the principal axis of each component) upon first contact are given in Table 3.3 for all runs. Note that for binaries with mass ratios $q \neq 1$, the secondary develops a larger lag angle than the primary. This effect is much more pronounced with the addition of 1PN corrections.

5.1 Dependence on the NS EOS

As discussed in Sec. 2.3, our PN calculations of NS binary coalescence are most relevant for stiff NS EOS, for which most recent calculations give values of $GM/Rc^2 \simeq 0.1 - 0.2$ (for $M \simeq 1.5\,M_\odot$). Even if the true NS EOS were much softer, making strong GR effects dominant throughout the final binary coalescence, performing hydrodynamic calculations in the PN limit would still remain important, since the PN results provide a crucial benchmark against which future full-GR calculations can be tested.

Gravitational radiation wave forms and luminosities for runs A1, B1, C1, D1 are shown in Figs. 5-3 and 5-4, computed from the formulae found in Eqs. 1.21, 1.22, & 1.25. The two polarizations of gravity waves are calculated for an observer at a distance d along the rotation axis of the system, in the quadrupole approximation. As was found for NS with a $\Gamma = 3$ EOS in the previous chapter, for NS with a $\Gamma = 2$ EOS PN corrections serve to lower the maximum gravity wave luminosity, but the effect is more dramatic for the softer EOS. However, regardless of whether we include 1PN terms, the peak gravity wave luminosity is larger for the softer EOS.

Comparing the Newtonian and PN runs in Fig. 5-4, we see that, besides differences

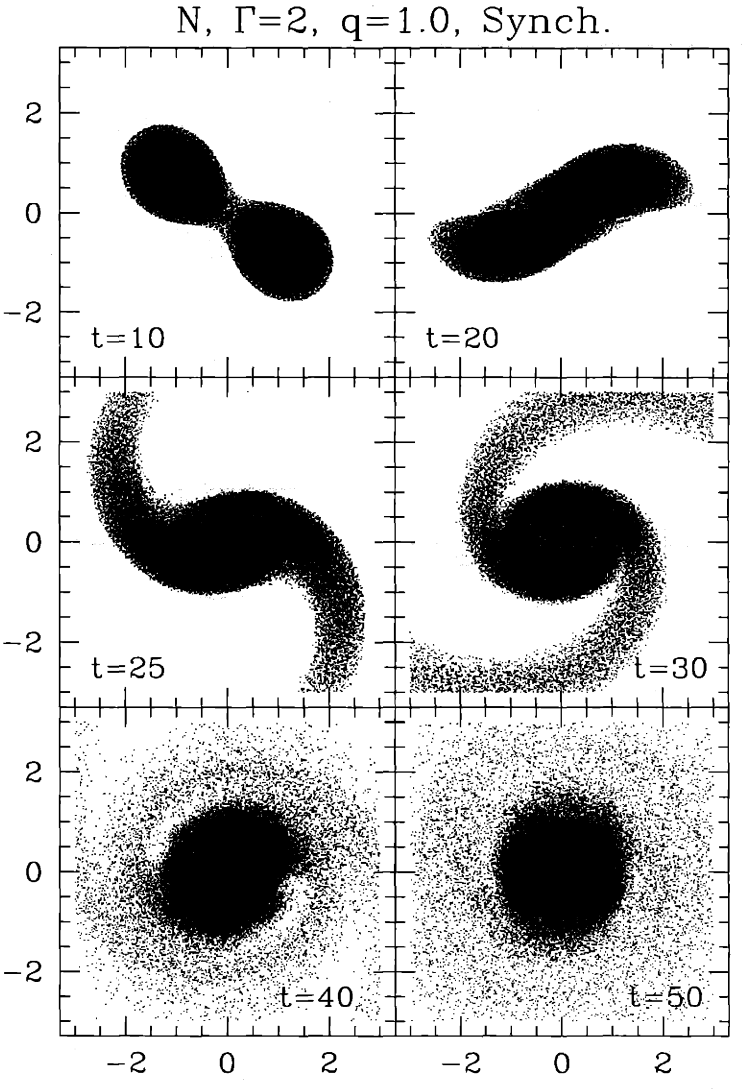

Figure 5-1: Evolution of the system for Run C1 with $\Gamma = 2$ and $q = 1$. This run includes all radiation reaction but no 1PN effects. Conventions are as in Fig. 4-1.

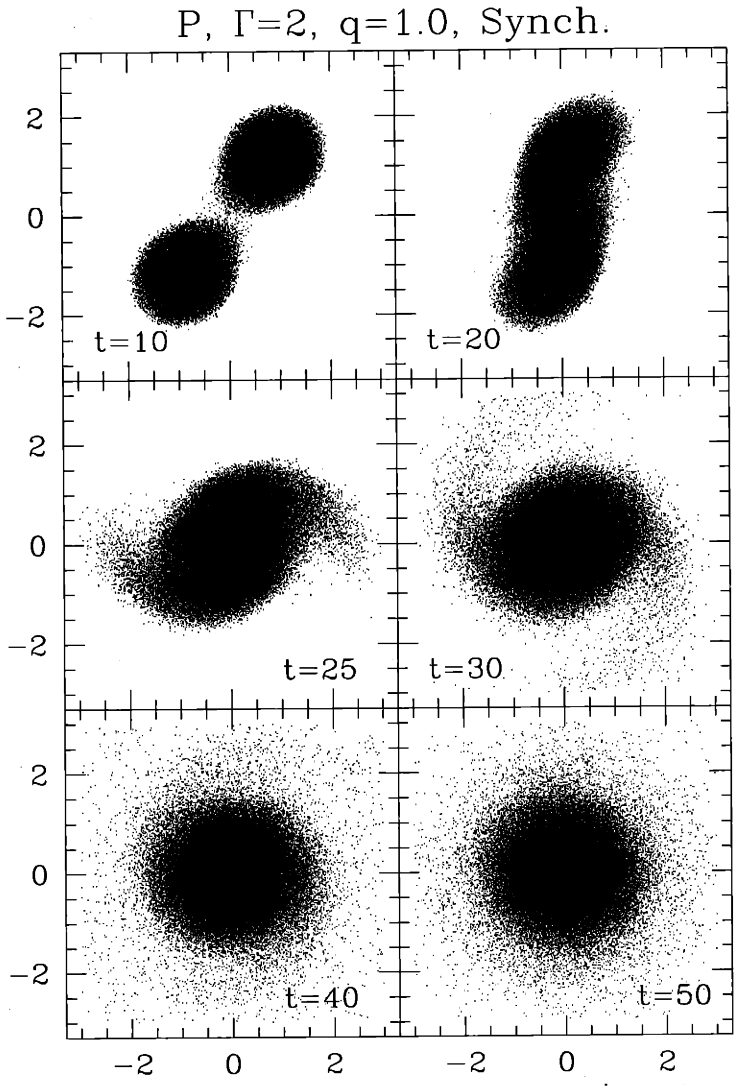

Figure 5-2: Evolution of the system for Run D1 with $\Gamma = 2$ and $q = 1$. This run includes all 1PN and radiation reaction (2.5PN) corrections. Conventions are as in Fig. 4-1.

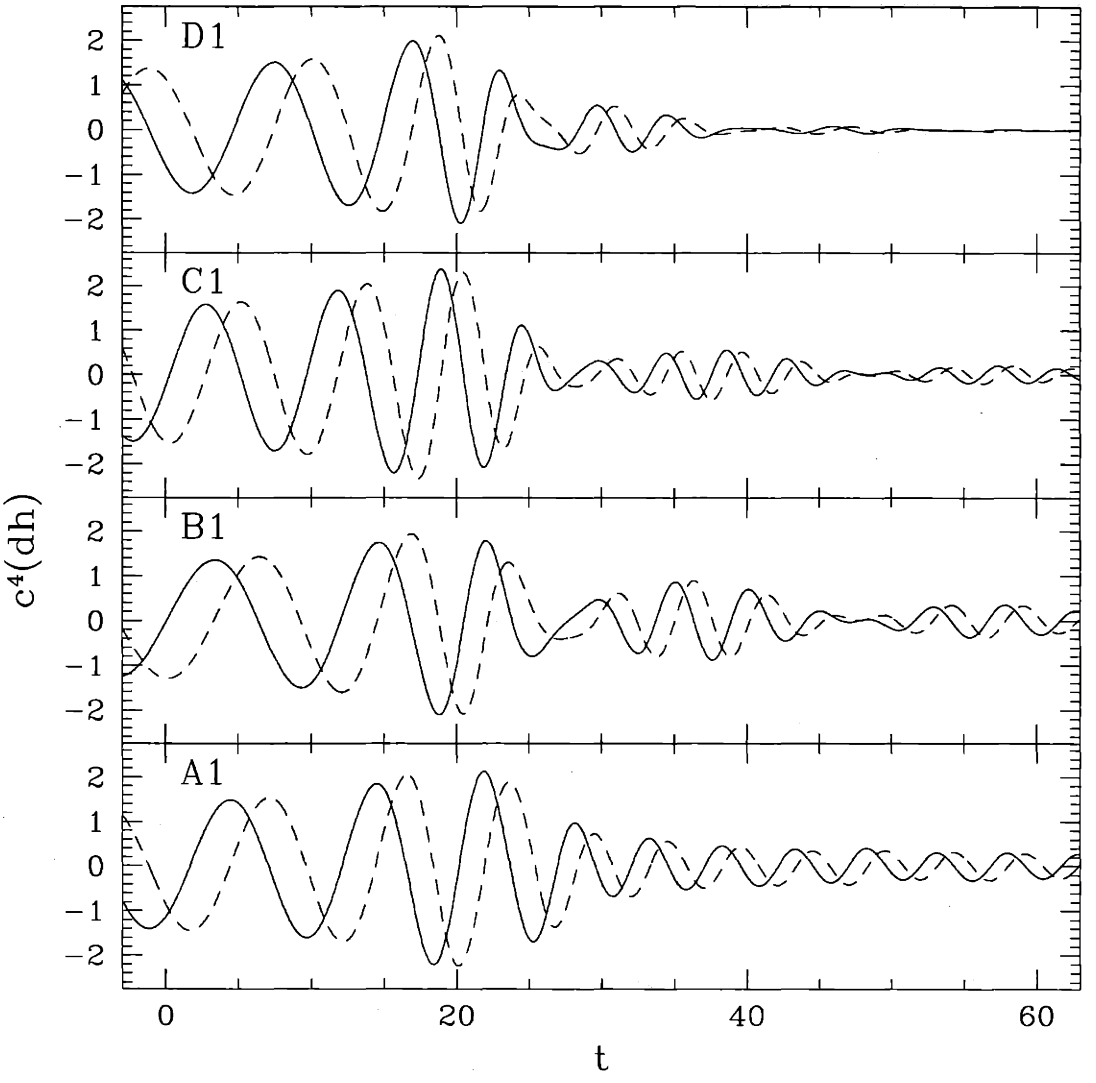

Figure 5-3: Gravity wave signatures for the runs A1 (N, $\Gamma = 3$), B1 (PN, $\Gamma = 3$), C1 (N, $\Gamma = 2$), and D1 (PN, $\Gamma = 2$). All have $q = 1$. The solid line shows the h_+ polarization, the dashed line the $h_\times$ polarization, both calculated for an observer at a distance d along the rotation axis. Note that at $t > 60$, there is essentially no gravitational radiation given off by $\Gamma = 2$ EOS binaries.

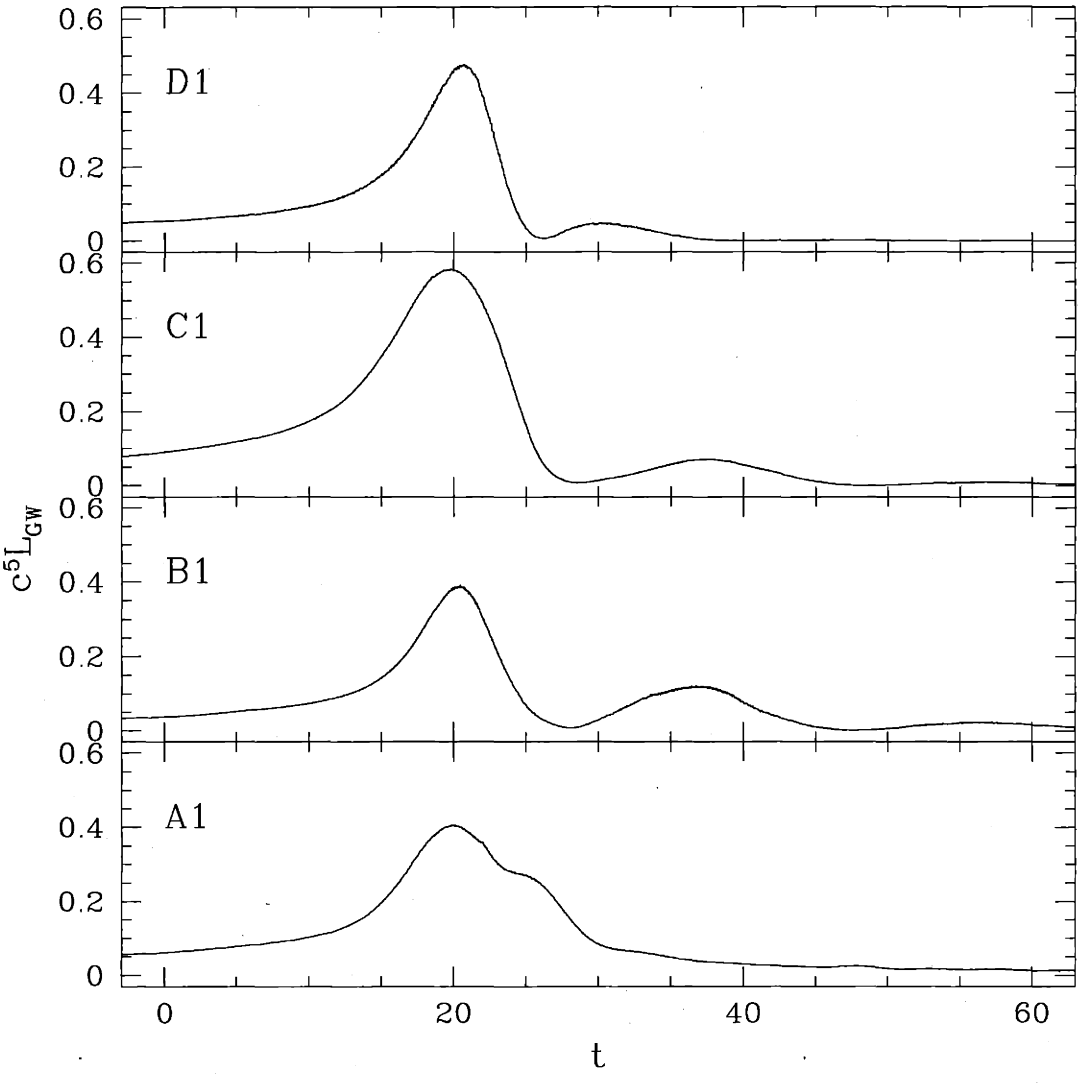

Figure 5-4: Gravity wave luminosity for the same runs as in Fig. 5-3. We see clear evidence for a second gravity wave luminosity peak in both $\Gamma = 2$ runs, but only in the PN $\Gamma = 3$ run.

in the maximum luminosity, there are qualitative differences in the shape of the first luminosity peak. Both PN runs show narrower luminosity peaks than their Newtonian counterparts. This effect can be attributed to the faster binary infall as the two stellar cores first come into contact (as seen in Fig. 5-5, which shows the binary separation r as a function of time).

Slightly different behavior is seen in the Newtonian runs. For the run with a $\Gamma = 3$ EOS (A1), we see a decrease in the inspiral rate from $t = 20 - 25$, which occurs after the period of maximum gravity wave luminosity, and a simultaneous plateau in the luminosity immediately after the peak. This corresponds with the onset of mass shedding, as particles begin to be ejected through the outer Lagrange points of the system. For the $\Gamma = 2$ case (C1), we see no apparent decrease in the inspiral rate, either before or after $t = 20$. Correspondingly, this was run showed an almost completely symmetric luminosity peak with respect to time.

In Fig. 5-6, we show the energy loss to gravitational radiation, calculated as the integral of gravity wave luminosity over time. We see that the Newtonian runs, A1 and C1, have higher energy losses than their PN counterparts B1 and D1, respectively, and that the runs with the softer $\Gamma = 2$ EOS, C1 and D1, have higher energy losses than their stiffer counterparts A1 and B1. The effects of EOS and gravity formalism here are seen to be of equal magnitude, although when we extrapolate toward fully relativistic physics, we expect the decrease in gravitational energy between Newtonian calculations and relativistic ones to be more pronounced. Note that energy losses are measured from the initial point of each run. Thus, since the runs had negative time offsets, $E_{GW} > 0$ at $t = 0$.

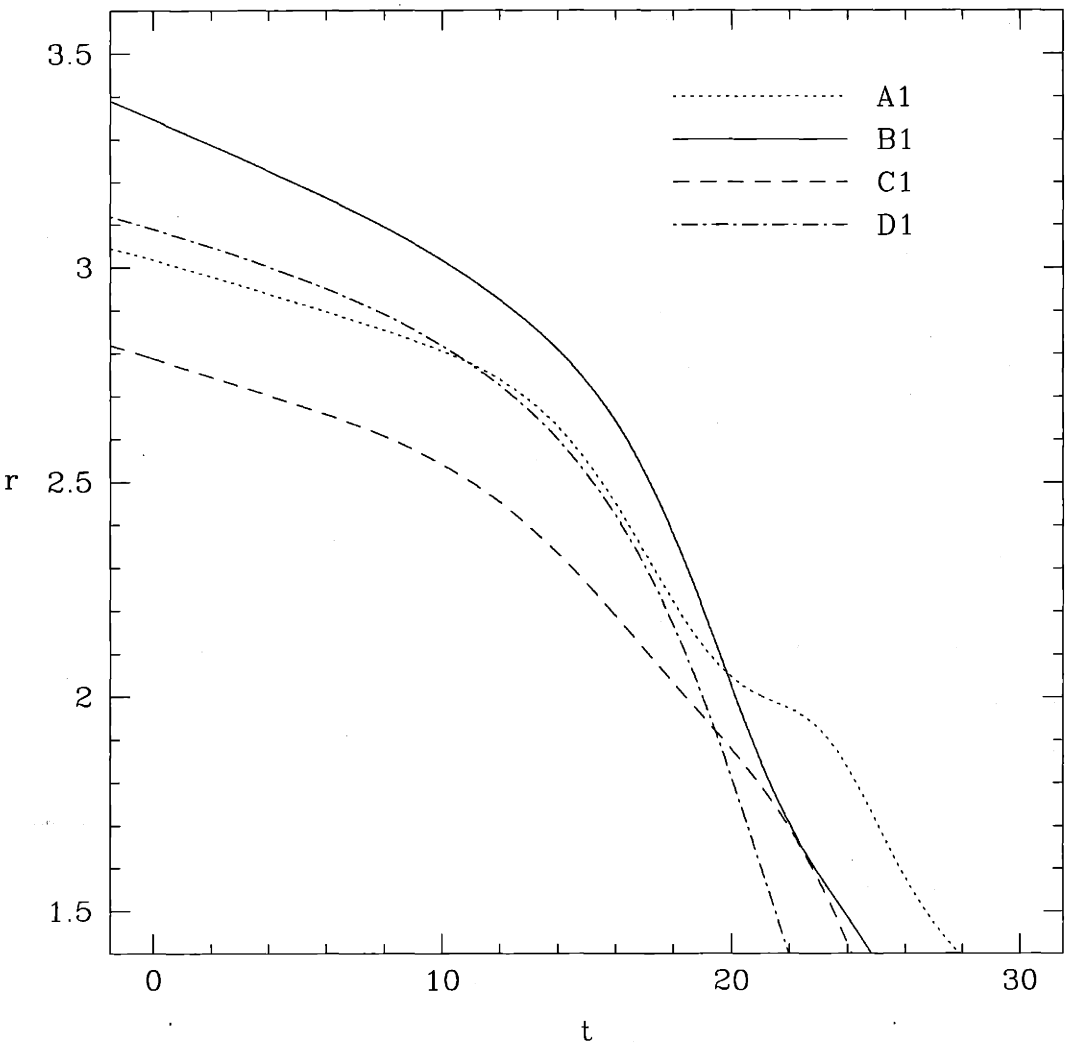

Figure 5-5: Binary separation r for the same runs as in Fig. 5-3.

More surprisingly, perhaps, we note that a second luminosity peak is visible not only in the $\Gamma = 2$ PN run (D1), but also in run C1, for a $\Gamma = 2$ Newtonian coalescence. In the previous chapter, it was shown that the gravity wave luminosity is extremely well correlated with the ratio of the first and second principal moments of inertia, I_1 and I_2, in effect giving a measure of the ellipticity of the remnant in the orbital plane. A similar analysis is shown in Fig. 5-7, which compares runs C1 and D1. Note that we have used a higher density cut for this plot than was used for the $\Gamma = 3$ remnants in the previous chapter. Here only, we define the inner remnant to consist of all SPH particles with local densities $r_* > 0.04$. We see again a strong correlation between ellipticity and gravity wave luminosity. In run D1, the small-amplitude oscillations with period $T \simeq 5$ are caused by an interaction with the outer material of the remnant. If we lower our density cut to include all SPH particles with local densities $r_* > 0.005$ (as in the previous chapter), thereby including more of the tenuous material outside of the core of the remnant, the moment of inertia ratio shows only this oscillation, which damps out over time. Since this material contributes only weakly to the quadrupole moment, we conclude that it is the dynamics inside the core that controls the gravity wave signal.

Comparing the results of our run C1, which includes the effects of radiation reaction, with the completely Newtonian $\Gamma = 2$ run shown in RS2, we conclude that the asymmetry induced by the larger tidal lag angle is responsible for the existence of a second gravity wave luminosity peak, even for systems that eventually reach oblate, non-radiating configurations. To confirm this, we checked our results against a completely Newtonian $\Gamma = 2$ test run (without radiation reaction terms, and starting from $r_0 = 2.7$), and found that a second peak is indeed absent in this case (in agreement with RS2).

Careful inspection of Fig. 4-7 reveals very small irregularities in the otherwise smooth gravity wave luminosity at $t \simeq 33$ and 48, which correspond to the secondary gravity wave luminosity peaks found in run B1. Clearly, the existence of secondary luminosity peaks seems to be reasonably universal in these simulations. For run A1, however, modulation of the moment of inertia ratio is virtually absent, so that the

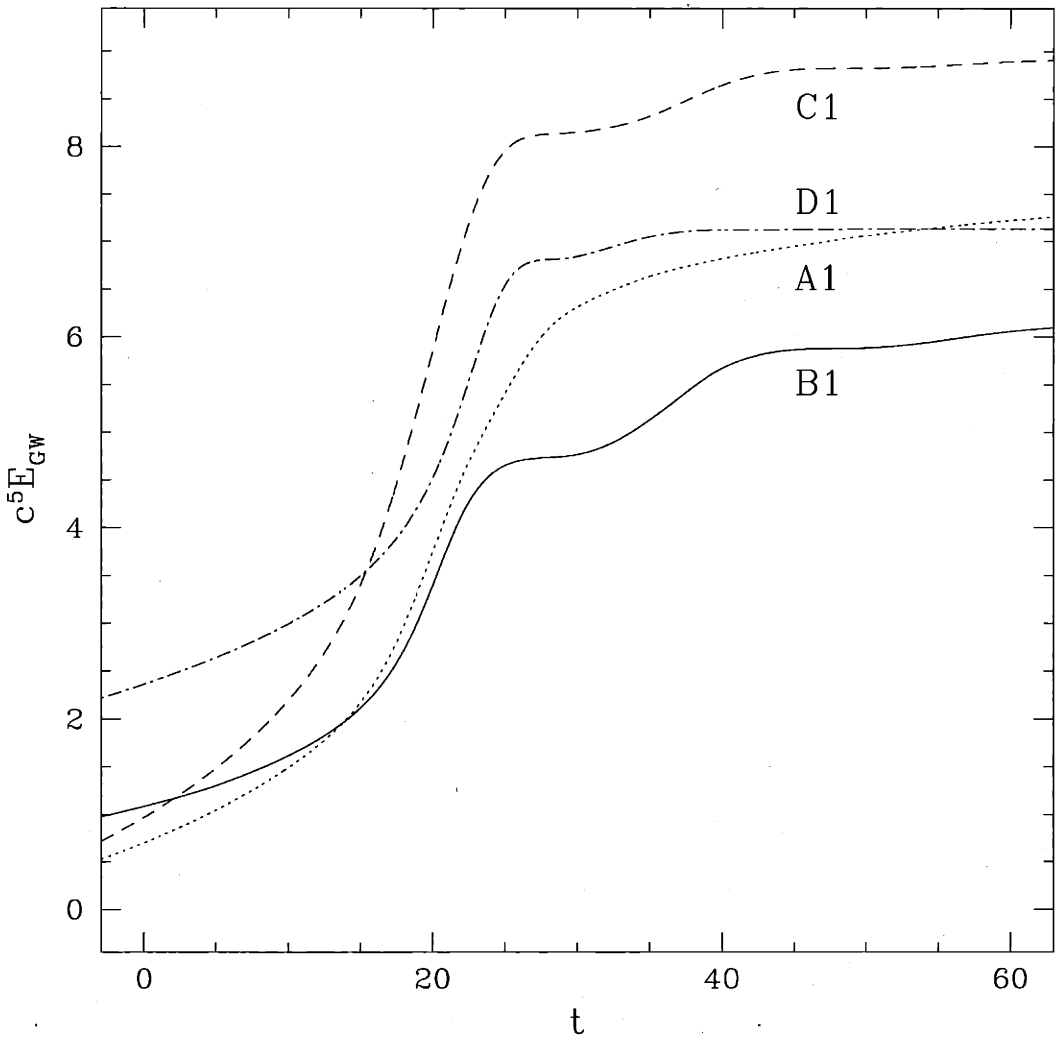

Figure 5-6: Energy lost to gravitational radiation for the same runs shown in Figs. 5-3, 5-4, & 5-5.

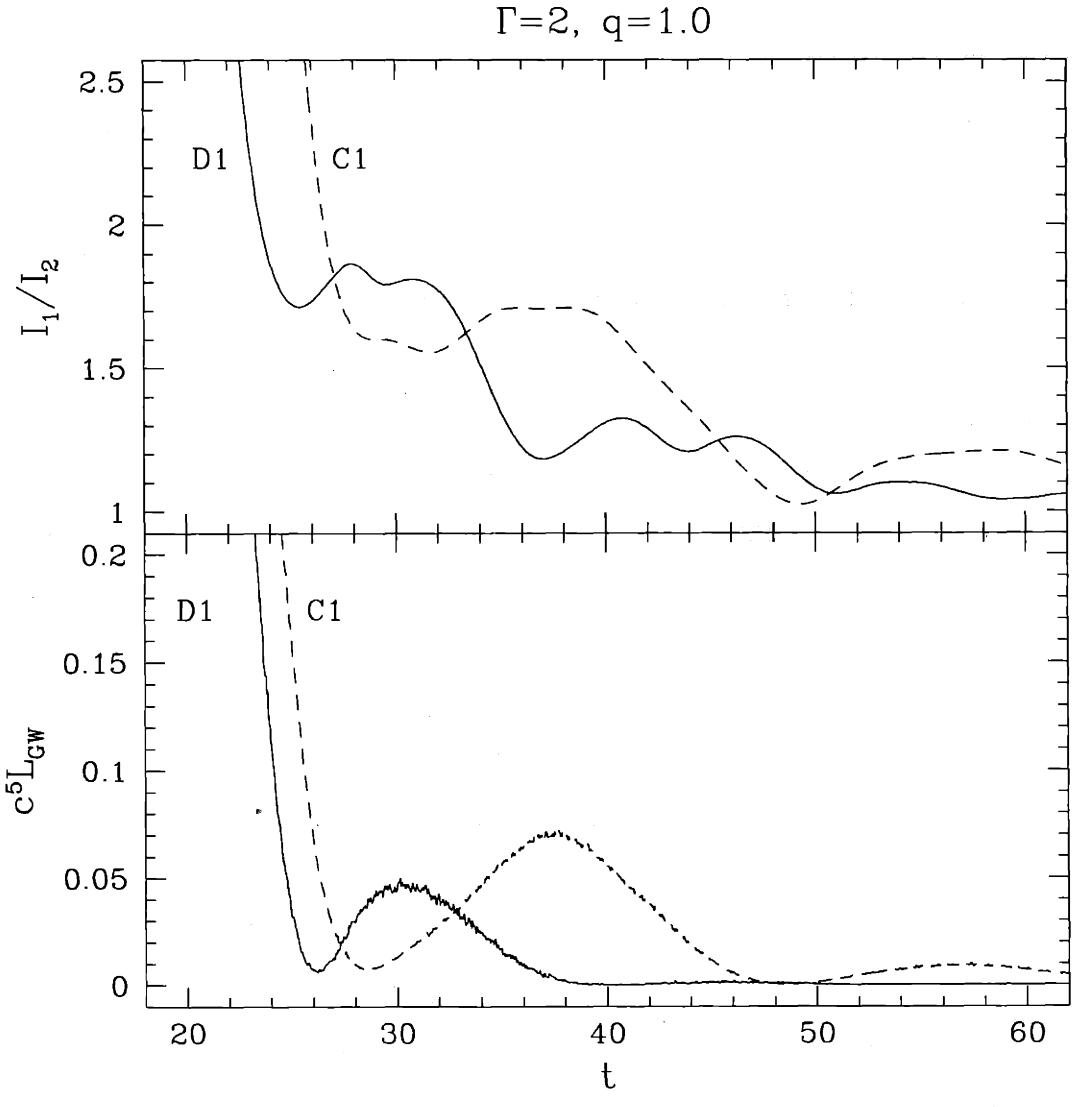

Figure 5-7: Ratio of the principal moments of inertia in the equatorial plane for the remnants of runs C1 (N, $\Gamma = 2$; dashed lines) and D1 (PN, $\Gamma = 2$; solid lines), compared to the corresponding gravity wave luminosities at late times. We see a clear correlation between the two quantities, as the remnants relax towards an axisymmetric, oblate configuration. Here the remnants are defined by the density cut $r_* > 0.04$, which includes the entire binary initially, but only the inner part of the merger at later times.

effect is extremely small in this case.

5.2 Dependence on the binary mass ratio

The dependence of the peak gravity wave amplitude amplitude, defined by Eq. 3.75, on the mass ratio q appears to be very strong. In RS2, an approximate power law $h_{max} \propto q^2$ was derived for nearly equal-mass systems, on the basis of two purely Newtonian calculations for $q = 1$ and $q = 0.85$. This is considerably steeper than the naïve scaling obtained for two point masses in a Keplerian orbit, which gives $h_{max} \propto q$. Such a linear scaling is obeyed (only approximately, because of finite-size effects) by the wave amplitudes of the various systems prior to final coalescence. For determining the maximum amplitude during the merger, however, hydrodynamics must be taken into account. In a system with $q \neq 1$, the more massive star tends to play a far less active role in the hydrodynamics and, as a result, there is a rapid suppression of the radiation efficiency as q departs even slightly from unity. For the peak luminosity of gravitational radiation RS found approximately $L_{max} \propto q^6$. Again, this is a much steeper dependence than one would expect based on a simple point-mass estimate, which gives $L \propto q^2(1+q)$. The results of RS were all for initially synchronized binaries, but very similar results have been obtained by Zhuge, Centrella, & McMillan (1996) for binaries containing initially nonspinning stars with unequal masses.

The role of the primary and secondary is shown qualitatively in Figs. 5-8 and 5-9 for run D2, which uses a $\Gamma = 2$ EOS with $q = 0.8$, and included 1PN terms. The panels on the left show the primary, center panels the secondary, and those on the right the combined system. We see that the evolution is markedly different from that of the $q = 1$ binary shown in Fig. 5-2. Here, there is a single spiral arm, which is formed from the secondary as it gets tidally disrupted. Shortly after first contact is made, a stream of matter flows from the secondary toward the primary, landing on the trailing side (orbital rotation is counterclockwise), as a result of the orbital motion and the significant tidal lags present in the system upon contact. As the coalescence proceeds, the secondary is tidally stretched, with the outer portion spun out of the

system while the inner part is accreted by the primary. Throughout this evolution, the primary remains relatively undisturbed, except for a small layer near its surface. By $t \simeq 40$, mass shedding is triggered and the system develops a single spiral arm, composed entirely of matter from the secondary as it is completely disrupted. Note that this single spiral arm is even wider than those seen in the $q = 1$ coalescence (with a width comparable to the initial NS radius). There is also an extremely small amount of mass shedding from the outer edge of the primary, where it joins with a high-velocity stream of matter from the secondary, on the side opposite the single spiral arm. Finally, by $t \simeq 50$, what was once the core of the secondary has fallen onto the primary, and the spiral arm has begun to dissipate, forming a low-mass halo around the system.

In Figs. 5-10 and 5-11, we show the gravitational radiation wave forms and luminosity for all but two of the synchronized binary simulations. For clarity, we only show results for runs A1, A3, and A5 in the $\Gamma = 3$ Newtonian plot, since the other runs can be safely interpolated from those present. We note that for the $\Gamma = 3$ EOS, the morphology of the peaks seen in Fig. 5-4 seems to be present for all mass ratios. We find narrower gravity wave luminosity peak for PN runs, and broader peaks for Newtonian runs.

In Fig. 5-12 we show the maximum gravity wave amplitude, defined by Eq. 3.75, and the maximum gravity wave luminosity for $\Gamma = 3$ and $\Gamma = 2$ EOS binaries, plotted as a function of the mass ratio. We find in all cases that the power-law dependence is steeper than would be predicted by the point-mass approximation. For the gravity wave strain, we see a slightly steeper power law for Newtonian runs than for PN runs. For $q = 1$, Newtonian runs have a higher peak strain, but, for both EOS, the $q = 0.8$ binaries show a higher peak strain in the PN case than in the Newtonian case. We conclude that the strictly Newtonian scaling obtained by RS2, $h_{max} \propto q^2$, remains approximately valid for Newtonian binaries with radiation reaction effects, but is almost certainly steeper than the dependence that will be present in realistic NS binaries (based on our results including 1PN effects).

For the peak gravity wave luminosity, we see a much stronger dependence on

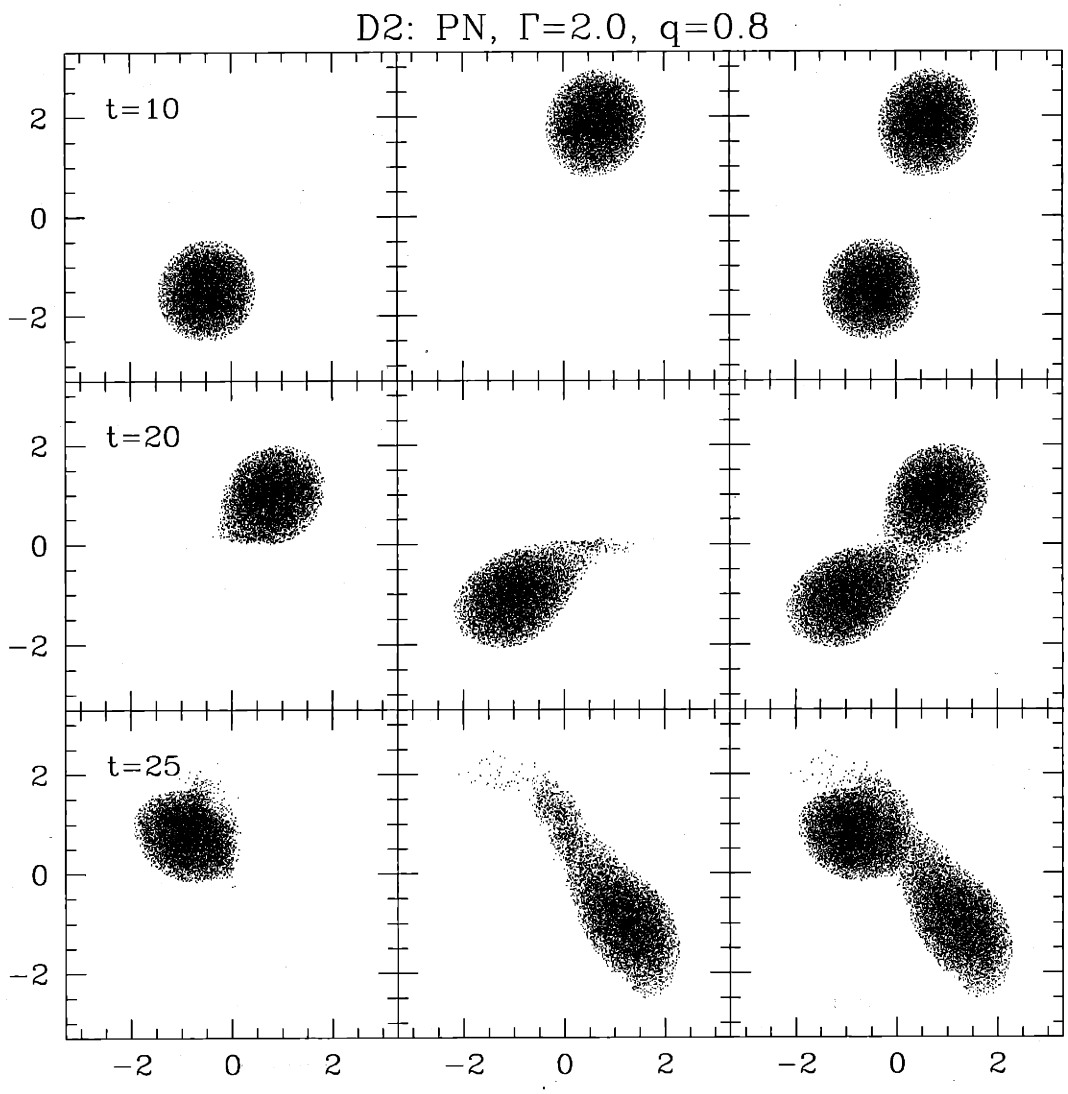

Figure 5-8: Evolution of the system for run D2 with $\Gamma = 2$, $q = 0.8$, and 1PN corrections included. Panels on the left show the primary, center panels show the secondary, and panels on the right the entire system.

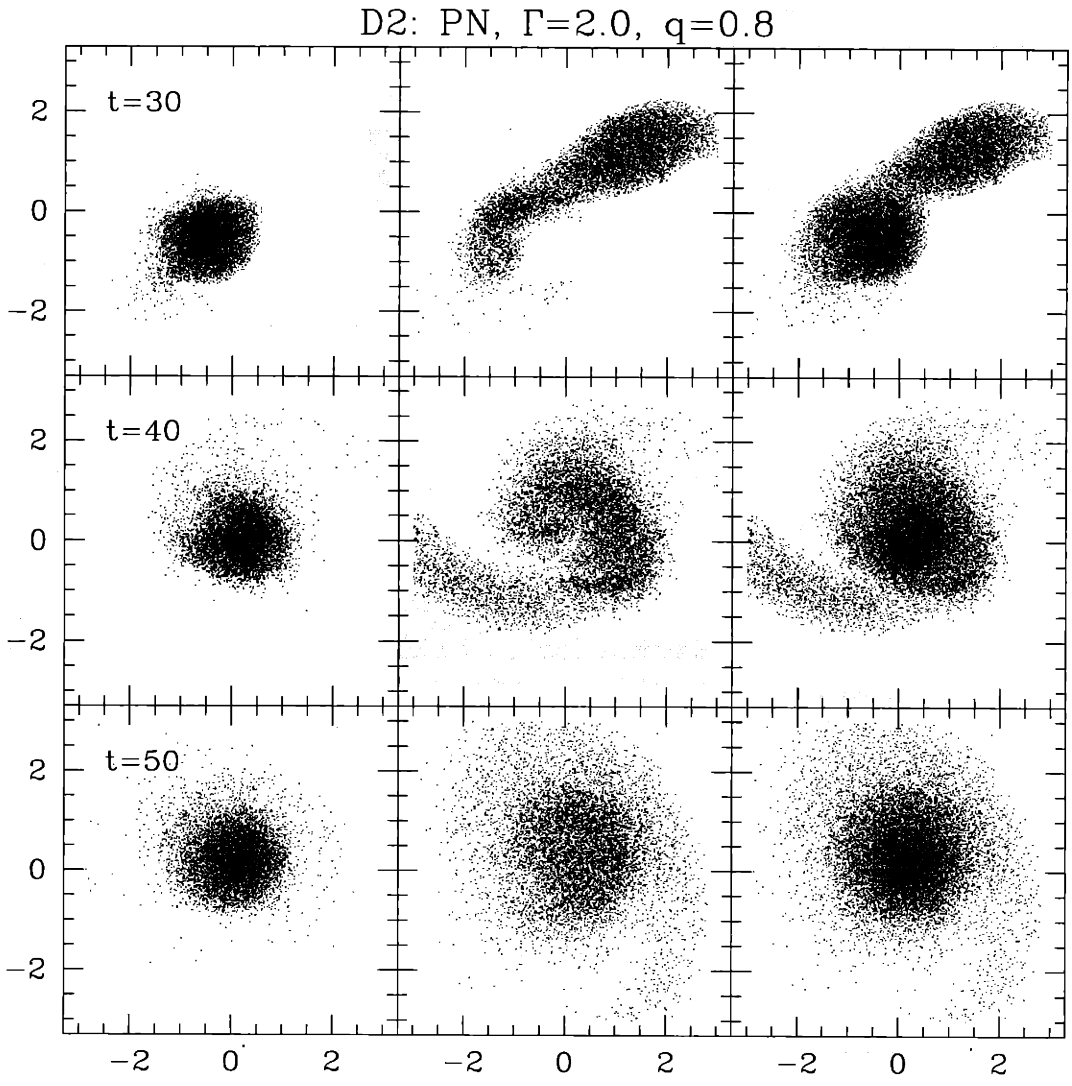

Figure 5-9: Evolution of run D2, continued.

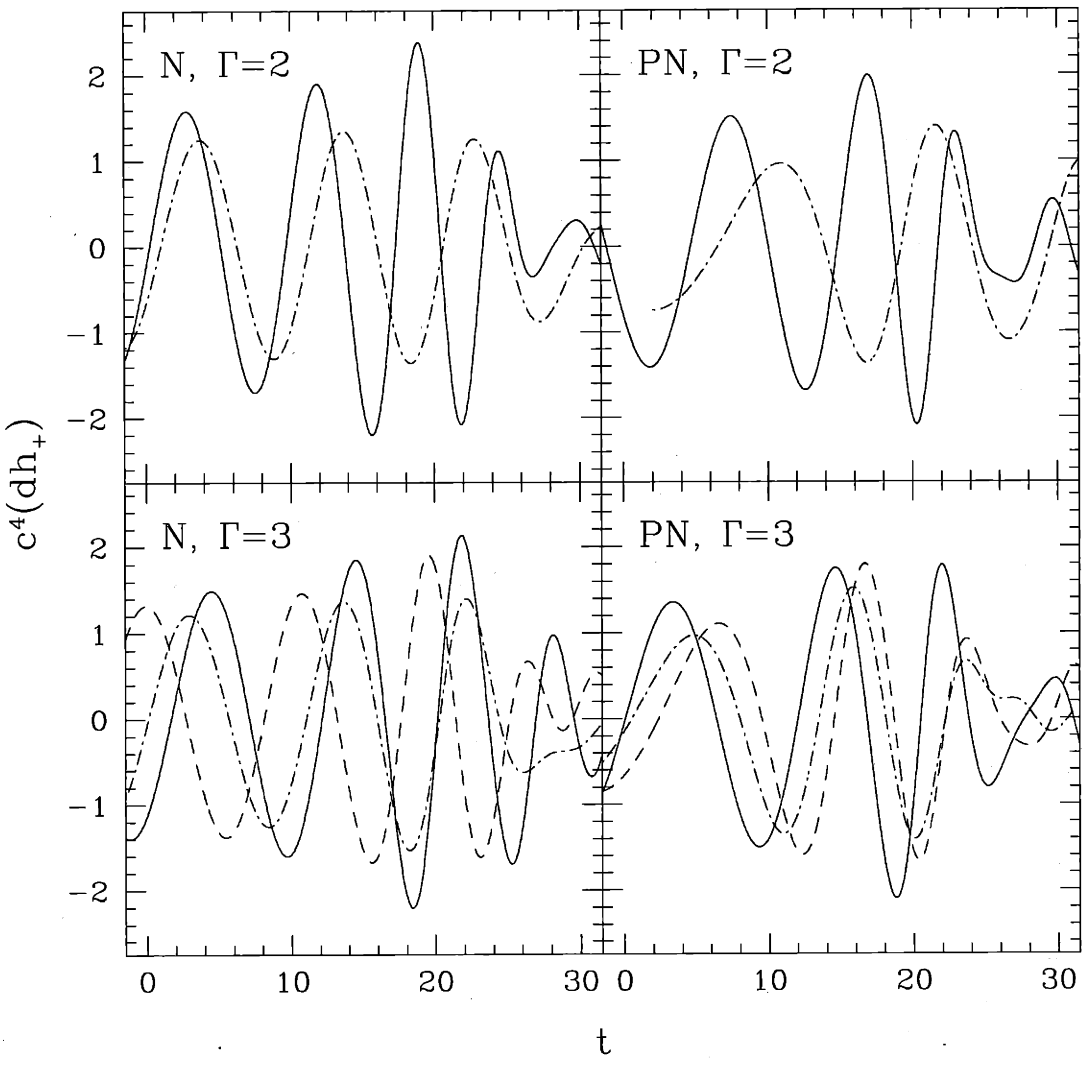

Figure 5-10: Gravity wave amplitude h_+ for an observer located at a distance d along the rotation axis, comparing systems with different mass ratios. The solid lines correspond to $q = 1$, the dashed lines to $q = 0.9$, and the dot-dashed lines to $q = 0.8$.

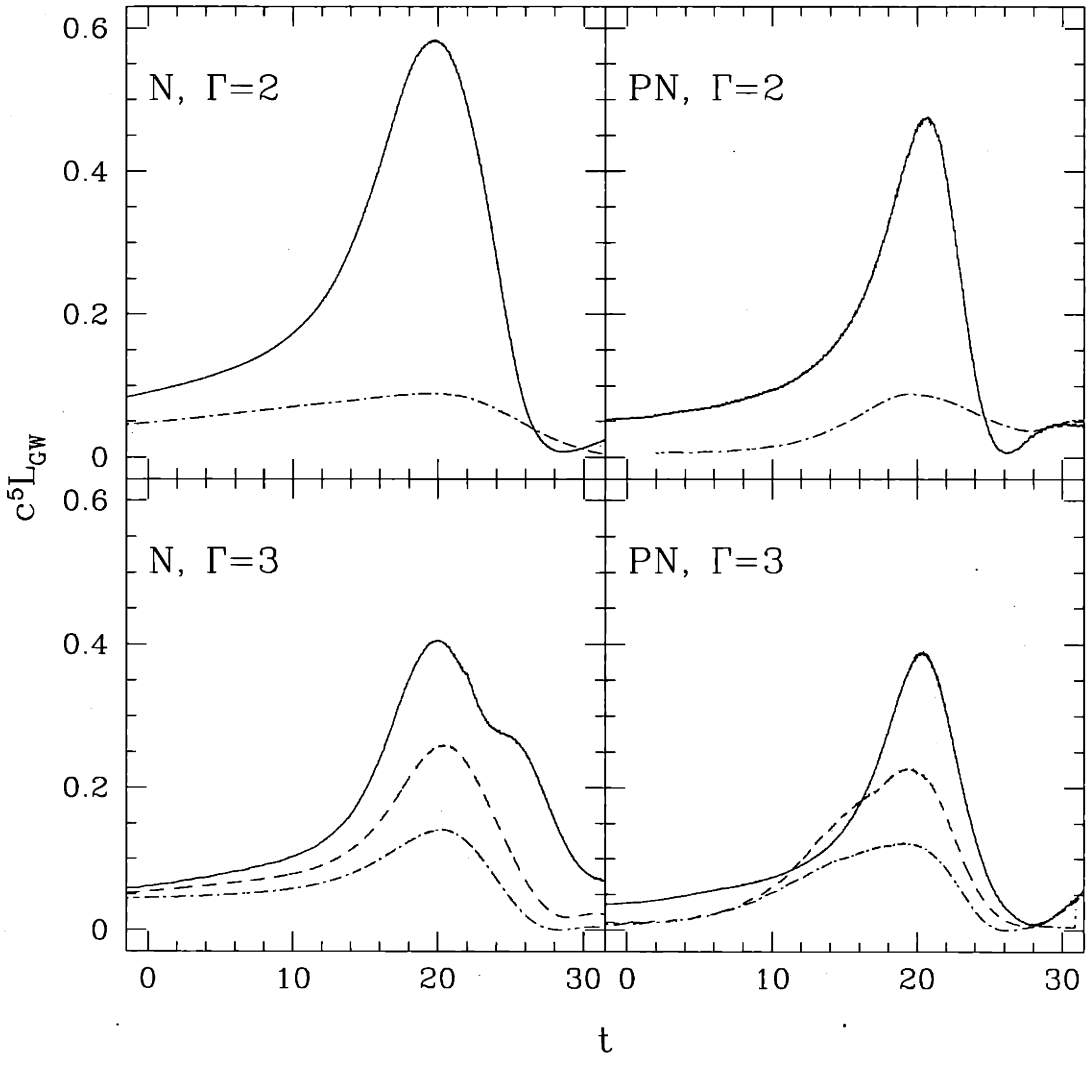

Figure 5-11: Gravity wave luminosity for the same runs shown in Fig. 5-10. Conventions are in Fig. 5-10.

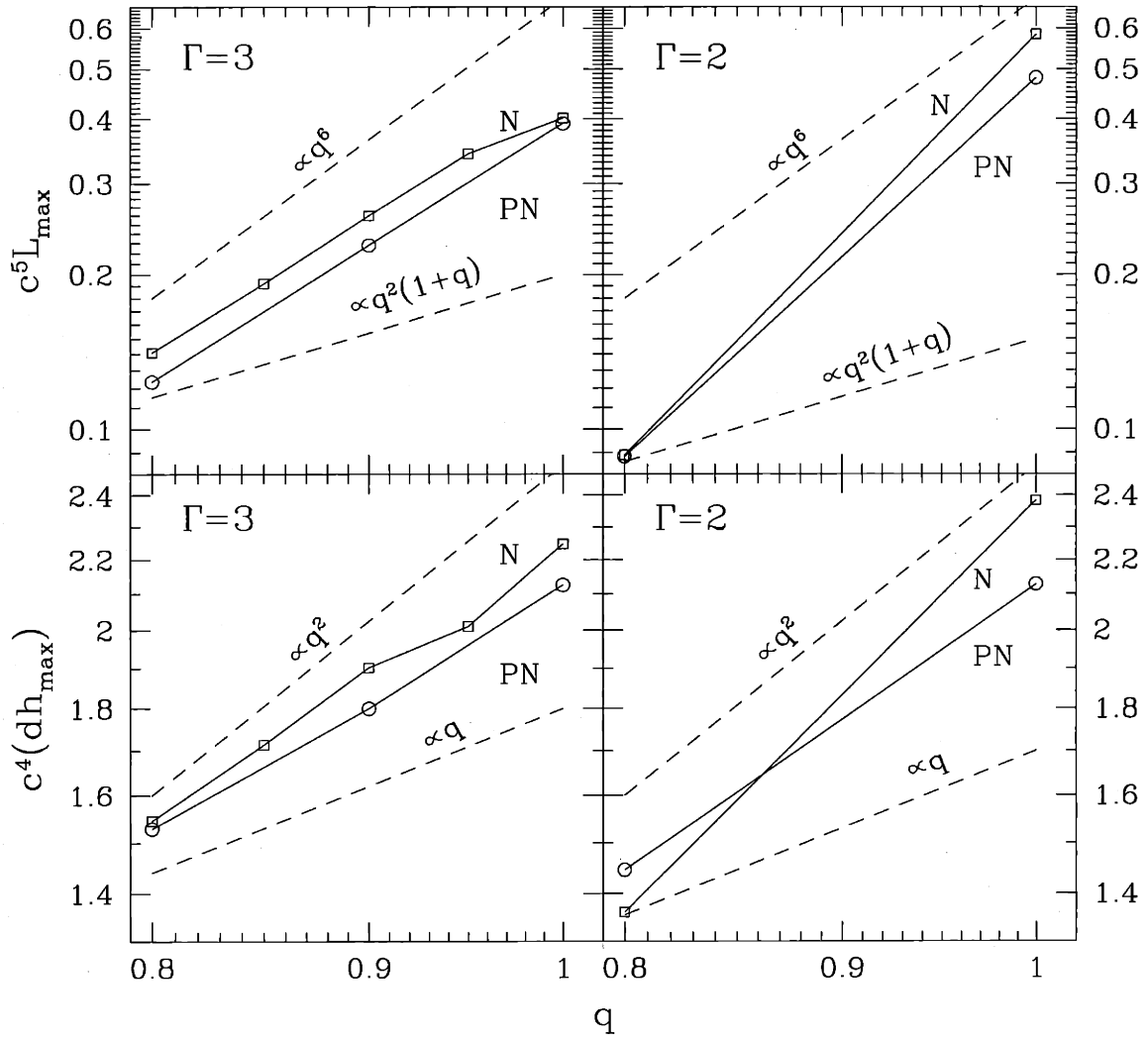

Figure 5-12: Dependence of the maximum gravity wave amplitude and luminosity on the mass ratio (for all the synchronized binaries). The Keplerian point mass approximation gives $h_{max} \propto q$ and $L_{max} \propto q^2(1+q)$. Instead, the strictly Newtonian hydrodynamic calculations of RS2 give approximate power laws $h_{max} \propto q^2$ and $L_{max} \propto q^6$ for nearly equal-mass binaries containing $\Gamma = 3$ polytropes. Note that both axes are plotted logarithmically.

the EOS. For the softer, $\Gamma = 2$ EOS, we see that the strictly Newtonian RS2 fit of $L_{max} \propto q^6$, obtained for $\Gamma = 3$ polytropes, is not nearly as steep as the correct relation. For $\Gamma = 3$, we see that the RS2 fit is slightly too steep, although the correct power law remains steeper than the point-mass approximation.

5.3 Structure of the final merger remnant

It was found in Sec. 4.3 that the addition of 1PN corrections to the hydrodynamics has the effect of reducing mass shedding for mergers of NS with a $\Gamma = 3$ EOS. In Fig. 5-13, we show the evolution of the remnant mass M_r for runs C1 and D1, and find the same behavior for a $\Gamma = 2$ EOS. We show two different density cuts to highlight this behavior. By taking all SPH particles with a local density $r_* > 0.005$, we extend our definition of the "remnant" far into the outer halo. Instead, a density cut of $r_* > 0.04$ includes just the inner part of the remnant, and excludes any material that was ejected into spiral arms. In both runs mass shedding starts occuring approximately at the time of maximum gravity wave emission ($t = 20$), and lasts for a total time $\delta t \simeq 10$, but in the PN case the mass shedding rate is significantly smaller, leading to approximately half the total amount of mass shedding as in the Newtonian case.

In Fig. 5-14, we show the radial mass profiles of the inner remnants for the four synchronized $q = 1$ runs. We see that the mass profile at small radii for the initially synchronized runs is primarily determined by the EOS, with the $\Gamma = 2$ models showing slightly more central concentration, as would be expected, although the inclusion of 1PN effects does decrease the enclosed mass in a given cylinder. At $r \simeq 1.2$, however, we start to see significant differences between runs with and without 1PN corrections. In the Newtonian runs, matter is ejected much more efficiently to large radii, and thus the final mass of the inner remnant falls in the range $M_r = 1.7 - 1.8$, whereas for the PN runs it is $M_r \simeq 1.9$. The remaining mass, ejected through the spiral arms, forms the halo around the inner remnant. Here we can see from the slopes of the mass profiles near $r_{\rm cyl} \simeq 2$ that for a softer ($\Gamma = 2$) EOS, the density in the halo near the inner remnant is still significant, indicating more mass in the inner region of the

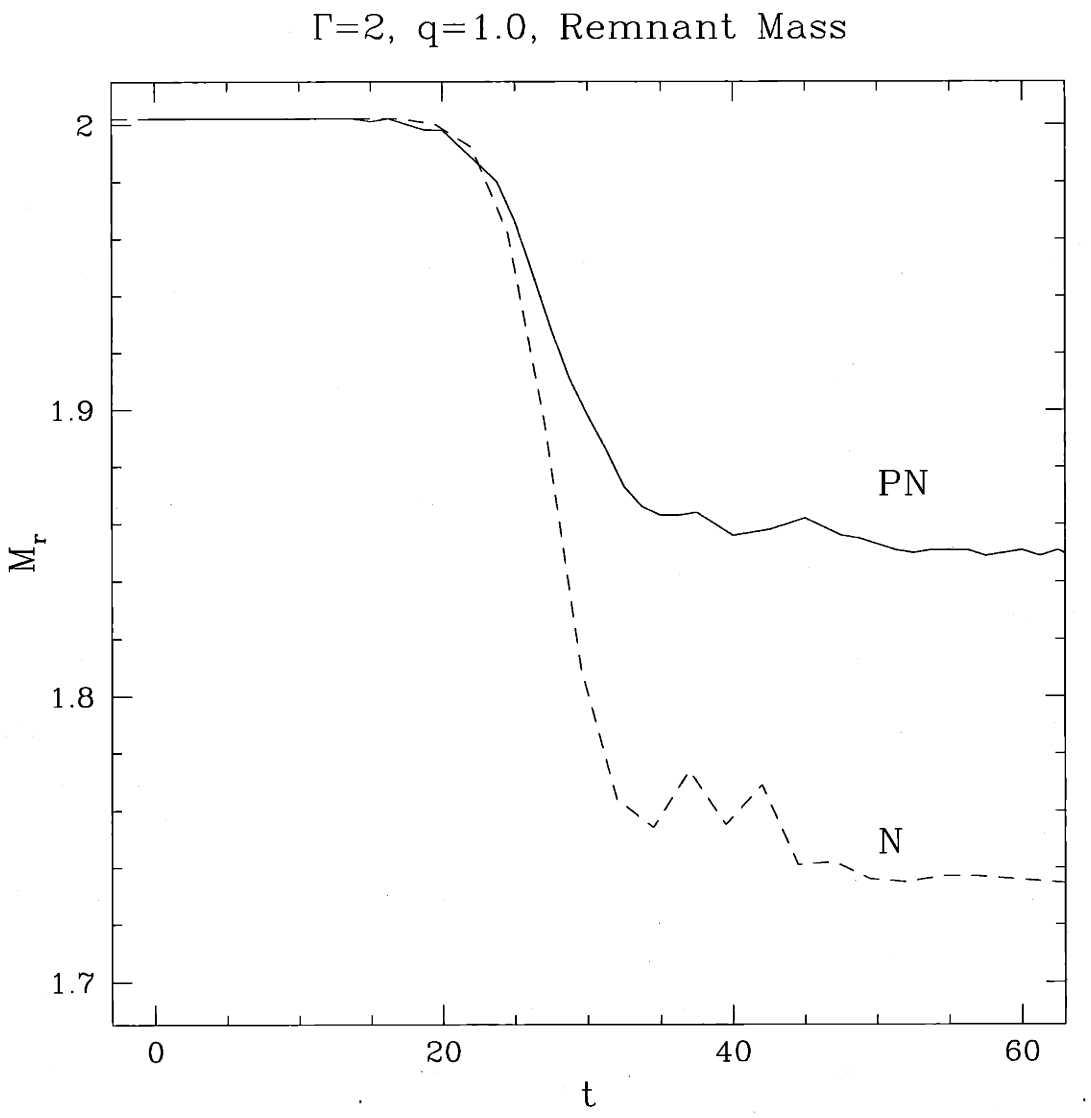

Figure 5-13: Evolution of the remnant mass for the $\Gamma = 2$, $q = 1$ runs (C1 and D1). Suppression of mass shedding in the PN case leads to a higher final remnant mass. The density cut $r_* > 0.04$, shown as dashed lines, includes the inner remnant only. The cut $r_* > 0.005$, shown as solid curves, extends further into the outer halo.

halo. This is not a surprise since, as already noted by RS2, a softer EOS produces wider spiral arms, which in turn dissipate more quickly and transport material less efficiently out to very large radii.

In Table 3.5, we list the total rest mass M_r, gravitating mass M_{gr}, and Kerr parameter a_r of the inner remnant at $t = 70$. Here the inner remnant includes all SPH particles out to a radius $r = 2$ (The results are rather insensitive to the precise choice of density cut, since the material in the halo is very tenuous).

A comparison of the angular velocity profiles of the remnants is shown in Fig. 5-15. We see, quite surprisingly, that the $\Gamma = 3$ run without 1PN corrections (A1) leads to a different form than each of the other runs. All are differentially rotating, but in all other cases the angular velocity drops as a function of distance away from the rotation axis, whereas in run A1 it increases monotonically out to $r_{\rm cyl} \simeq 1.4$, which is close to the surface of the inner remnant. Only run A1 agrees with previous purely Newtonian calculations (RS1, RS2), which found that the angular velocity increases with increasing distance from the rotation axis. However, in agreement with all previous studies, we find that the rotation profiles of all our merger remnants are pseudo-barotopic, i.e., Ω is a constant on cylinders. Recent fully GR calculations have indicated that differential rotation can increase very significantly the maximum stable mass of neutron stars (Baumgarte, Shapiro, & Shibata 2000), which makes it more likely that merger remnants can be dynamically stable against collapse to a black hole. However, differentially rotating configurations could still be secularly unstable on a viscous timescale.

Run A1 is the only one that did not produce a second gravity wave luminosity peak, suggesting that perhaps the combination of Newtonian gravity and the stiffer EOS can lead to a lower central angular momentum. In turn, this could suppress the quadrupole oscillations shown in Fig. 5-7. We also note a general difference in rotational velocity between the PN runs and the Newtonian runs, with both Newtonian runs showing an increase in angular velocity near the surface of the inner remnant, from $r_{\rm cyl} \simeq 1.2 - 1.4$, whereas the PN runs show a steady decrease through this range and out into the halo.

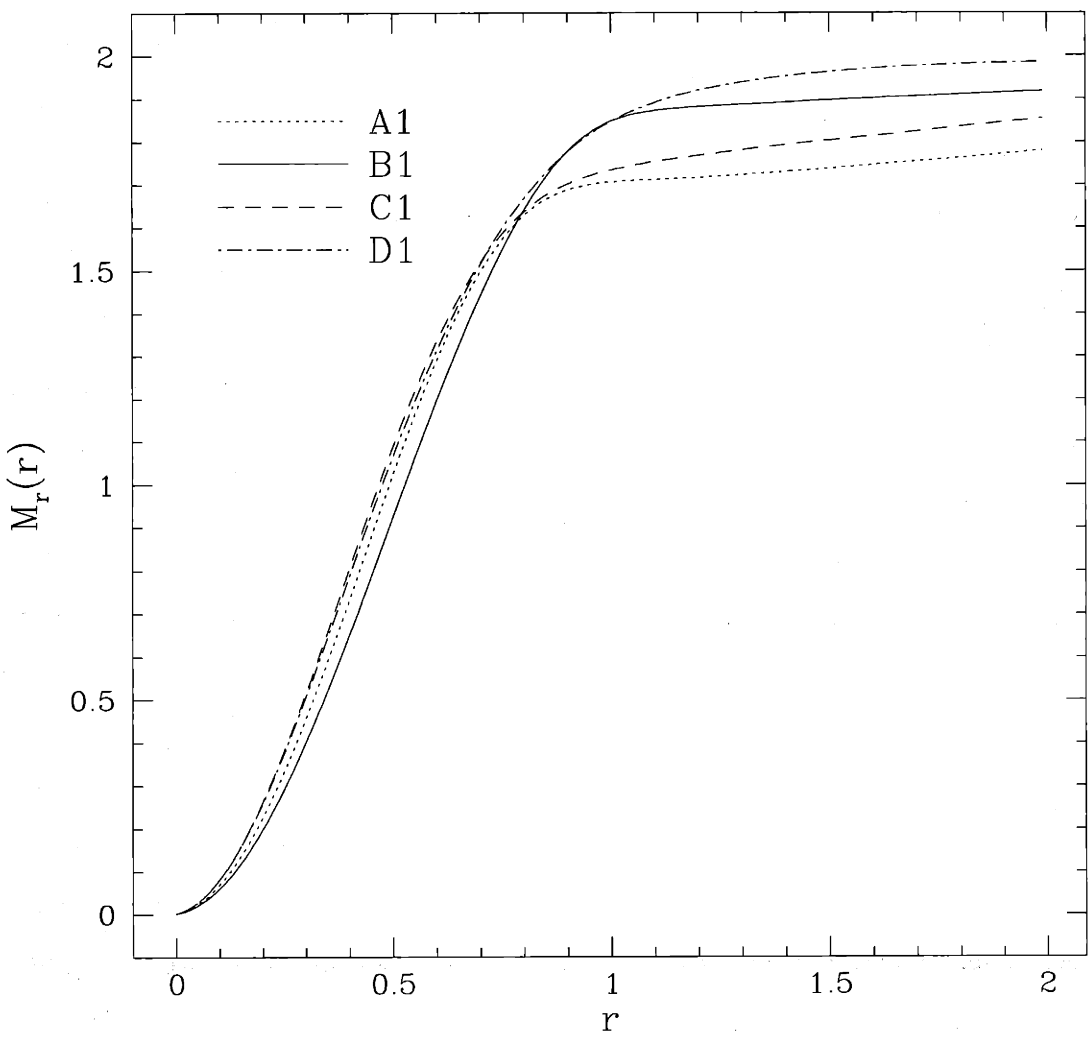

Figure 5-14: Radial mass profiles of the final merger remnants in runs A1, B1, C1, and D1 (at $t = 70$). We see that the internal structure is governed primarily by the EOS, with the $\Gamma = 2$ models slightly more centrally condensed than the $\Gamma = 3$ models, although 1PN effects do decrease the enclosed mass at small radii. At larger radii, we find more mass contained in the PN remnants, since much less mass has been ejected through spiral arms.

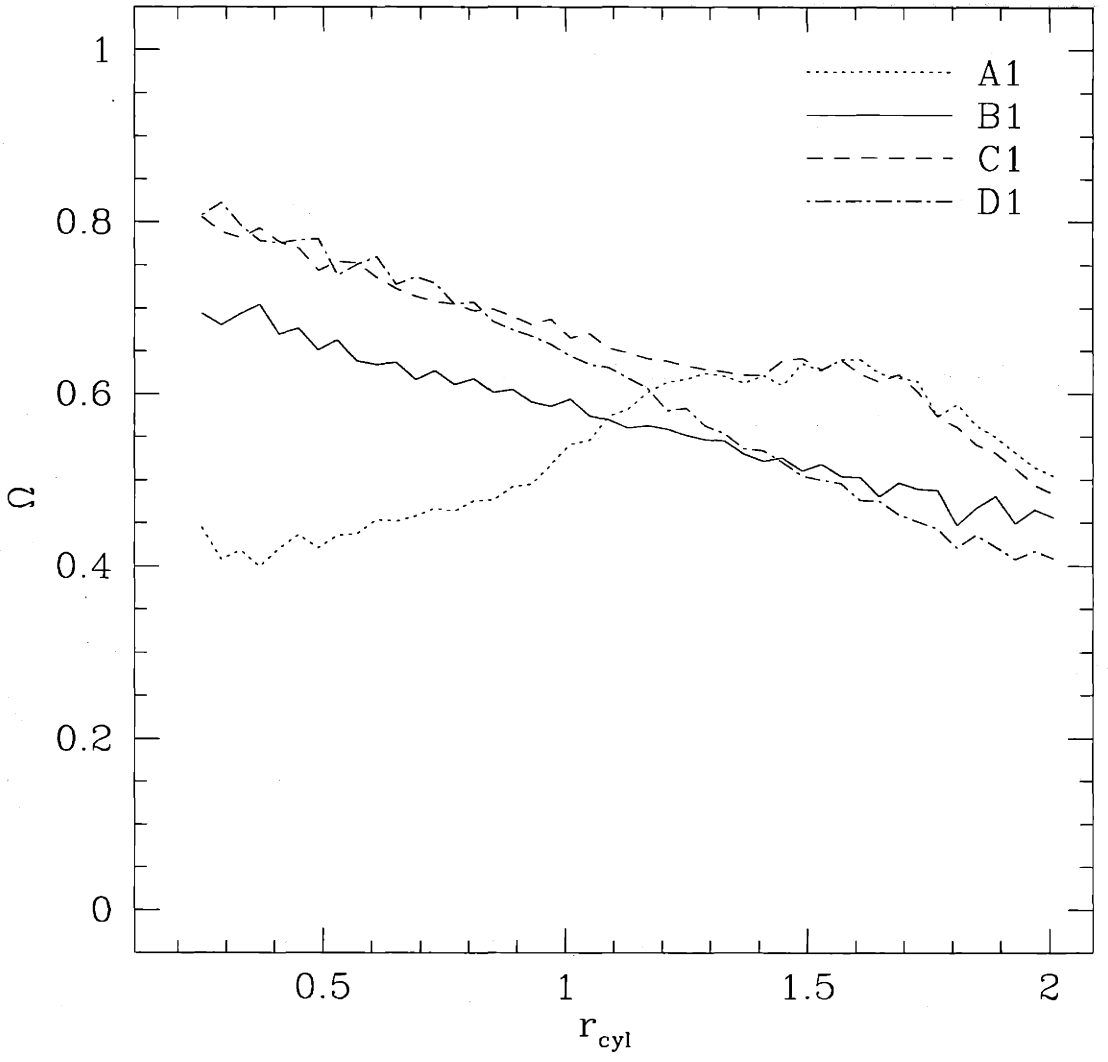

Figure 5-15: Angular velocity profiles for the same merger remnants shown in Fig. 22. We see that all are differentially rotating, and all but the Newtonian $\Gamma = 3$ remnant show a decrease in angular velocity with increasing radius for $r_{\rm cyl} < 1.3$. In general, at larger radii, the PN models show slower rotation, regardless of the EOS.

Chapter 6

Irrotational PN calculations

Having completed our survey of initially synchronized binary systems, we move on to calculations which feature an initially irrotational configuration. Such an initial state is thought to be the physically realistic description of NS binaries immediately prior to coalescence, since the timescale for tidally locking the stars into corotation is considerably longer than the coalescence timescale due to the extremely low viscosity of NS material (Bildsten & Cutler 1992; Kochanek 1992). Note that in the context of this work, the term irrotational is taken to mean that the rotation periods of the NS are large with respect to the the dynamical time of the system, $t_D \approx 0.07$ ms. Thus, NS with periods of $P \approx 1$ s would be considered essentially irrotational. We performed calculations designed to study the dependence of gravity wave signals on the EOS and system mass ratio, as well as to study the dependence on the initial spin of the system, in order to properly determine the relevance of synchronized calculations, which although unphysical, are easier in general to perform.

Although the coalescence process is essentially the same qualitatively for both types of initial spin, they present different computational challenges. To demonstrate this, in Fig. 6-1 we show the evolution of run E1, with a $\Gamma = 3$ EOS, a mass ratio $q = 1.0$, and an initial separation of $r_0 = 4.0\ R$. It is in all ways similar to run B1, except that the NS start from an initially irrotational configuration. Rather than plot SPH particle positions, we instead show the density contours of the matter, overlaying the velocity of the material in the inertial frame. Unlike the case of initially synchronized

binaries, in which the material maintains a small velocity in a frame which corotates with the binary throughout the period prior to first contact, in irrotational binaries material on the inner edge of each NS is counterspinning in the corotating frame, and thus we see a large discontinuity in the tangential velocity when first contact is made. This surface layer, initially at low density, is Kelvin-Helmholtz unstable to the formation of turbulent vortices on all length scales. Meanwhile, material on the outer edge of each NS has less angular momentum in an irrotational binary configuration than in a synchronized one. Thus, there is less total angular momentum in the system, and mass shedding is greatly suppressed, as we will discuss further in Sec. 6.2.

6.1 Tests and results

There are a number of difficulties which are introduced by an irrotational binary. One consideration is the spurious viscosity found in any numerical scheme, which is significantly larger than the true physical viscosity in this case. Because of this, any calculation which features a long evolution prior to merger will show some degree of synchronization. The corresponding advantage in decreasing the initial separation r_0 must be balanced against the benefits of a large initial separation, primarily in allowing the initial deviations from equilibrium to dissipate.

Additionally, the Kelvin-Helmholtz unstable layer which forms at the surface of contact between the NS presents a numerical challenge. Inherently, the results should be sensitive to some degree upon the numerical resolution of the calculation. However, the large-scale physics of the merger should remain qualitatively unchanged. To test the robustness of our results, we ran calculations using a broad range for the number of SPH particles, seeking to determine the number required in any calculation to achieve numerical convergence.

6.1.1 Initial separation of irrotational configurations

There are a number of competing factors that affect the determination of which initial binary separation r_0 to choose for our calculations. Traditionally, the standard choice

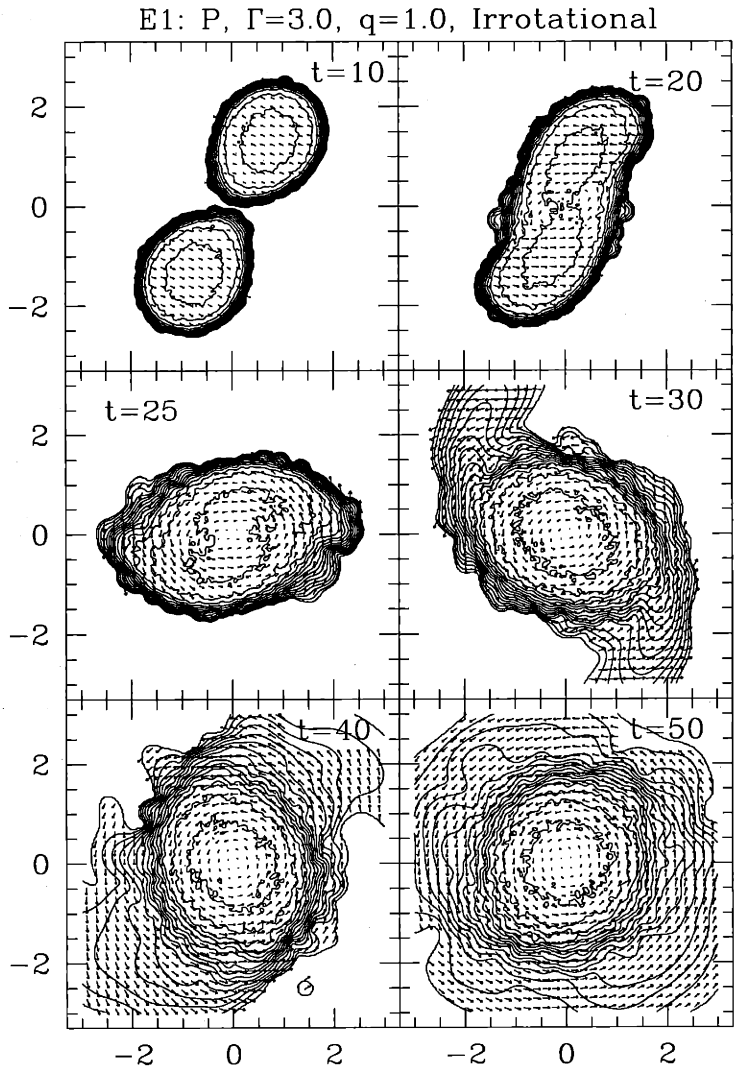

Figure 6-1: Density contours overlaid with velocity vectors for the evolution of run E1, with a $\Gamma = 3$ EOS, q=1, and an irrotational initial condition. Upon first contact of the NS, a surface layer forms as counterstreaming material forms turbulent vortices. As the cores of the respective NS continue to inspiral, we eventually find the formation of a merger remnant with a well-organized and coherent circular differential rotation pattern.

is the largest possible separation for which the calculation can be performed using a reasonable amount of computational resources. This method has the advantage that any initial deviations from equilibrium will generally be damped away before the NS actually make contact. It also allows for the best determination of the dynamical stability limit, since stellar oscillations can play such a large role in calculations which use PN gravity. There are caveats, though, in the case of initially irrotational binaries, since numerical viscosity inherently present in SPH codes can lead to some degree of vorticity in the respective NS during the inspiral phase. Thus, by the time the merger takes place, the stars will no longer be completely irrotational. To study this effect, we calculated mergers for equal-mass NS with a $\Gamma = 3$ EOS starting at initial separations of $r_0 = 4.0$ and $r_0 = 3.5$. In the top panel of Fig. 6-2, we show the binary separation as a function of time for both runs, with the initial times defined such that the respective gravity wave luminosity peaks are simultaneous. We see good agreement throughout, although the during the merger itself we do show a slight discrepancy, which is attributable in part to greater mass shedding in the calculation started at greater separation.

It should be noted that in both runs the most noticeable effect on the binary separation as a function of time is a slight ellipticity in the orbit, with a period corresponding to the orbital period of the binary itself. This should not be seen as evidence that the initial oscillations about equilibrium are unimportant in dynamical runs which include radiation reaction effects. From the top panel of Fig. 3-5, we know that oscillations are visibly present even when radiation reaction effects are included. While these oscillations in the infall velocity of the binary may be of small amplitude, they are at a frequency an order of magnitude larger than that of the orbital frequency, and thus play a strikingly more dramatic role in the inwardly directed acceleration of the binary.

In the bottom panel of Fig. 6-2, we plot the net spin angular momentum of the NS about their own centers of mass as a function of time. We see that the NS do gradually acquire a rotation pattern which corresponds to the direction of corotation, although there is nowhere near enough time to synchronize the binary. The effect

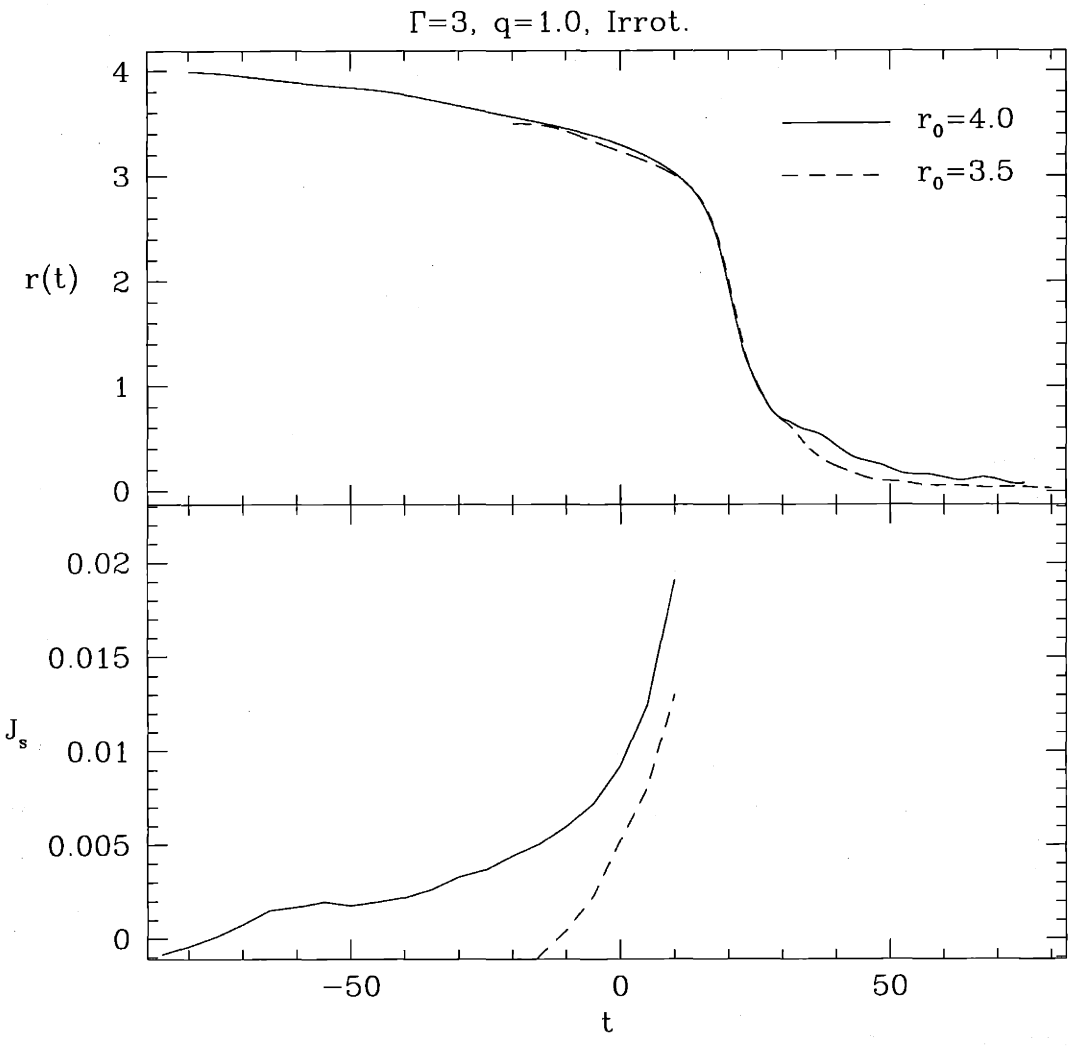

Figure 6-2: Binary separation (top panel) and spin angular momentum (bottom panel) as a function of time for irrotational binary systems with a $\Gamma = 3$ NS EOS and q=1.0, started from an initial separation of $r_0 = 4.0R$ (solid lines) and $r_0 = 3.5R$ (dashed lines). The binary with greater initial separation does show greater spin angular momentum throughout the calculation prior to merger.

is greatly enhanced immediately prior to merger in both case, as the NS develop tidal lag angles and become distorted. By the time the binary initially started from $r_0 = 4.0R$ reaches a separation of $r = 3.5R$, the net angular momentum around each NS center of mass is equal to approximately 0.5% the value we would expect should the binary be synchronized. This difference persists throughout the inspiral phase when the two calculations are compared.

In Fig. 6-3, we compare the gravity wave forms and luminosities for the two runs. We find excellent agreement between the two wave forms, both in amplitude and in phase. Both runs show the modulated, damped gravity wave luminosity which is characteristic of all runs we have computed using PN gravity. There is a slight difference in the amplitude of the signal during the second gravity wave luminosity peak, but we expect the difference to be minor compared to effects such as uncertainty in the equation of state and the larger issue of a proper relativistic treatment of gravitation.

To highlight the difference in the effect of our initial separation on our final results, we show the final mass and angular velocity profiles of the remnants for the two calculations in Fig. 6-4. The results are in good agreement, although we see that the greater spin angular momentum of the run started at greater initial separation leads to approximately three times as much mass being deposited in a halo which surrounds the remnant while remaining gravitationally bound to it. In both cases, however, the total mass in the halo is less than 1% of the total system mass. The inner region of the remnant in the run started from $r_0 = 4.0$ actually spins slightly slower than in the run started further inward, even though the NS have a greater spin angular momentum at the moment of first contact, but only because angular momentum transport outward was marginally more efficient in this case.

6.1.2 Dependence on numerical resolution

A serious problem for all irrotational calculations involves the surface layer that develops between the two NS upon first contact. An irrotational initial condition leads to a large velocity shear between the outer surfaces of the respective NS, since both

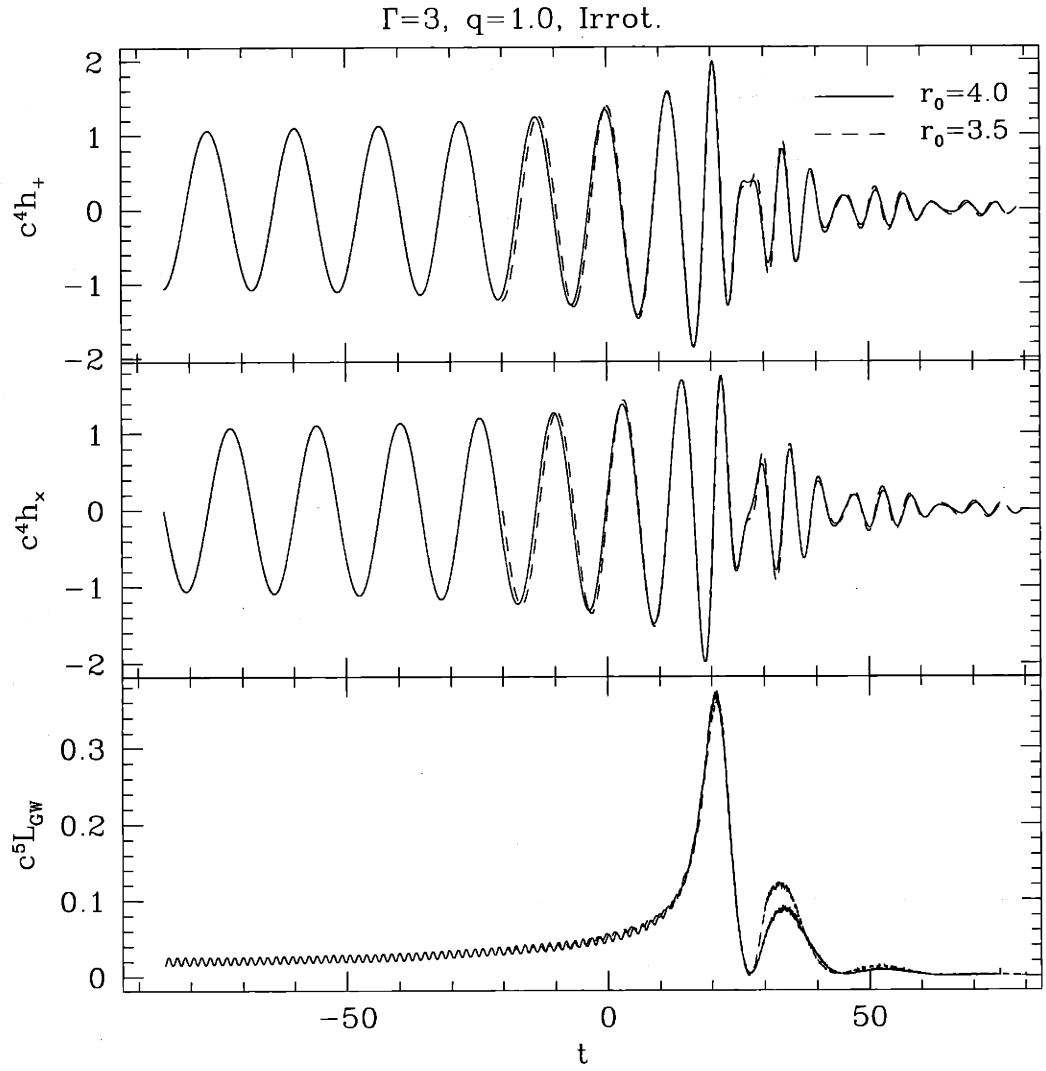

Figure 6-3: Gravity wave forms in both polarizations (top and middle panel) and gravity wave luminosities (bottom panel) for the two runs described in Fig. 6-2, calculated from Eqs. 1.21, 1.22, & 1.25. The agreement is excellent throughout, except for a slight difference in the amplitude of the second gravity wave peak.

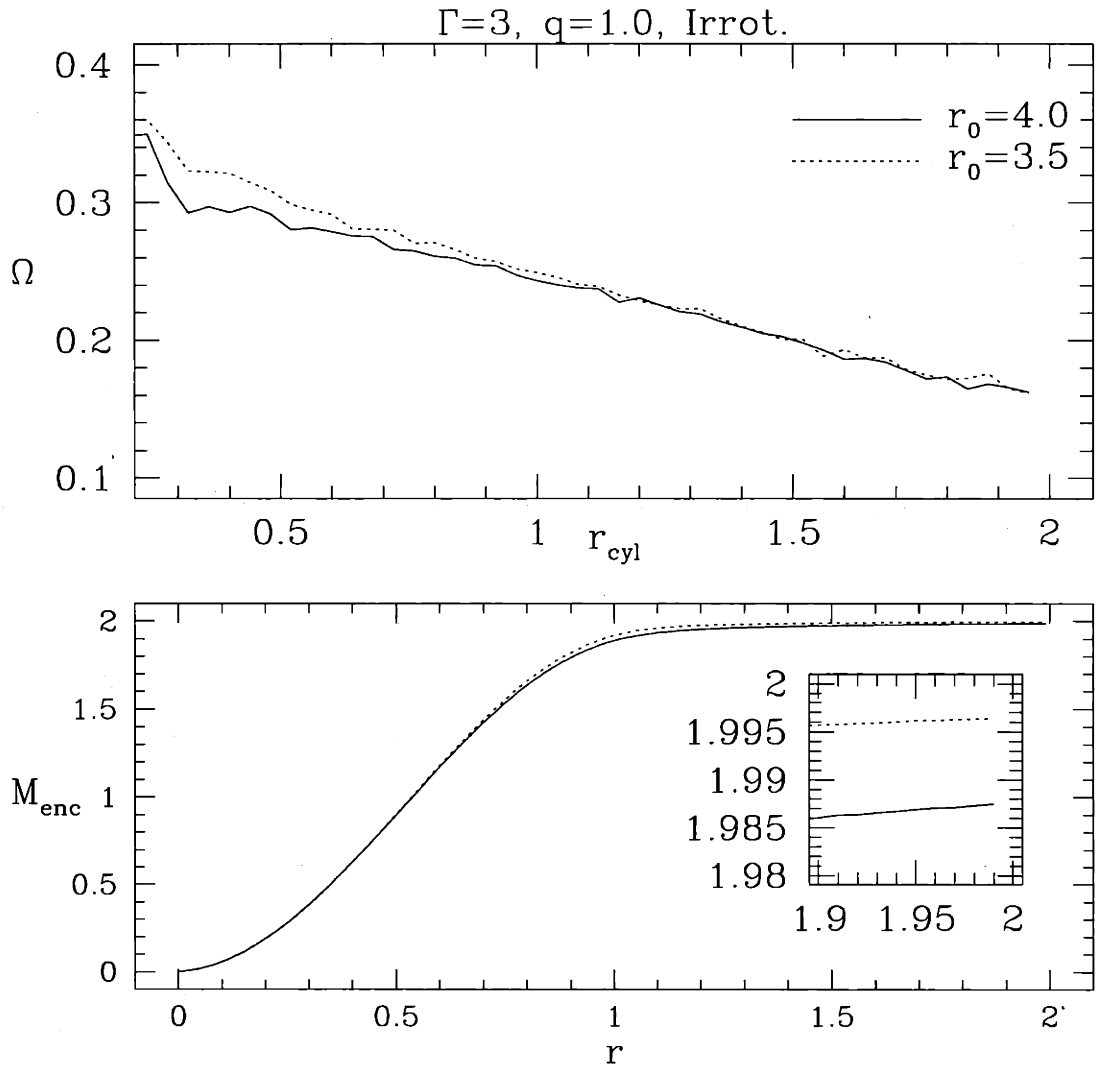

Figure 6-4: Angular velocity as a function of cylindrical radius (top panel) and enclosed mass as a function for the remnants of the runs shown in Fig. 6-2. The profiles are taken at $T = 65$ for both runs. We see that mass shedding to larger radii is more efficient for the calculation started from $r_0 = 4.0$, but that in both cases virtually all the matter in the system ends up in the remnant itself. The inset shows the profile at the outer edge of the system, indicating that no more than $\sim 0.5\%$ of the material is ejected to larger radii.

are counterspinning in the corotating frame. This leads to the formation of a vortex sheet at the surface of contact which is Kelvin-Helmholtz unstable on all physical scales. Such instabilities are extremely worrisome for numerical calculations, which cannot accurately model the small-scale behavior of the unstable region.

In order to study the effect of resolution dependent effects on the gravitational wave signals derived from NS merger calculations we performed three calculations with a wide range in the number of SPH particles used. Respectively, they use 5×10^3, 5×10^4, and 5×10^5 particles per NS (i.e., $N = 10^4$, 10^5, and 10^6 total SPH particles). The optimal number of neighbors is set to $N_N = 50$, 100, and 200 respectively for the runs. We believe that the last of these stands as the most detailed calculation ever done of a binary NS merger.

A comparison of the gravity wave signals in both polarizations, as well as the gravity wave luminosities, is shown in Fig. 6-5. We see that the lowest resolution run produces a gravity wave signal qualitatively different than higher precision runs, due in part to large initial oscillations. As all three calculations featured relaxed single-star components which were linearly rescaled into an ellipsoidal configuration, we conclude that the amplitudes of the initial fluctuations in the gravity wave signal result primarily from statistical effects associated with sampling errors. The two runs with higher resolution show good agreement throughout the calculation, producing nearly equal gravity wave luminosities. Reassuringly, the gravity wave signals produced by the respective runs remain in phase throughout as well, indicating that calculations that use $N = 10^5$ can indeed model well the large-scale effects associated with the merger process.

The vortices which form at the surface of contact are shown in detail in Fig. 6-6. Density contours are overlaid with velocity vectors, which are plotted in the corotating frame. To define this frame, we use a particle-averaged tangential velocity, such that

$$\Omega_c = \frac{\sum_i m_i[(xv_y - yv_x)/r_{cyl}]_i}{\sum_i m_i (r_{cyl})_i}, \tag{6.1}$$

where the cylindrical radius is defined as $r_{cyl} = \sqrt{x^2 + y^2}$. The top panels show the

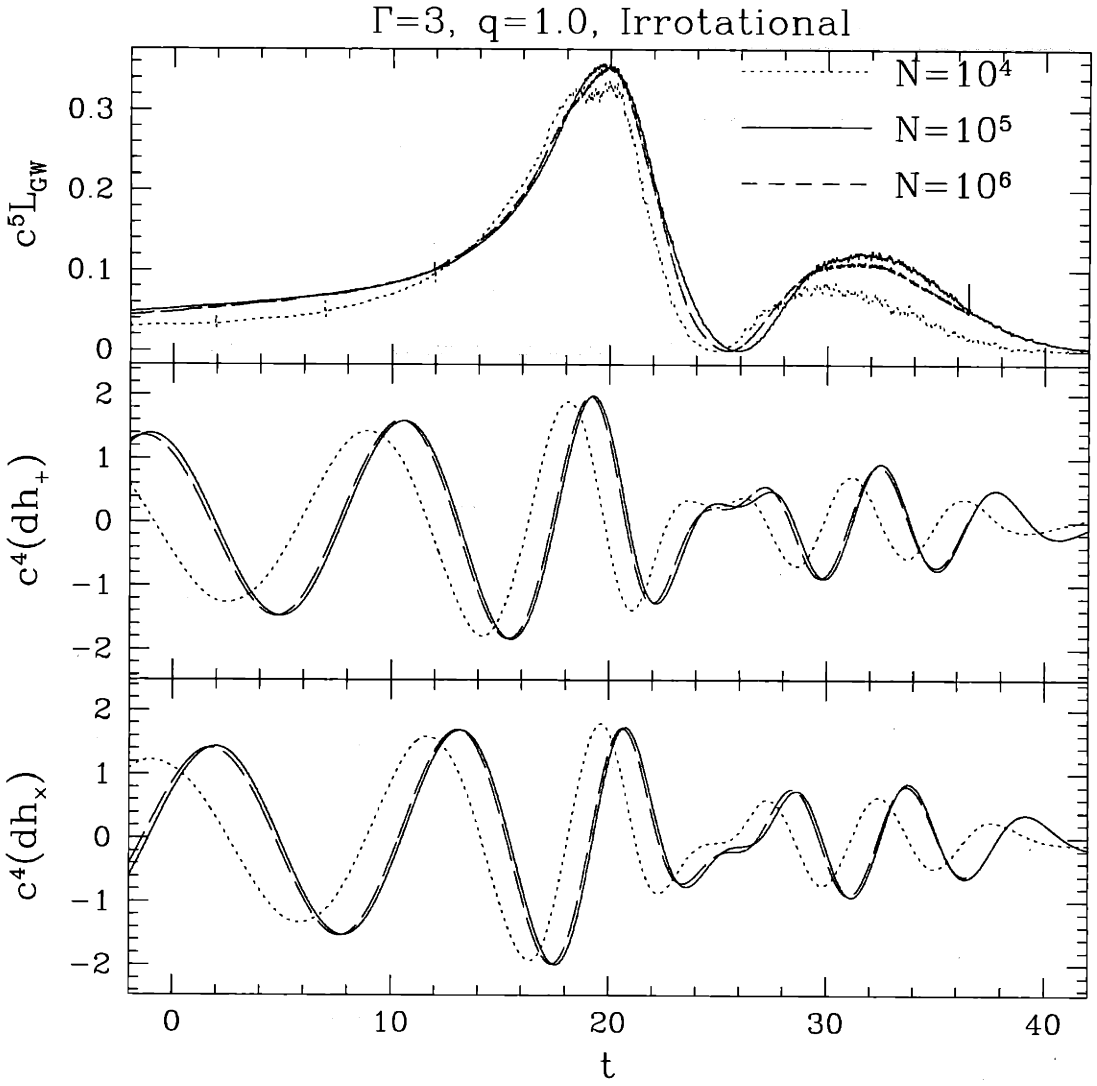

Figure 6-5: Gravity wave luminosities (top) and waveforms (middle and bottom) for calculations using various number of particles. The dotted curve corresponds to 10^4 SPH particles, the solid curve to 10^5, and the dashed curve to 10^6. We see that the two highest resolution runs agree almost perfectly. The lowest resolution run is more susceptible to initial deviations from equilibrium, and shows some qualitative differences with the higher resolution runs, especially after the first gravity wave luminosity peak.

evolution of the run with 10^4 SPH particles, with the middle and bottom panels representing the runs with 10^5 and 10^6 SPH particles, respectively. We see in the leftmost panels the state of the three runs at $t = 20$. Immediately apparent is that vortices have begun to form in the lowest resolution run, whereas in the higher resolution run there is very little sign of particles mixing, except at a large distance from the center of the forming remnant along the vortex sheet. By $t = 25$, shown in the center panels, we see that the lowest resolution run continues to look qualitatively different than the other two calculations. There is a slight difference between the high resolution calculations with regard to the direction of the material flowing along the vortex sheet. In the highest resolution run, the streams of material flow nearly in a straight line from one vortex to the other, whereas in the middle run, there is a larger region of material which is accelerated toward the very center of the remnant. Overall, though, there is excellent agreement between the two calculations. Finally by $t = 30$ in the rightmost panels, we see that the vortices formed have merged into the center of the remnant, leaving a characteristic differentially rotating patter. It is more coherent for the higher resolution runs, especially the run with 10^6 particles.

6.2 Equal-mass calculations

To study the effect of the choice of EOS on the evolution of irrotational NS binaries, we calculated mergers for both choices of EOS ($\Gamma = 3$ and $\Gamma = 2$ polytropes) with equal-mass NS, each containing $N = 5 \times 10^4$ SPH particles, with an initial separation of $r_0 = 4.0R$. A comparison of the binary separations, along with the gravity wave luminosities and wave forms are shown in Fig. 6-7. Immediately apparent is a difference in the location of the dynamical stability limit for the two calculations. The orbit of NS with a softer EOS remains stable at separations where the stiffer EOS has already begun to plunge inward toward merger. We see that as in the synchronized case presented in Sec. 5.1, the peak gravity wave luminosity is larger for the softer choice of EOS, but after a secondary luminosity peak, the remnant relaxes toward a spheroidal, non-radiating configuration, with essentially no emission whatsoever after

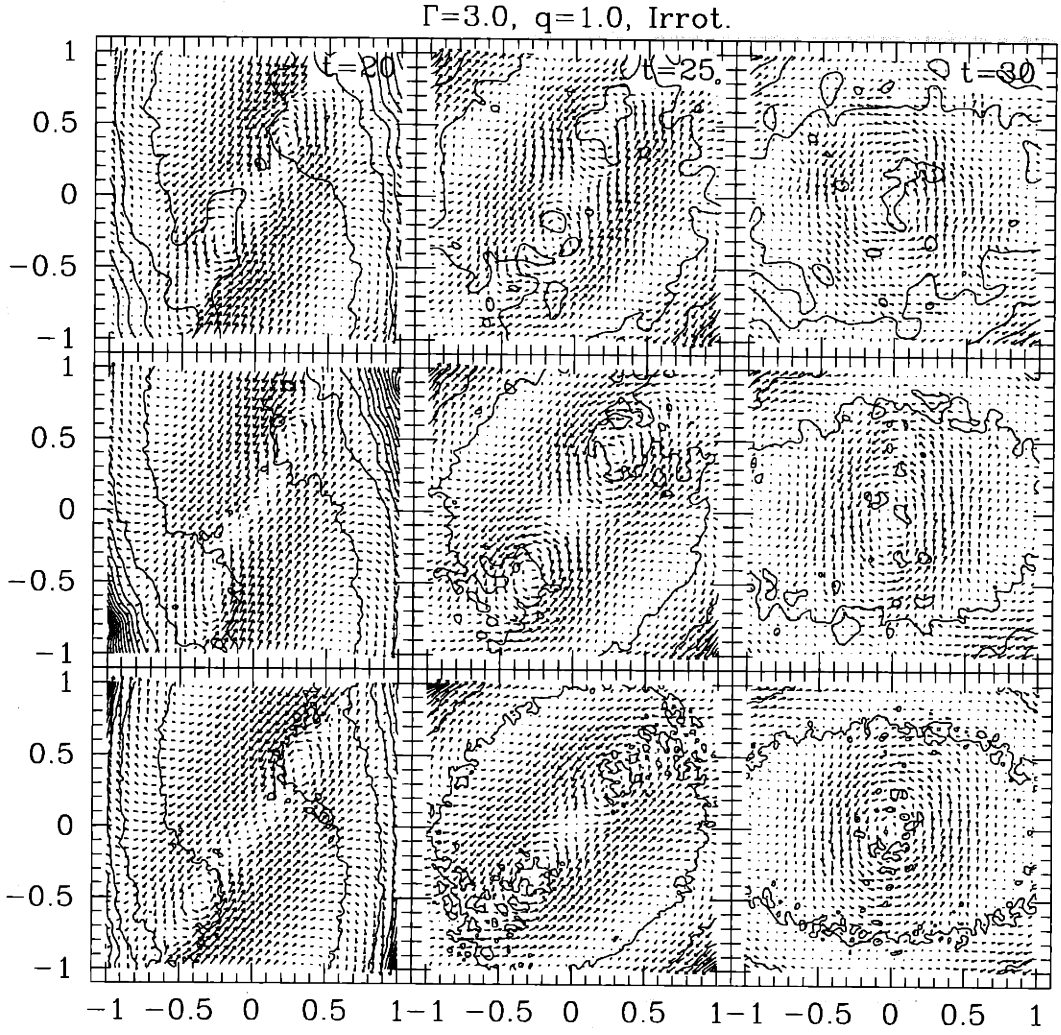

Figure 6-6: Density contours overlaid with velocity vectors shown in the corotating frame of the binary (See Eq. 6.1) for calculations which use a total of 10^4 (top), 10^5 (middle), and 10^6 (bottom) total SPH particles. Leftmost panels show the system at $t = 20$, center panels at $t = 25$, and rightmost panels at $t = 30$. We see some divergence between the lowest resolution run and the two higher resolution runs, which agree well throughout.

$T \sim 40$. We also note that the secondary peak occurs sooner after the primary peak, by a factor of $\sim 30\%$.

Even though they are presumed to be unphysical, calculations started from a synchronized initial condition make up much of the body of work performed to date on the binary NS coalescence problem. Noting this, we compare our irrotational run with a $\Gamma = 3$ EOS, $q = 1.0$, and an initial separation of $r_0 = 4.0$ to one similar in every respect but started with a synchronized initial condition. Comparing the evolution of run E1, shown in Fig. 6-1 to the evolution of run B1, shown in Fig. 4-2, we see that in both cases, the stars develop a large tidal lag immediately before merger, leading to an "off-center" collision and a highly asymmetrical merger, which is found in both cases to persist until $t \simeq 50$.

In the top panel of Fig. 6-8, we see that the inspiral tracks do not align particularly well. Synchronized binaries contain more total energy, and are less dynamically stable than irrotational ones, leading to a more rapid inspiral, even before the stability limit is reached. Additionally, the binary separation "hangs up" even earlier, at a separation of $r \approx 2.0$, indicating the onset of mass shedding. This is similar to what was seen in Sec. 6.1.1, where the run which had acquired greater spin angular momentum showed greater mass shedding, but the effect is greatly magnified in the synchronized case. The middle and bottom panels of the figure show the gravity wave forms and luminosity, respectively, for two runs. While the initial peaks are similar for both runs, both in amplitude and morphology, the secondary peaks are vastly different. The secondary peak for the synchronized calculation is considerably stronger than the irrotational case, and delayed relative to it. We conclude that while the EOS seems to be the dominant factor in determining the gravity wave signal during the merger itself, the initial spins of the NS play a key role in the evolution of the remnant, as well as affecting the orbital dynamics during inspiral.

To better understand the features found in the gravity wave forms of these calculations, particle plots for the runs described above are shown in Fig. 6-9. Comparing the leftmost panels, we see that at $T = 20$, when the gravity wave luminosity peaks, the mass configurations are qualitatively similar, although the run with the $\Gamma = 2$

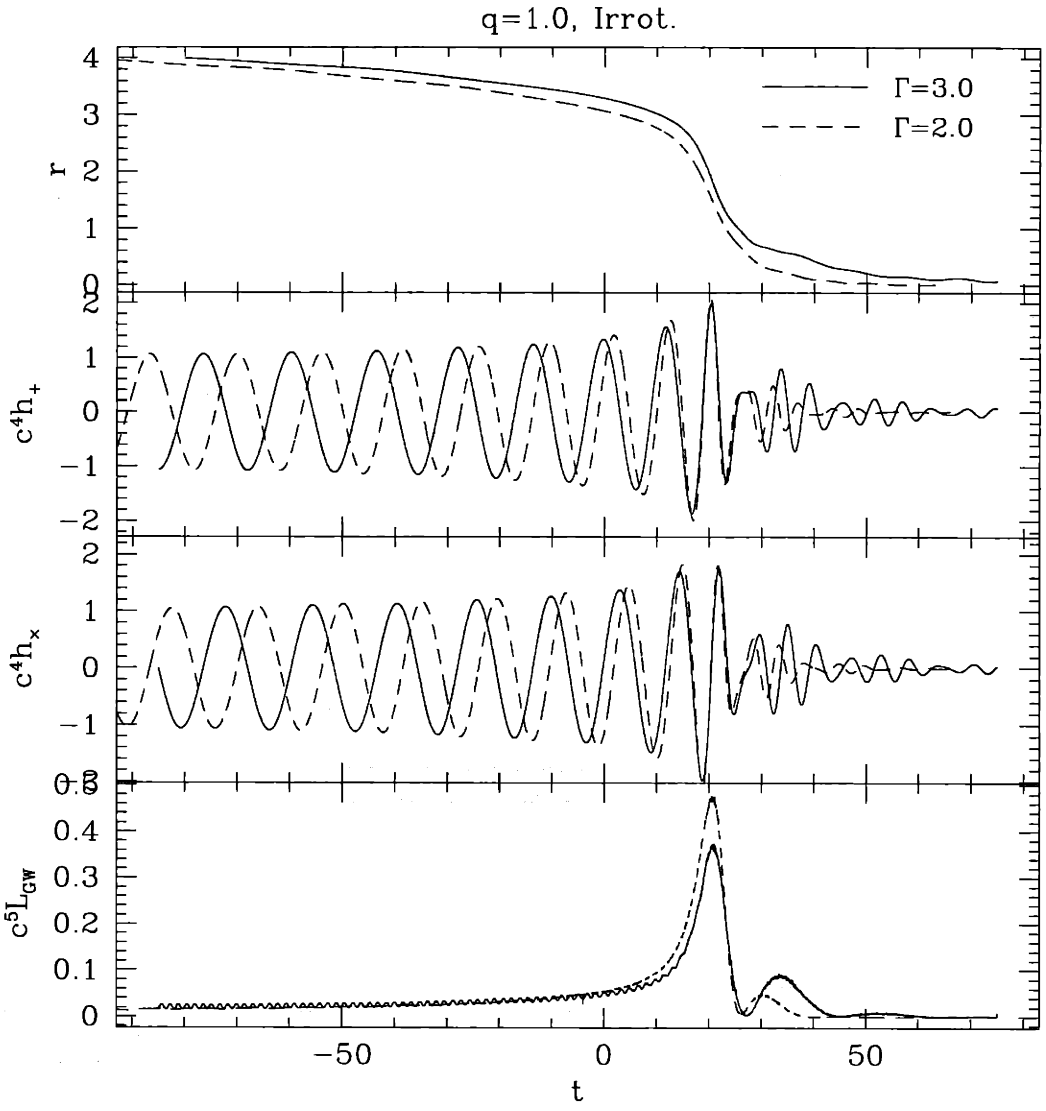

Figure 6-7: Binary separation (top panel), gravity wave forms (middle panels) and gravity wave luminosity (bottom panel) as a function of time for our irrotational, equal-mass runs started from $r_0 = 4.0$. The solid curve corresponds to NS with a $\Gamma = 3$ EOS, dashed to a $\Gamma = 2$ EOS. The dynamical stability limit for the softer EOS lies within that of the stiffer one. The softer EOS also results in a higher peak gravity wave luminosity, but no late-time gravity wave emission.

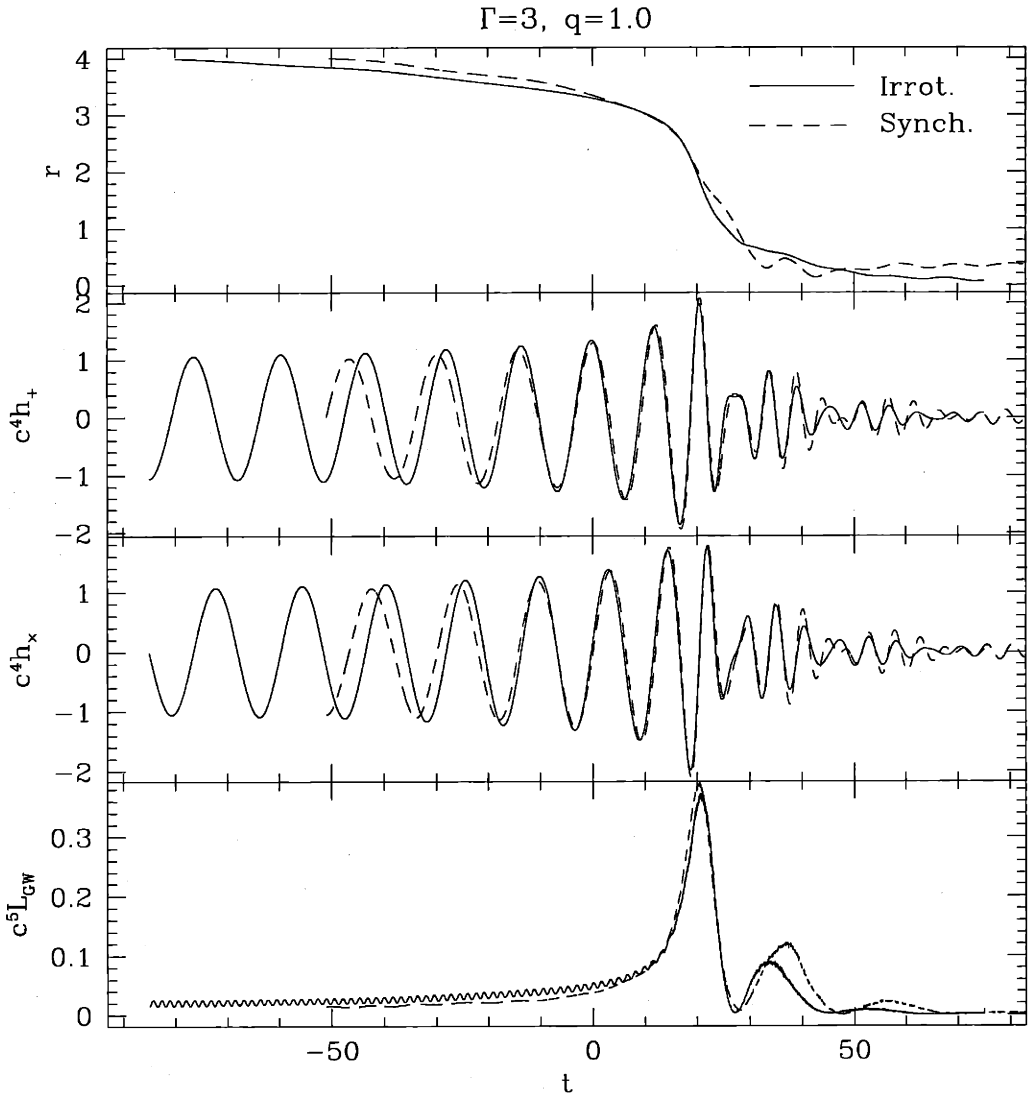

Figure 6-8: Binary separation (top panel), gravity wave forms (middle panels) and gravity wave luminosity (bottom panel) as a function of time for our equal-mass, $\Gamma = 3$ EOS runs, started from an irrotational (solid) and a synchronized (dashed) initial condition. The synchronized run contains more energy and is relatively more dynamically unstable. While the initial peaks in the gravity wave luminosities are of similar amplitude, the secondary peaks are much more luminous for the synchronized binary.

EOS shows more low-density material at the edges of the newly forming remnant, conforming to the general density profile expected of a softer EOS. More subtle is the greater extension present in the synchronized run. Since material on the outside of each NS has greater angular momentum when a synchronized initial condition is chosen, the calculation shows much greater efficiency at channeling material outward during the final moments of inspiral. This difference is made abundantly clear by a comparison of the calculations at $T = 30$, shown in the center panels. We see extensive mass shedding from the synchronized run, much less from the irrotational runs. There is significantly more mass shedding from the run with the softer EOS, but most of the material remains extremely close to the remnant. Finally, by $T = 45$, we see that the softer EOS produces a nearly spherical remnant, whereas the calculations with a stiffer choice of EOS produce remnants which are clearly ellipsoidal, and will continue to radiate gravity waves for some time, albeit at a much lower amplitude than at the peak.

The strong influence of the choice of both EOS and spin on the final state of the remnant is shown in Fig. 6-10. In the top panel, we see the angular velocity profiles of the remnants at $T = 65$. We see that the choice of EOS plays an important role near the center of the remnant, but at $r > 1.0R$, the velocity profiles are essentially identical. The pattern holds as well for the mass profiles, which are shown in the bottom panel. The softer EOS leads to a more centrally condensed remnant, as we would expect, but both remnants formed in irrotational calculations contain virtually all the system mass within $r \approx 2.0R$, with no more than 1% escaping to larger radii. There is slightly more mass shedding past this point for the softer choice of EOS, since more of the low-density material originally found at the edges of the NS is shed through the outer Lagrange points of the system. By comparison, the initially synchronized run sheds almost 5% of the total system mass past $r > 2.0R$, even though the angular velocity profile at small radii is nearly the same as for the irrotational run with the same choice of NS EOS.

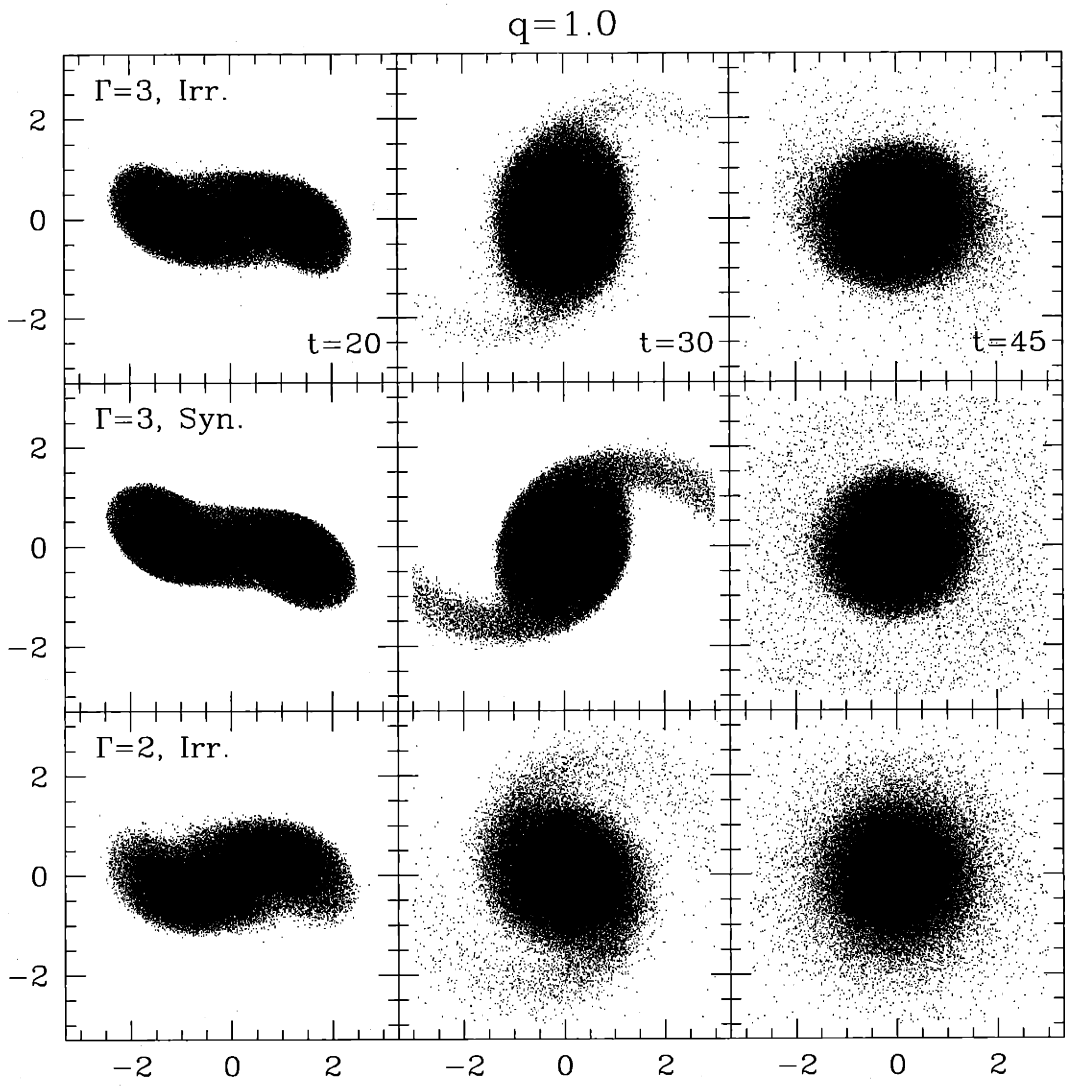

Figure 6-9: Particle plots for the runs described in Figs.6-7 and 6-8. The top panels show the $\Gamma = 3$ Irrotational run, the middle panels the $\Gamma = 3$ Synchronized run, and the bottom panels the $\Gamma = 2$ Irrotational run. The plots represent the configuration of all SPH particles at $T = 20$ (left), $T = 30$ (center), and $T = 45$ (right). We see that mass shedding is more sensitively dependent on the initial spin, but the remnant ellipticity, and thus the long-term gravity wave emission, is dominated by the choice of EOS.

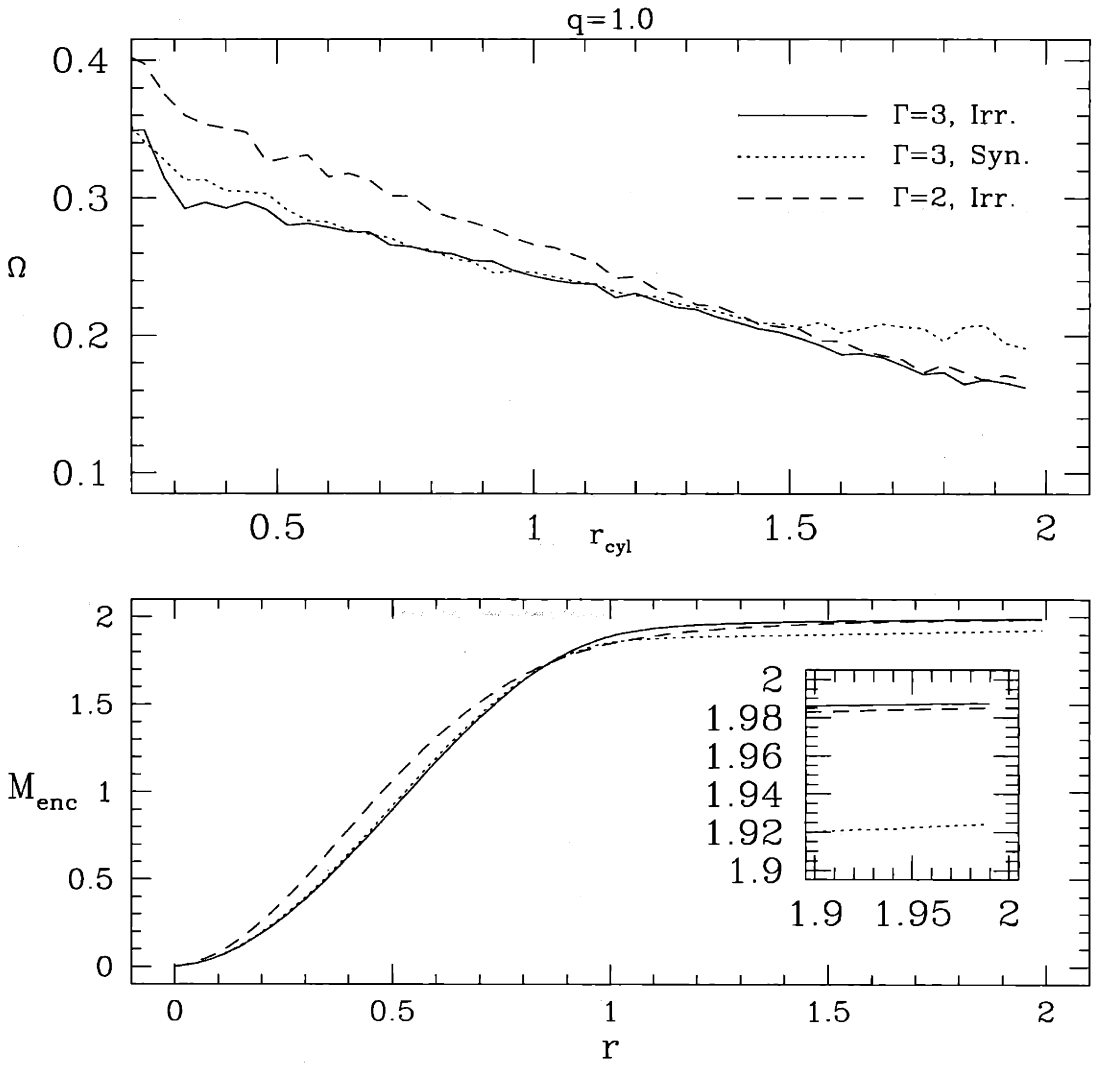

Figure 6-10: Angular velocity as a function of cylindrical radius (top panel) and enclosed mass as a function for the remnants of the equal-mass runs shown in Figs.6-7 and 6-8. The profiles, all taken at $T = 65$, correspond to the irrotational runs with $\Gamma = 3$ EOS (solid) and $\Gamma = 2$ EOS (dashed) and the synchronized run with $\Gamma = 3$ EOS (dotted).

6.3 Unequal-mass calculations

Even though all well-measured NS masses in relativistic binaries are roughly consistent with a single NS mass $M_{NS} \approx 1.4 M_{\odot}$ (Thorsett & Chakrabarty 1999), it is important to consider cases where the two NS have different masses. The roles played by the primary and secondary in such a system are remarkably different from the picture developed above for equal-mass systems. In Sec. 5.2, we found that the primary generally remains virtually undisturbed in unequal-mass mergers, falling toward the middle of the newly forming merger remnant. The secondary is tidally disrupted prior to merger, forming a single thick spiral arm. Most of the material originally located in the secondary eventually forms the outer region of the merger remnant, but a significant amount of material is shed to form a thick torus around the remnant. In Fig. 6-11, we show particle plots for irrotational runs with a mass ratio $q = 0.8$ and both choices of EOS. In the leftmost panels, which show the respective calculations at $t = 20$, we see that the secondary, located on the left, is tidally stretched as it falls onto the primary. For the softer ($\Gamma = 2$ polytropic) NS EOS, we see a greater extension of the the secondary immediately prior to merger, as well as early mass shedding from the surface of the primary, as material from the secondary essentially blows it off the surface of the newly forming remnant. This process continues, so that by $T = 30$ (center panels), the secondary has begun to shed a considerable amount of mass in a single spiral arm which wraps around the system. Much like in the equal-mass case, the spiral arm is much broader for the softer EOS. Mass loss from the primary is greatly reduced in the system with the stiffer EOS, with only a scattering of particles originally located in the primary lifted off the surface. Finally, by $T = 45$ (right panels), we see that the spiral arm has in both cases begun to dissipate, leaving a torus around the merger remnant containing approximately $3 - 4\%$ of the total system mass.

Although the merger process is significantly different for equal-mass and unequal-mass binaries, the details of the inspiral phase are reasonably similar. In particular, the evolution of the binary separation for runs with $q = 0.8$, shown in the top panel of

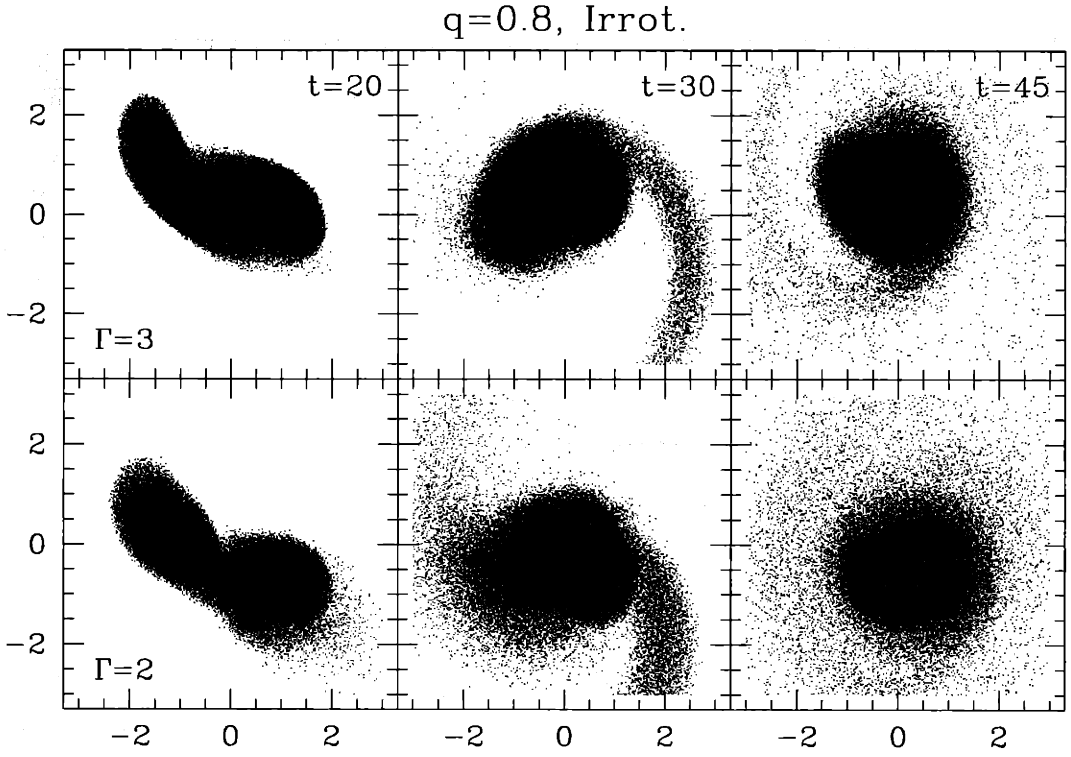

Figure 6-11: Particle plots for the irrotational runs with mass ratio $q = 0.8$ and a NS EOS given by a $\Gamma = 3$ polytrope (top panels) and a $\Gamma = 2$ polytrope (bottom panels). From left to right, we see snapshots taken at $T = 20$, $T = 30$, and $T = 45$, showing in both cases the tidal disruption of the secondary, the formation of a single spiral arm during mass shedding, and the eventual creation of a massive torus around the merger remnant.

Fig. 6-12 is roughly similar to what was found in Fig. 6-7 for binaries with $q = 1.0$. For both choices of the NS EOS, the dynamical stability limit is located at approximately the same separation for both $q = 0.8$ and $q = 1.0$ binaries, although prior to the onset of instability the more massive equal-mass binaries show a more rapid stable inspiral. As we found before, the dynamical stability limit occurs further inward for the softer choice of the NS EOS.

In Sec. 5.2, we found that the scaling of the gravity wave amplitude and luminosity as a function of the system mass ratio followed a steeper power law in synchronized binaries than would be predicted by Newtonian point-mass estimates, with the discrepancy resulting from the unequal role played by the two components during the final moments before plunge. The primary, which remains relatively undisturbed, contributes rather little to the gravity wave signal, especially during the final moments before coalescence. Thus, the gravity wave power is reduced as the mass ratio is decreased. Similar results were found for PN calculations of synchronized binaries, especially a steeper decrease in the gravity wave luminosity as a function of the mass ratio for binaries with a soft NS EOS.

In the middle and bottom panels of Fig. 6-12 we show the gravity wave forms and luminosity, respectively, for the irrotational runs with $q = 0.8$. We find the same strong decrease in the gravity wave power, especially for the softer EOS. We expect that there should be a strong observational bias towards mergers with equal-mass components should NS-NS binaries be seen with LIGO or other detectors, especially if the NS EOS is extremely soft. Even if the physical NS EOS is as stiff as our $\Gamma = 3$ polytropic model, we expect there to be a considerable difference in cosmic volume for which mergers will eventually be above noise thresholds for binaries with mass ratios of $q = 1.0$ and $q = 0.9$.

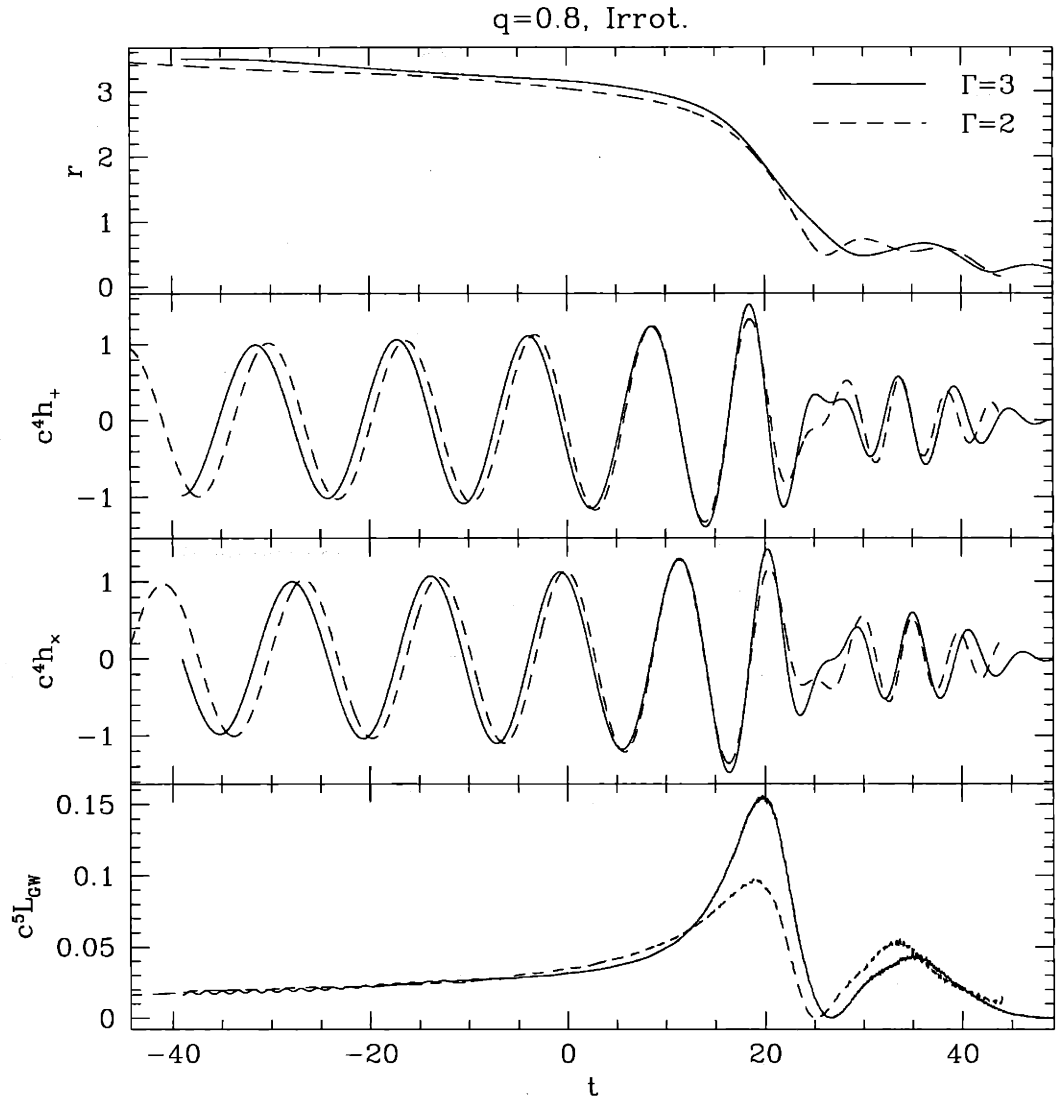

Figure 6-12: Binary separation (top panel), gravity wave forms (middle panels) and gravity wave luminosity (bottom panel) as a function of time for our irrotational calculations with mass ratio $q = 0.8$ started from $r_0 = 3.5$, shown in Fig. 6-11. The solid and dashed curves correspond to a $\Gamma = 3$ and $\Gamma = 2$ polytropic NS EOS, respectively. We see that gravity wave production is significantly suppressed for the softer, $\Gamma = 2$ EOS.

Chapter 7

Gravity wave power spectra

While it is important to compute templates for the gravity wave spectra that will be produced in coalescing NS binaries, it is at best an inexact art, which is made extremely difficult by uncertainties in the EOS of physical NS. Given that the detection of NS coalescence events may be easiest for narrow-band detectors, it is important to understand the frequency dependence of the gravity wave signal as well as the time behavior. In particular, the frequency dependence of the signal is not troubled by issues of phase-matching that will make template fitting almost impossible for the first detected signals. Instead, the power spectrum yields key information about the strongest features found in the signal, and since the characteristic frequency of the gravitational wave signal sweeps upward during the merger, does allow a glimpse into the time history of the evolution.

Zhuge, Centrella, and McMillan calculated the first power spectra for numerical calculations of binary mergers (1994; 1996), for a wide variety of system parameters. They found that the energy lost to gravity waves per unit frequency interval is given by

$$\frac{dE}{df} = \frac{c^3}{G}\frac{\pi}{2}(4\pi r^2) f^2 \left\langle |\tilde{h}_+(f)|^2 + |\tilde{h}_\times(f)|^2 \right\rangle \tag{7.1}$$

where the averages are taken over time as well as solid angle. In terms of the compo-

nents of the quadrupole tensor, the expression is given by

$$\frac{dE}{df} = \frac{\pi^2 G}{c^5}\left[\frac{8}{15}\left(|\tilde{Q}^{(2)}_{xx}-\tilde{Q}^{(2)}_{yy}|^2+|\tilde{Q}^{(2)}_{xx}-\tilde{Q}^{(2)}_{zz}|^2+|\tilde{Q}^{(2)}_{yy}-\tilde{Q}^{(2)}_{zz}|^2\right)+\frac{48}{15}\left(|\tilde{Q}^{(2)}_{xx}|^2+|\tilde{Q}^{(2)}_{yy}|^2+|\tilde{Q}^{(2)}_{zz}|^2\right)\right]. \quad (7.2)$$

In order to properly treat the complete time behavior of the wave form, we must include that part which represents the history of the binary system before the dynamical phase of the coalescence calculation starts. Thus, we attach a point-mass inspiral wave form, hereafter referred to as the inspiral subcomponent, onto the beginning of the signal calculated in our dynamical runs, hereafter referred to as the merger subcomponent, with the quadrupole tensor of the inspiral subcomponent assumed to have the form

$$Q_{xx}(t) = -Q_{yy}(t) = A(t)\sin(\phi(t)) \quad (7.3)$$

$$Q_{xy}(t) = A(t)\sin(\phi(t)) \quad (7.4)$$

$$Q_{zz}(t) = Q_{xz}(t) = Q_{yz}(t) = 0, \quad (7.5)$$

with amplitude and phase are given by

$$A(t) = (1+\epsilon)\frac{2M\mu}{[a_0(1-\frac{t}{t_0})^{0.25}]} \quad (7.6)$$

$$\phi(t) = -\int_t^0 \omega(t)dt \quad (7.7)$$

$$\omega(t) = (1.0+\epsilon')\sqrt{\frac{M}{[a_0(1-\frac{t}{t_0})^{0.25}]^3}}, \quad (7.8)$$

with a_0 the initial binary separation and M and μ the total and reduced masses of the system, respectively. The time constant t_0, is given in familiar fashion by

$$t_0 = \frac{5}{256}\frac{c^5}{G^3}\frac{a_0^4}{\mu M^2}. \quad (7.9)$$

The correction factor ϵ is used to account for finite size effects present in the numerical

calculation of the quadrupole moment, and is determined by matching the amplitude of the point-mass signal to the initial amplitude calculated during the dynamical phase of the merger. Typically, it is no larger than 3%. The correction factor ϵ' is used in a similar way to match the initial angular velocity of the system, and is of similar magnitude. For the point-mass approximation, the gravity wave spectrum is known to follow the power law form $dE/df \propto f^{\frac{1}{3}}$, up to the characteristic frequency at which the inspiral piece is truncated and our dynamical calculation attached. It is important to note that the power spectra components derived from the point-mass inspiral and our merger calculations are essentially independent of each other except in a the narrow frequency band characteristic of the crossover between the two. Thus, the power spectrum calculated for the merger calculation itself is unaffected by the details of the inspiral.

While it is true that the stiff EOS we use can support a long-lived quadrupole oscillation, we have found a modulated gravity wave signal at late times in all runs calculated in PN gravity. This differs significantly from previous purely Newtonian results (see, e.g., RS). As a result, we generally find that the gravity wave luminosity at late times is generally more than an order of magnitude lower than at peak. Including a fit to the late time behavior of the gravity wave forms, therefore, does not change the power spectrum in any significant way.

In Figs. 7-1 and 7-2, we show the power spectra computed for Newtonian run A1 and PN run E1. In both figures, the dashed and dotted curves represent the power spectra derived from the merger and point-mass inspiral subcomponents, respectively, with the heavy solid line representing the combined spectrum.

We see immediately that there is a significant difference in the power emitted between $700 - 2000$ Hz. This is directly attributable to the faster inspiral rates found in PN calculations. Since the binary system spends less time at a given characteristic frequency, the power emitted is greatly suppressed by the addition of 1PN effects. The difference in the "cliff frequency", where the power spectrum deviates from the point-mass limit is the best indicator of the start of dynamical instability. In general, the characteristic frequency of the merger sweeps upward monotonically throughout

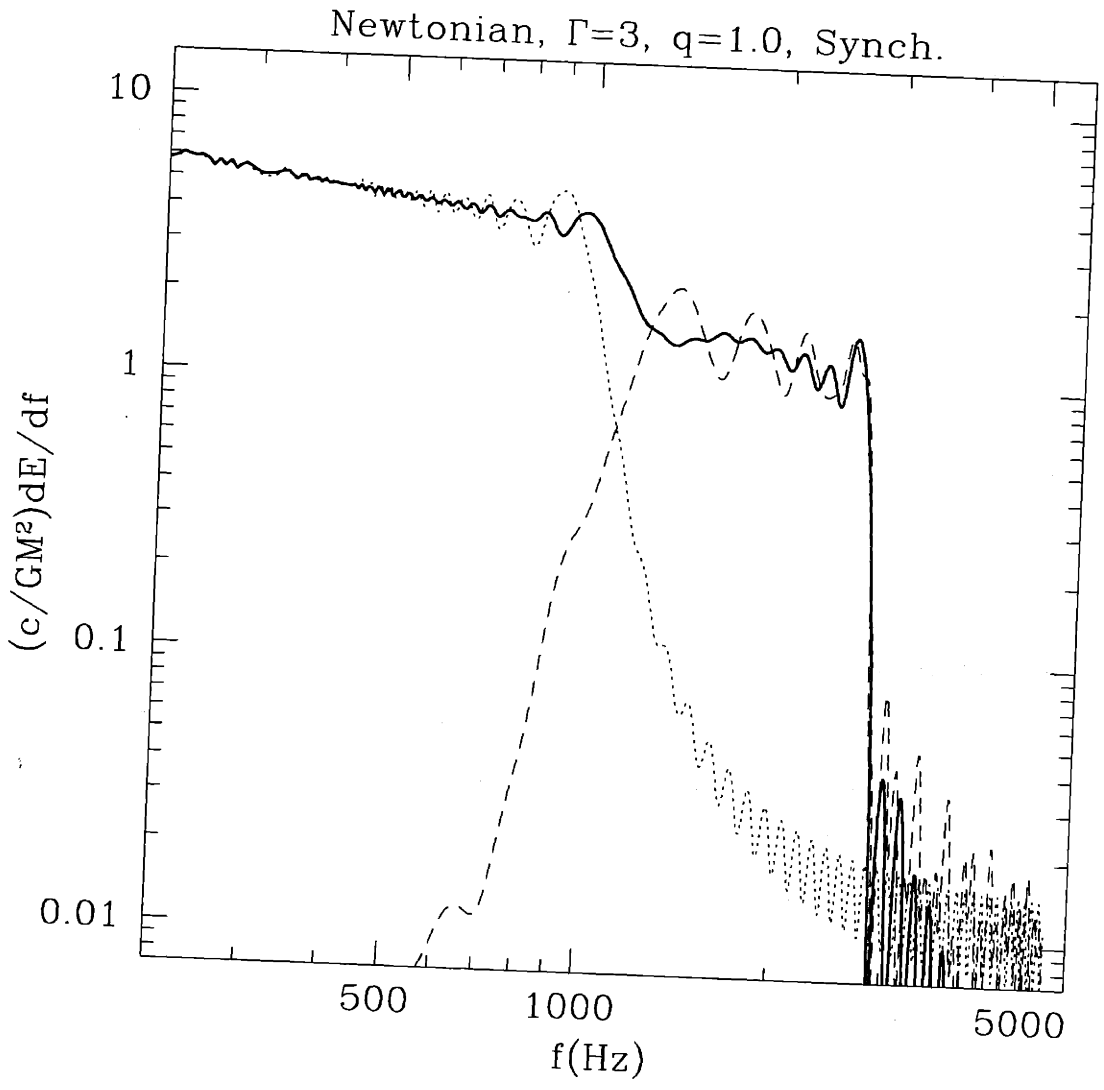

Figure 7-1: Gravity wave power spectrum calculated using Eq. 7.2 for Newtonian run A1. We show the point-mass inspiral (dotted) and merger (dashed) subcomponents of the run, along with the combined spectrum (heavy solid).

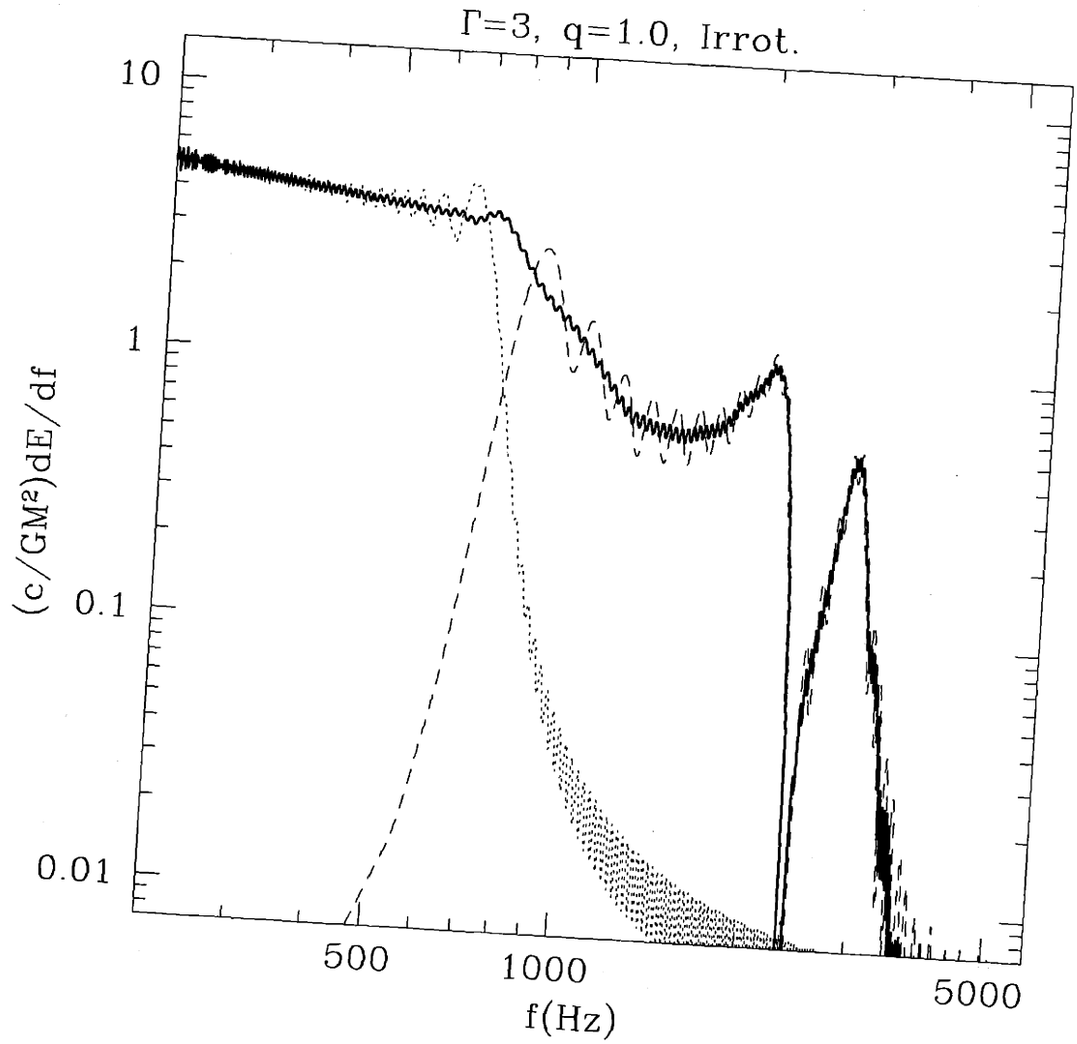

Figure 7-2: Gravity wave power spectrum calculated using Eq. 7.2 for the the $\Gamma = 3$ EOS, $q = 1.0$, irrotational run started from a separation $r_0 = 4.0\ R$. Conventions are as in Fig. 7-1. We see that the power emitted during the course of the merger is greatly suppressed relative to the Newtonian case, since the binary inspiral is much more rapid.

the coalescence process. The sharp peaks at $f \sim 2000$ Hz and $f \sim 3000$ Hz, therefore, result from emission at the gravity wave luminosity peak and during the remnant oscillation phase, respectively. Unlike some previous Newtonian results Zhuge, Centrella, & McMillan (1996), we find the amplitude of these peaks to be well below the point-mass prediction, by a factor of almost three and five, respectively. No calculation we have performed with our PN formalism has produced power above the point-mass prediction in any frequency range, indicating that the PN corrections not only enhance the dynamical instability of a binary system, but also cause a damping of the total gravity wave emission by shrinking the timescale during which the gravity wave luminosity is at its highest values.

In the top panel of Fig. 7-3, we show the power spectra computed for our $\Gamma = 3$ EOS, equal-mass calculations, which were started at initial separations of $r_0 = 3.5R$ and $r_0 = 4.0R$. We see there is general agreement above ~ 1 kHz, but a slight discrepancy at the characteristic frequency of the crossover between point-mass inspiral and our merger calculations. We find at separations of $r = 3.5 - 4.0R$, the binary does inspiral faster than the point-mass formula would predict. As the code has been extensively tested and shown to reproduce Newtonian results in this separation range, we attribute the effect to the PN gravitational formalism being used. Assuming quasi-equilibrium holds true in this regime, the inspiral rate should be given by

$$\frac{dr}{dt} = \left(\frac{dE}{dt}\right)_{grav} \left(\frac{dE}{dr}\right)^{-1}_{equil} \tag{7.10}$$

where $\left(\frac{dE}{dt}\right)_{grav}$ is the energy loss rate to gravitational radiation, and $\left(\frac{dE}{dr}\right)^{-1}_{equil}$ is the change in the total energy of a binary configuration with respect to separation for a quasi-equilibrium sequence of binary NS models. Since the former is nearly equal to the Newtonian value, we conclude that the slope of the equilibrium energy curve is made smaller by the addition of PN corrections to the gravitational potential energy and other terms in the total energy. While there must exist a minimum in the equilibrium energy curve at some separation, representing the innermost stable circular orbit (ISCO) of the sequence, it will be masked by the dynamical nature of

these calculations. The binary system undergoes a plunge phase not when the system reaches the ISCO, but rather when it is no longer to main quasi-equilibrium because the inspiral timescale grows comparable to the dynamical timescale of the NS.

Notable in the figure are the same sharp peaks at $f \sim 2000$ Hz and $f \sim 3000$ Hz, which represent emission at the gravity wave luminosity peak and during the remnant oscillation phase, respectively. Assuming that the remnant is stable against gravitational collapse and that a BH does not form, it should be possible to use narrow-band high-frequency detectors to study the NS EOS by tracing the sharp peaks found in the spectrum. If either oscillation frequency was measured, it could yield important information about the angular momentum present in the system and, in a secondary way, about the moments of inertia of the individual NS, the details of the remnant they form, and thus the EOS.

In the bottom panel of Fig. 7-3 we compare the power spectra of two of the runs used to study the dependence of the gravity wave signal on numerical resolution. We find that the spectra are similar, especially with regard to frequency regime of remnant oscillations, but disagree by a significant amount at lower frequencies. It is important to remember from Fig. 6-5 that the lowest resolution run suffered from larger initial oscillations around equilibrium. While these are at too high a frequency to play a significant role on the power spectrum, they do affect the binary infall. The extra energy present in the system, combined with the tendency of such systems to be slightly elliptical, leads to a much more rapid inspiral than was found for the higher resolution run, which showed very small oscillations initially. This is picked up well in the gravity wave spectrum, which shows suppressed power for the lowest resolution run at the characteristic frequencies of the last few orbits.

We expect that "cliff frequency" that must be located in the power spectrum at $\sim$ 700Hz, representing the onset of dynamical instability, may not actually yield detailed information about the NS EOS, especially given the noise that is expected to be present in any LIGO measurement. In the top panel of Fig. 7-4, we show the power spectra computed for both equal-mass runs started from $r_0 = 4.0R$. The power spectrum corresponding to the softer EOS does show excess power in the frequency

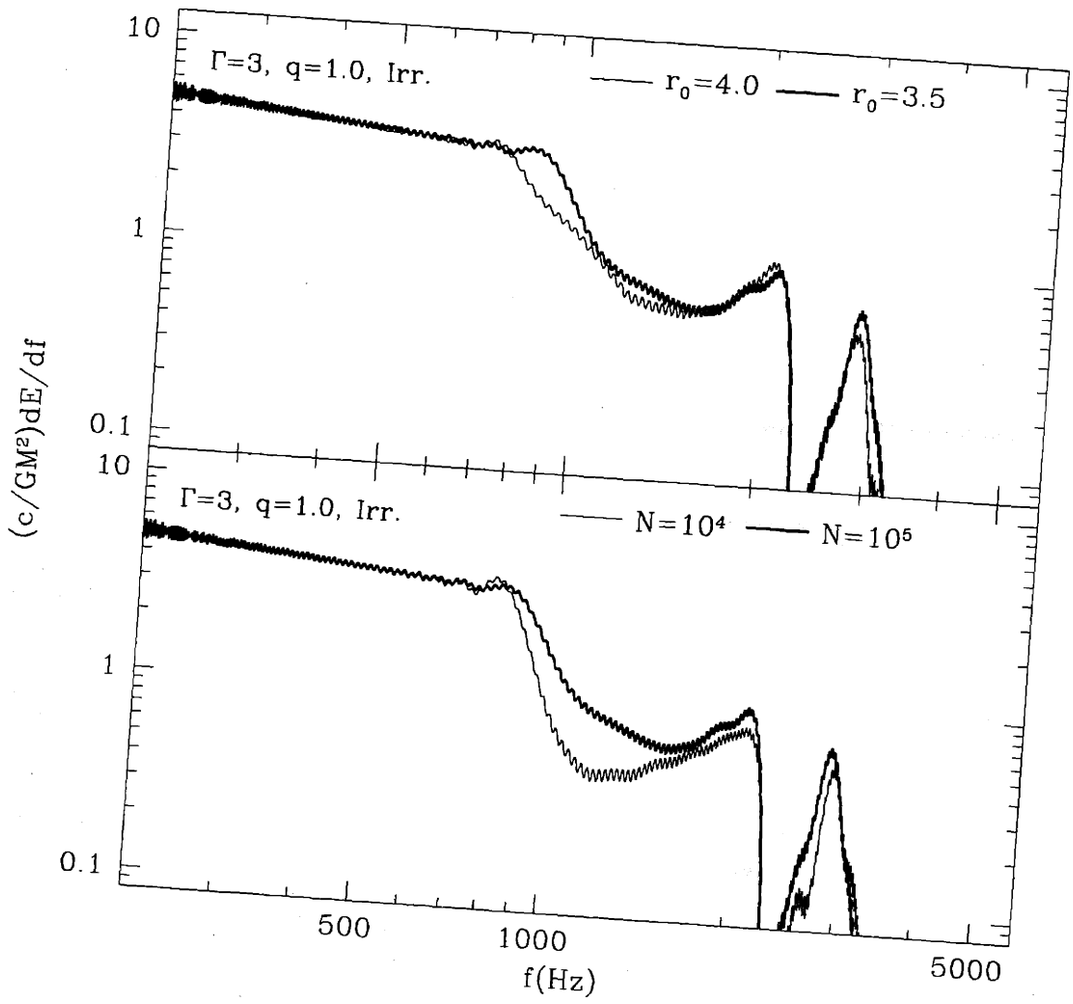

Figure 7-3: Gravity wave power spectra calculated using Eq. 7.2 for the the equal mass, $\Gamma = 3$ EOS, irrotational runs which differ in initial separation (top panel) and numerical resolution (bottom panel). In the top panel, we show the spectra of the calculations started from $r_0 = 4.0$ (thin solid) and $r_0 = 3.5$ (thick solid). In the bottom panel, we show the spectra for the runs with $N = 10^4$ (thin solid) and $N = 10^5$ (thick solid) SPH particles respectively.

range from $f \approx 1000 - 2000$ Hz, but at lower frequencies the spectra are nearly identical. The dynamical stability limit for the softer EOS is located inside that of the stiffer EOS, by $\Delta r \sim 0.2R$, but the resulting difference in power of $\sim 30\%$ in gravitational energy at a frequency of ~ 1500 Hz may be very difficult to detect. These conclusions, though, should tempered by the fact that our PN corrections are not taken at the full physical values. If indeed the difference between the dynamical stability limits of the stiffer and softer EOS are enhanced by PN corrections, it is likely the effect will be more pronounced in fully GR calculations. Since such an effect is imprinted on the gravity wave signal before the actual merger of the NS, we expect the results to be independent of the details of the remnant formation or collapse of the matter to a black hole. For the softer EOS, the peak in the power spectrum corresponding to maximum gravity wave emission is of lower amplitude and frequency when compared against the result of the stiffer EOS. The peak corresponding to remnant oscillations is greatly suppressed, since the soft EOS cannot support a stable triaxial configuration.

Although a synchronized initial condition is likely to be inappropriate for describing NS immediately before merger, it is relatively easier to construct than an irrotational one. In the bottom panel of Fig. 7-4, we compare the power spectra from a synchronized run against that of an irrotational run. We find that the sharper plunge seen in the synchronized run leads to lower power in the frequency range which describes inspiral. At frequencies greater than 1200 Hz, however, there is some measure of agreement, especially with regard to the amplitude of the peaks in the power spectrum. The frequencies of the first power spectrum peak are quite similar between the two calculations, indicating that the gravity wave power is much more strongly affected by the choice of EOS, rather than by the details of the initial spin configuration. Although it would be natural to assume that the initially synchronized run, which contains a greater total angular momentum in the system, would produce a remnant spinning at a higher frequency than an initially irrotational calculation, that is not the case. Instead, we find that the secondary peaks in the power spectra also line up well, since the synchronized run tends to transfer more of its angular mo-

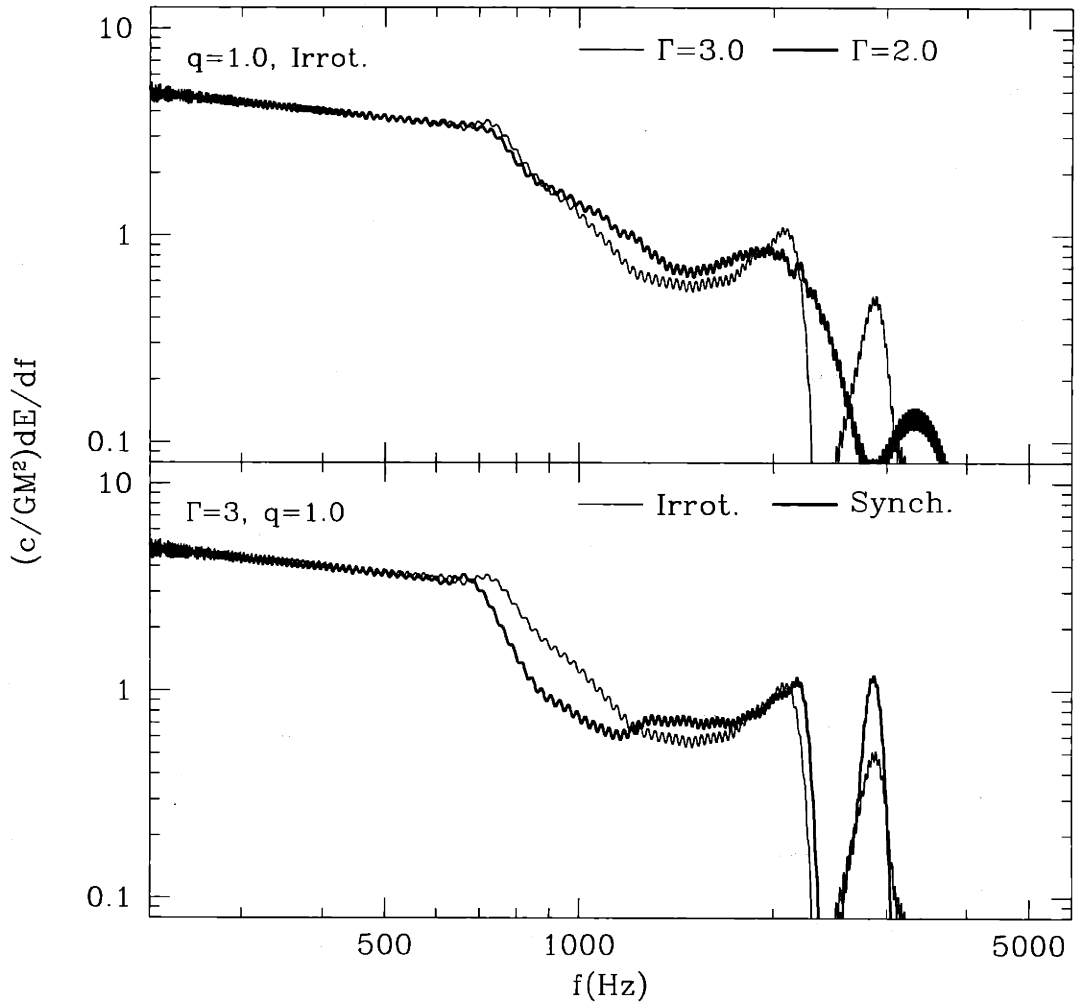

Figure 7-4: Gravity wave power spectra for runs which differ in the choice of EOS (top panel) and initial spin (bottom panel) for equal mass NS. In the top panel, we show the spectra for a $\Gamma = 3$ EOS (thin solid), along with that of a $\Gamma = 2$ EOS (thin solid). Both runs are initially irrotational. In the bottom panel we show the same $\Gamma = 3$ run, along with a synchronized run (thick solid).

mentum into particles shed through spiral arms, leaving the remnant with a similar amount of angular momentum regardless of the spin for these two cases.

In the top panel of Fig. 7-5, we compare irrotational runs with a $\Gamma = 3$ NS EOS and mass ratios of $q = 1.0$ and $q = 0.8$, both started from an initial separation of $r_0 = 3.5R$. We see a clear difference in the overall amplitude of the two power spectra, but in general the low-frequency behavior of the spectra is not qualitatively different. In both cases, we see a smooth decline in the gravity wave power which indicates the onset of dynamical instability, which levels off as we reach the characteristic frequency of the emission at peak luminosity. A key difference is the lack of a true peak in the signal for the $q = 0.8$ binary, which reflects the suppression of gravity wave production in unequal-mass collisions, discussed in Sec. 5.2. There is a well defined peak in the power spectra characteristic of emission from the remnant, nearly equal in intensity to the first peak, as was found for the equal-mass binary with the same EOS. The frequencies of both peaks in the $q = 0.8$ spectrum are shifted lower relative to their location in the equal-mass case, indicating that the frequency of such peaks might yield clues to the total mass of the binary system.

In the bottom panel of Fig. 7-5, we show a similar comparison, comparing runs with $\Gamma = 2$ and mass ratios of $q = 1.0$ and $q = 0.8$. The calculation for mass ratio $q = 0.8$ was started from an initial separation of $r_0 = 3.5$, whereas the calculation for mass ratio $q = 1.0$ was started from $r_0 = 4.0$, but for the sake of comparison we have excised the gravity wave forms for the times when the binary separation was in the range $r = 3.5 - 4.0$, and added on a point-mass inspiral in its stead. We see that as was the case for the stiffer NS EOS, the low frequency behavior of the power spectrum is qualitatively similar regardless of the mass ratio, but at frequencies above $f \approx 1800Hz$, the power emitted by the binary of mass ratio $q = 0.8$ drops off dramatically, as could have been predicted by the extreme reduction in the peak gravity wave luminosity seen in Fig. 6-12 for the run. Like the stiffer NS EOS, there is evidence for an oscillation peak in the spectrum at $f \sim 2700Hz$, a lower frequency than was seen for the equal-mass binary with the same choice of EOS.

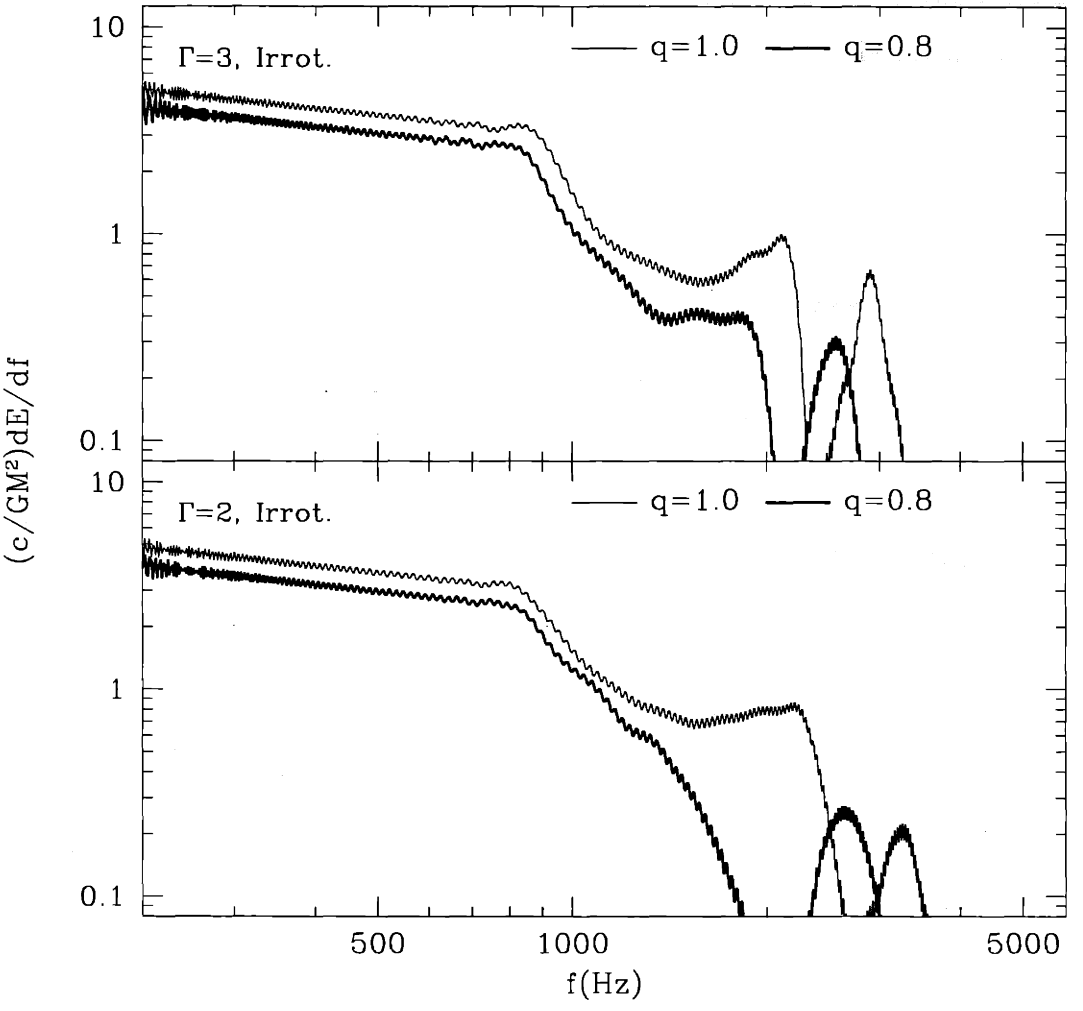

Figure 7-5: Gravity wave power spectra for runs with a $\Gamma = 3$ (top panel) and $\Gamma = 2$ (bottom panel) EOS. Thin solid curves represent the spectra for equal-mass runs, thick solid curves for runs with $q = 0.8$. In general, the binaries with $q = 0.8$ not only have lower amplitude through the lower frequency portion of the spectrum, but lack clear peaks at the characteristic frequency of peak gravity wave emission.

Chapter 8

Conclusions

Using the Lagrangian SPH code described in this thesis, which is complete to 1PN order and also includes all 2.5PN radiation reaction effects, we have investigated the properties of NS binary mergers in PN gravity. In addition to the method presented for constructing PN equilibrium initial conditions for synchronized binaries, we have used the results of the analytic work by Lombardi, Rasio, & Shapiro (1997) based on compressible ellipsoids to create realistic irrotational initial conditions.

Using a hybrid formalism in which radiation reaction is treated realistically but 1PN effects are scaled down in amplitude to remain numerically tractable, we have studied the effect of PN corrections on several aspects of binary NS mergers. We find that NS with a softer EOS, modeled here as $\Gamma = 2$ polytropes, produce higher gravity wave luminosities during the merger than NS with stiffer EOS, modeled as $\Gamma = 3$ polytropes. As was found in previous purely Newtonian calculations, the final merger remnant produced when $\Gamma = 2$ is an oblate spheroid, rather than a triaxial ellipsoid (obtained for $\Gamma = 3$). We find a strong second peak of gravity wave luminosity for a $\Gamma = 2$ EOS, whether or not we use 1PN gravity, as well as for calculations with a $\Gamma = 3$ EOS and PN gravity. This differs from the common finding for Newtonian binaries with stiff EOS.

By holding the EOS and the primary NS mass fixed while varying the secondary NS mass, we have studied the dependence of the gravity wave emission on the binary mass ratio. We find that the steep power-law scaling $h_{\max} \propto q^2$ for the maximum

amplitude, derived from purely Newtonian calculations in RS2 for a $\Gamma = 2$ EOS, remains approximately correct in PN gravity, for both $\Gamma = 2$ and $\Gamma = 3$ EOS. In both cases the dependence on q appears slightly steeper when 1PN effects are neglected (but while retaining 2.5PN effects). The maximum gravity wave luminosity for PN mergers follows a slightly steeper power law than the $L_{\rm max} \propto q^6$ found by RS2 for the $\Gamma = 2$ EOS, but is significantly flatter for the $\Gamma = 3$ EOS.

Our coalescence calculations using an irrotational initial condition, thought to be the physically realistic model, show clearly the development of a vortex sheet along the surface of contact. A turbulent region is seen until the time when the inner cores of the two NS begin to merge, at which point a stable, differentially rotating configuration is created. Although the peak gravity wave luminosity is generally similar for calculations with either choice of spin, irrotational mergers show suppressed secondary luminosity peaks, and only trace power afterwards.

We believe our results concerning irrotational binaries to be relatively unaffected by issues of numerical resolution, even though calculations performed at different resolutions do show subtle differences in the exact location and size of the vortices formed at the surface of contact. It is important to note that it is the outer regions of the star, at lower density, that supply material to the vortex sheet. The high density cores of the two NS inspiral during the entire process, and provide the dominant component of the quadrupole moment and thus the gravity wave signal. The path traced out by the NS cores depends sensitively on gravitational forces and properties of the fluid, such as the EOS, but proves to be remarkably insensitive to the details of the flow in the "turbulent" boundary region. The conclusion to be drawn is that numerical convergence for a given set of initial conditions and physical assumptions is possible without requiring excessive computational resources, even for this difficult problem involving small-scale instabilities.

We find that, in general, the addition of 1PN effects decreases the mass in the outer halo of the merger remnant for binaries with $q = 1$, especially when an irrotational initial condition is used. For this latter case, very little mass ($< 1\%$) is ejected through spiral arms during the merger. Since the 1PN corrections are artificially reduced in our

calculations, we expect that for two NS with realistic parameters and an irrotational initial configuration, no matter at all will be ejected. When a synchronized initial condition is used, we also find that the halo around the remnant is much denser and less extended for a softer NS EOS.

There is much information to be gained from examining the power spectrum of gravitational radiation emitted by a coalescing binary system. This may prove to be easier to study than the signal in the time-domain, since there are no issues of phase-matching to consider. The frequencies of the two peaks seen in the our spectra, which represent peak emission and the remnant oscillations, do give a strong clue to the nature of the NS EOS. While the frequency of peak oscillation is essentially the same in all our simulations, the width of the peak is seen to be strongly dependent on the EOS. The softer $\Gamma = 2$ EOS shows a broad peak of emission in the frequency range $f \sim 1500-2500$ Hz, whereas the stiffer $\Gamma = 3$ EOS calculations have a peak much more focused around $f = 1800-2200$ Hz, regardless of the initial spins. The stiffer EOS also results in a lower frequency oscillation than the softer one, with considerably greater power. Finally, for binary systems with unequal-mass components, the magnitude of the gravity wave emission is strongly correlated with the mass ratio q. Because the primary in such systems generally remains relatively undisturbed, whereas the secondary is tidally disrupted and accreted onto the primary, a large component of the matter essentially does not contribute to the gravity wave signal. Thus, even if NS masses do not typically lie within a narrow range, there should be a strong bias observationally toward detection of nearly equal-mass systems.

Bibliography

Abramovici, A. et al. 1992, Science, 256, 325

Abramovici, A. et al. 1996, Phys. Lett. A, 218, 157

Akmal, A., Pandharipande, V.R., & Ravenhall, D.G. 1998, Phys. Rev. C, 58, 1804

Arzoumanian, Z., Cordes, J.M., & Wasserman, I. 1999, Astrophys. J., 520, 696

Ayal, S. et al. 2001, Astrophys. J., 550, 846

Bailes, M. 1996, in IAU Symposium 165: Compact Stars in Binaries, ed. J. van Paradijs, E.P.J. van den Heuvel, & E. Kuulkers (Dordrecht: Kluwer), 213

Balsara, D. 1995, J. Comput. Phys., 121, 357

Barish, B. 1999, in Proceedings of the APS Division of Particle and Fields 1999, ed. K. Arisaka & Z. Bern, http://www.dpf99.library.ucla.edu, 14-12 (gr-qc/9905026)

Baumgarte, T.W., Hughes, S.A., & Shapiro, S.L. 1999, Phys. Rev. D, 60, 087501

Baumgarte, T.W., & Shapiro, S.L. 1998, Astrophys. J., 504, 431

Baumgarte, T.W., Shapiro, S.L., & Shibata, M. 2000, Astrophys. J. Lett., 528, L29

Baumgarte, T.W. et al. 1997, Phys. Rev. Lett., 79, 1182

Baumgarte, T.W. et al. 1998, Phys. Rev. D, 57, 7299

Baym, G. 1991, in Neutron Stars: Theory and Observation, ed. J. Ventura & D. Pines (Dordrecht: Kluwer), 21

Belczynski, K., & Kalogera, V. 2001, preprint (astro-ph/0012172)

Bertschinger, E. 2000, preprint (http:arcturus.mit.edu/8.962/notes/gr6.pdf)

Bethe, H.A, & Brown, G.E. 1998, Astrophys. J., 506, 780

Bhattacharya, D. & van den Heuvel, E. P. J. 1991, Phys. Rep., 203, 1

Bildsten, L., & Cutler, C. 1992, Astrophys. J., 400, 175

Blanchet, L., Damour, T., & Schäfer, G. 1990, Mon. Not. R. Astron. Soc., 242, 289 [BDS]

Blanchet, L. et al. 1996, Class. Quant. Grav., 13, 575

Bloom, J.S., Sigurdsson, S., & Pols, O.R. 1999, Mon. Not. R. Astron. Soc., 305, 763

Bonazzola, S., Gourgoulhon, E., & Marck, J.-A. 1999, Phys. Rev. Lett., 82, 892

Bradaschia, C. et al. 1990, Nucl. Instrum. Meth. A, 289, 518

Brown, G.E. 1995, Astrophys. J., 440, 270

Brown, G.E., & Bethe, H.A. 1994, Astrophys. J., 423, 659

Buonanno, A., & Damour, T. 1999, Phys. Rev. D, 59, 084006

Caron, B. et al. 1997, Class. Quant. Grav., 14, 1461

Chandrasekhar, S. 1987, Ellipsoidal Figures of Equilibrium; Revised Dover Edition (New Haven: Yale University Press)

Chernoff, D.F., & Finn, L.S. 1993, Astrophys. J. Lett., 411, L5

Chevalier, R.A. 1993, Astrophys. J. Lett., 411, L33

Chevalier, R.A. 1996, Astrophys. J., 459, 322

Cook, G.B., Shapiro, S.L., & Teukolsky, S.A. 1994, Astrophys. J., 424, 823

Cordes, J.M., & Chernoff, D.F. 1998, Astrophys. J., 505, 315

Curran, S.J., & Lorimer, D.R. 1995, Mon. Not. R. Astron. Soc., 276, 347

Danzmann, K. 1998, in Relativistic Astrophysics: Proceedings of the 162nd W.E. Heraeus Seminar, ed. H. Riffert et al. (Wiesbaden: Vieweg Verlag), 48

Danzmann, K. 2000, Adv. Space Res., 25, 1129

Dave, R., Dubinsky, J., & Hernquist, L. 1997, New Astron., 2, 277

Davies, M.B. et al. 1994, Astrophys. J., 431, 742

Deich, W.T.S., & Kulkarni, S.R. 1996, in IAU Symposium 165: Compact Stars in Binaries, ed. J. van Paradijs, E.P.J. van den Heuvel, & E. Kuulkers (Dordrecht: Kluwer), 279

Del Noce, C., Preti, G., & de Felice, F. 1998, Astrophys. J., 507, 287

Eichler, D. et al. 1989, Nature, 340, 126

Faber, J.A., & Rasio, F.A. 2000, Phys. Rev. D, 62, 064012

Faber, J.A., Rasio, F.A., & Manor, J.B. 2001, Phys. Rev. D, 63, 044012

Finn, L.S., & Chernoff, D.F. 1993, Phys. Rev. D, 47, 2198

Flanagan, E.E., & Hughes, S.A. 1998, Phys. Rev. D, 57, 4566

Freiburghaus, C., Rosswog, S., & Thielemann, F.-K. 1999, Astrophys. J. Lett., 525, L121

Freise, A. et al. 2000, Phys. Lett. A, 277, 135

Frigo, M., & Johnson, S. 1997, MIT Laboratory of Computer Science preprint (MIT-LCS-TR-728)

Fryer, C.L., Burrows, A., & Benz, W. 1998, Astrophys. J., 496, 333

Fryer, C.L., & Kalogera, V. 1999, preprint (astro-ph/9911312)

Fryer, C.L., Woosley, S.E., & Hartmann, D.H. 1999, Astrophys. J., 526, 152

Gingold, R.A., & Monaghan, J.J. 1977, Astrophys. J., 181, 375

Glendenning, N.K. 1992, Phys. Rev. D, 46, 1274

Gourgoulhon, E. et al. 2001, Phys. Rev. D, 63, 064029

Grishchuk, L.P. et al. 2001, Phys. Usp., 44, 1

Hernquist, L., & Katz, N. 1989, Astrophys. J. Suppl., 70, 419

Houck, J.C., & Chevalier, R.A. 1992, Astrophys. J., 376, 234

Hough, J. 1992, in Proceedings of the Sixth Marcel Grossmann Meeting, ed. H. Sato & T. Nakamura (Singapore: World Scientific), 192

Janka, H.-Th. et al. 1999, Astrophys. J. Lett., 527, L39

Junker, W., & Schäfer, G. 1992, Mon. Not. R. Astron. Soc., 254, 146

Kalogera, V. 2000, in AIP Conf. Proc. 523, Gravitational Waves: Third Edoardo Amaldi Conference, ed. S. Meshkov (New York: AIP Press), 41

Kalogera, V., & Lorimer, D.R. 2000, Astrophys. J., 530, 890

Kalogera, V. et al. 2000, preprint (astro-ph/0012038)

Kidder, L.E., Will, C.M., & Wiseman, A.G. 1992, Class. Quant. Grav., 9, L125

Kochanek, C.S. 1992, Astrophys. J., 398, 234

Kouveliotou, C. et al. 1993, Astrophys. J. Lett., 413, L101

Kuroda, K. et al. 1997, in Proceedings of the International Conference on Gravitational Waves: Sources and Detectors, ed. I. Ciufolini & F. Fidecard (Singapore: World Scientific), 100

Lai, D., Chernoff, D.F., & Cordes, J.M. 2001, Astrophys. J., 549, 1111

Lai, D., Rasio, F.A., & Shapiro, S.L. 1993a, Astrophys. J. Lett., 406, L63 [LRS1]

Lai, D., Rasio, F.A., & Shapiro, S.L. 1993b, Astrophys. J. Suppl., 88, 205 [LRS2]

Lai, D., Rasio, F.A., & Shapiro, S.L. 1994a, Astrophys. J., 420, 811 [LRS3]

Lai, D., Rasio, F.A., & Shapiro, S.L. 1994b, Astrophys. J., 423, 344 [LRS4]

Lai, D., Rasio, F.A., & Shapiro, S.L. 1994c, Astrophys. J., 437, 742 [LRS5]

Lai, D., & Shapiro, S.L. 1995, Astrophys. J., 442, 259

Lai, D., & Wiseman, A.G. 1997, Phys. Rev. D, 54, 3958

Landry, W., & Teukolsky, S.A. 1999, preprint (gr-qc/9912004)

Lattimer, J.M., & Swesty, F.D. 1991, Nucl. Phys., A535, 331

Lee, W.H., & Kluzniak, W.L. 1999a, Astrophys. J., 526, 178

Lee, W.H., & Kluzniak, W.L. 1999b, Mon. Not. R. Astron. Soc., 308, 780

Lincoln, W., & Will, C.M. 1990, Phys. Rev. D, 42, 1123

Lipunov, V.M., Postnov, K.A., & Prokhorov, M.E. 1997a, Mon. Not. R. Astron. Soc., 288, 245

Lipunov, V.M., Postnov, K.A., & Prokhorov, M.E. 1997b, Astrophys. Lett., 23, 492

Lipunov, V.M. et al. 1995, Astrophys. J., 454, 593

Livio, M., & Waxman, E. 2000, Astrophys. J., 538, 187

Lombardi, J.C., Rasio, F.A., & Shapiro, S.L. 1997, Phys. Rev. D, 56, 3416

Lombardi, J.C. et al. 1999, J. Comput. Phys., 152, 687

Lucy, L.B. 1977, Astron. J., 82, 1013

MacFayden, A.I., & Woosley, S.E., 1999, 524, 262

Marković, D. 1993, Phys. Rev. D, 48, 4738

Marronetti, P., Mathews, G.J., & Wilson, J.R. 1998, Phys. Rev. D, 58, 107503

Marronetti, P., Mathews, G.J., & Wilson, J.R. 1999, Phys. Rev. D, 60, 087301

Meers, B.J. 1988, Phys. Rev. D, 38, 2317

Mészáros, P. 2000, Nucl. Phys. B Suppl., 80, 63

Mészáros, P., & Rees, M.J. 1992, Astrophys. J., 397, 570

Mészáros, P. Rees, M.J., & Wijers, R.A.M.J. 1999, New Astron., 4, 303

Miller, M., Suen, W., & Tobias, M. 1999, preprint (gr-qc/9910022)

Misner, C.W., Thorne, K.W., & Wheeler, J.A. 1973, Gravitation (New York: W.H. Freeman)

Monaghan, J.J. 1992, Ann. Rev. Astron. Astrophys., 30, 543

Monaghan, J.J., & Lattanzio, J.C. 1985, Astron. Astrophys., 149, L35

Nakamura, T. 1994, in Relativistic Cosmology: Proceedings of the Eighth Nishinomiya-Yukawa Memorial Symposium, ed. M. Sasaki (Tokyo: Universal Academy Press), 155

Nakamura, T., & Oohara, K. 1989, Prog. Theor. Phys., 82, 1066

Nakamura, T., & Oohara, K. 1991, Prog. Theor. Phys., 86, 73

Nakamura, T., & Oohara, K. 1999, in Proceedings of the International Conference on Numerical Astrophysics 1998, ed. S.M. Miyama, K. Tomisaka, & T. Hanawa (Boston: Kluwer Academic), 247

Narayan, R., Paczyński, B., & Piran, T. 1992, Astrophys. J. Lett., 395, L83

Narayan, R., Piran, T., & Shemi, A. 1991, Astrophys. J. Lett., 379, L17

New, K.C.B., & Tohline, J.E. 1997, Astrophys. J., 490, 311

Oohara, K., & Nakamura, T. 1989, Prog. Theor. Phys., 82, 535

Oohara, K., & Nakamura, T. 1990, Prog. Theor. Phys., 83, 906

Oohara, K., & Nakamura, T. 1992, Prog. Theor. Phys., 88, 307

Phinney, E.S. 1991, Astrophys. J. Lett., 380, L17

Portegies Zwart, S.F., & Yungelson, L.R. 1998, Astron. Astrophys., 332, 173

Rasio, F.A. 2000, in Prog. Theor. Phys. Suppl. 138: Proceedings of the 5th International Conference on Computational Physics, ed. Y. Hiwatari et al. (Kyoto: Yukawa Istitute), 609

Rasio, F.A. 2001, in Black Holes in Binaries and Galactic Nuclei: Proceedings of the ESO Workshop, ed. L. Kaper, E.P.J. van den Heuvel, and P.A. Woudt (Berlin: Springer), 344

Rasio, F.A., & Shapiro, S.L. 1992, Astrophys. J., 377, 559

Rasio, F.A., & Shapiro, S.L. 1992, Astrophys. J., 401, 226 [RS1]

Rasio, F.A., & Shapiro, S.L. 1994, Astrophys. J., 432, 242 [RS2]

Rasio, F.A., & Shapiro, S.L. 1995, Astrophys. J., 438, 887 [RS3]

Rasio, F.A., & Shapiro, S.L. 1996, in IAU Symposium 165: Compact Stars in Binaries, ed. J. van Paradijs, E.P.J. van den Heuvel, & E. Kuulkers (Dordrecht: Kluwer), 17

Rasio, F.A., & Shapiro, S.L. 1999, Class. Quant. Grav., 16, 1

Rosswog, S., Freiburghaus, C., & Thielemann, F.-K. 2000, preprint (astro-ph/0012046)

Rosswog, S. et al. 1999, Astron. Astrophys., 341, 499

Rosswog, S. et al. 2000, Astron. Astrophys., 360, 171

Ruffert, M., & Janka, H.-Th. 1998, Astron. Astrophys., 338, 535

Ruffert, M., Janka, H.-Th., & Schäfer, G. 1996, Astron. Astrophys., 311, 532

Ruffert, M., Rampp, M., & Janka, H.-Th. 1997, AStron. Astrophys., 321, 911

Ruffert, M. et al. 1997, Astron. Astrophys., 319, 122

Schutz, B.F. 1986, Nature, 323, 310

Seidel, E. 1998, in Relativistic Astrophysics: Proceedings of the 162nd W.E. Heraeus Seminar, ed. H. Riffert et al. (Wiesbaden: Vieweg Verlag), 229

Shapiro, S.L. 1998, Phys. Rev. D, 58, 103002

Shapiro, S.L., & Teukolsky, S.A. 1983, Black Holes, White Dwarfs, and Neutron Stars (New York: Wiley)

Shibata, M. 1999, Phys. Rev. D, 60, 104052

Shibata, M., Oohara, K., & Nakamura, T. 1992, Prog. Theor. Phys., 88, 1079

Shibata, M., Oohara, K., & Nakamura, T. 1993, Prog. Theor. Phys., 89, 809

Shibata, M., Oohara, K., & Nakamura, T. 1997, Prog. Theor. Phys., 98, 1081

Shibata, M., & Taniguchi, K. 1997, Phys. Rev. D, 56, 811

Shibata, M., & Uryu, K. 2000, Phys. Rev. D, 61, 064001

Shibata, M., & Uryu, K. 2001, preprint (astro-ph/0104409)

Sneden, C. et al. 2000a, Astrophys. J. Lett., 533, L139

Sneden, C. et al. 2000b, Astrophys. J. Lett., 536, L85

Stairs, I.H. 1998, Astrophys. J., 505, 352

Strain, K.A., & Meers, B.J. 1991, Phys. Rev. Lett., 66, 1391

Swesty, F.D., Wang, E.Y.M., & Calder, A.C. 2000, Astrophys. J., 541, 937

Tagoshi, H. et al. 2001, Phys. Rev. D, 63, 062001

Taniguchi, K. 1999, Prog. Theor. Phys. 101, 283

Taniguchi, K., & Nakamura, T. 2000a, Phys. Rev. D, 62, 044040

Taniguchi, K., & Nakamura, T. 2000b, Phys. Rev. Lett., 84, 581

Taniguchi, K., & Shibata, M. 1997, Phys. Rev. D, 56, 798

Taylor, J.H., & Weisberg, J.M. 1989, Astrophys. J., 345, 434

Teukolsky, S.A. 1998, Astrophys. J., 504, 442

Thielemann, F.-K. et al. 2001, preprint (astro-ph/0101476)

Thorne, K.S. 1987, in 200 Years of Gravitation, ed. S. Hawking & W. Israel (Cambridge, Cambridge University Press), 330

Thorsett, S.E., & Chakrabarty, D. 1999, Astrophys. J. 512, 288

Timmes, F.X., Woosley, S.E., & Weaver, T.A. 1996, Astrophys. J., 457, 834

Uryu, K., & Eriguchi, Y. 2000, Phys. Rev. D, 61, 124023

Uryu, K., Shibata, M., & Eriguchi, Y. 2000, Phys. Rev. D, 62, 104015

van den Heuvel, E.P.J., & Lorimer, D.R. 1996, Mon. Not. R. Astron. Soc., 283, L37

Wang, E.Y.M., Swesty, F.D., & Calder, A.C. 1998, in Proceedings of the Second Oak Ridge Symposium on Atomic and Nuclear Astrophysics ed. A. Mezzacappa (London: Institute of Physics Publishing), 723

Wang, J.C.L. et al. 1999, Astron. Astrophys., 345, 869

Weber, J. 1961, General Relativity and Gravitational Waves (New York: Wiley)

Will, C.M. 1994, in Relativistic Cosmology: Proceedings of the Eighth Nishinomiya-Yukawa Memorial Symposium, ed. M. Sasaki (Tokyo: Universal Academy Press), 83

Wiringa, R.B., Fiks, V., & Fabrocini, A. 1988, Phys. Rev. C, 38, 1010

Wolczan, A. 1991, Nature, 350, 688

Zahn, J.-P. 1992, in Binaries as Tracers of Stellar Formation, ed. A. Duquennoy & M. Mayor (Cambridge: Cambridge University Press), 253

Zhuge, X., Centrella, J., & McMillan, S. 1994, Phys. Rev. D, 50, 6247

Zhuge, X., Centrella, J., & McMillan, S. 1996, Phys. Rev. D, 54, 7261